

10710
①

AD-A151 929



DTIC FILE COPY

RADIATION AND SCATTERING
 OF SPIRAL ANTENNAS
 THESIS
 John Paul Skinner
 Second Lieutenant, USAF
 AFIT/GE/ENG/84D-60

This document has been approved
 for public release and sale; its
 distribution is unlimited.

DTIC
SELECTED
APR 02 1985
S D
E

DEPARTMENT OF THE AIR FORCE
 AIR UNIVERSITY

AIR FORCE INSTITUTE OF TECHNOLOGY

Wright-Patterson Air Force Base, Ohio

85 03 13 054

**Best
Available
Copy**



RADIATION AND SCATTERING
OF SPIRAL ANTENNAS

THESIS

John Paul Skinner
Second Lieutenant, USAF

AFIT/GE/ENG/84D-60



Approved for public release; distribution unlimited

RADIATION AND SCATTERING OF SPIRAL ANTENNAS

THESIS

Presented to the Faculty of the School of Engineering
of the Air Force Institute of Technology

Air University

In Partial Fulfillment of the
Requirements for the Degree of

Master of Science in Electrical Engineering

John Paul Skinner, B.S.
Second Lieutenant, USAF

December 1984

| | |
|--------------------|-------------------------------------|
| Accession For | |
| NTIS GRA&I | <input checked="" type="checkbox"/> |
| DTIC TAB | <input type="checkbox"/> |
| Unannounced | <input type="checkbox"/> |
| Justification | <input type="checkbox"/> |
| By _____ | |
| Distribution/ | |
| Availability Codes | |
| and/or | |
| Dist. Statement | |
| A-1 | |

Approved for public release; distribution unlimited



Preface

The purpose of this study is to use a general technique to analyze the radiation and scattering performance of a logarithmic spiral antenna. This type of antenna is typically used in radar warning receivers because it has more than one mode of radiation, which gives the antenna a direction finding capability.

The study uses a relatively new general program known as the Electromagnetic Surface Patch (ESP) code to analyze the antenna. Three antenna modelling techniques are explored and results are compared to show how to obtain the most accurate modelling.

The first chapter gives a general background of antenna scattering and some of the basic knowledge of spiral antennas. The second chapter gives a development of the method of moments, which is a mathematical process used in the ESP code. This chapter is intended to give only the basics necessary to understand the moment method. The third chapter introduces the three computer modelling schemes. The computer results for the models are given in the fourth chapter. This chapter also compares the results to draw some specific conclusions. The fifth chapter gives the general conclusions for the study and discusses possibilities to extend the study. Finally, the three appendices are given to support the computer modelling discussion in the third chapter.

I would like to sincerely thank the Aircraft Observables and Analysis Branch, Directorate of Avionics Engineering, Deputy for Engineering, Aeronautical Systems Division (ASD/ENAMA) at Wright-Patterson AFB OH for the computer support necessary to carry out this project. I also have sincere gratitude for the assistance of Dr. E. H. Newman at the Ohio State University Electrosience Lab with the use of the ESP code.

John Paul Skinner

Table of Contents

| | Page |
|--|------|
| Preface | ii |
| List of Figures | v |
| List of Tables | viii |
| Abstract | ix |
| I. Introduction | 1 |
| Background | 1 |
| Problem | 1 |
| General Approach | 2 |
| Theory | 2 |
| Literature Review | 10 |
| II. The Method of Moments | 15 |
| Introduction | 15 |
| Expansion Functions | 15 |
| The Piecewise Sinusoidal Expansion Function | 18 |
| Testing Functions | 20 |
| Point Matching | 22 |
| Galerkin's Method | 24 |
| Reaction Integral Equation | 25 |
| Radiation Problems | 28 |
| III. Computer Modelling | 31 |
| Thin Wire Modelling | 31 |
| Wire Grid Modelling | 35 |
| Patch Modelling | 38 |
| IV. Results | 42 |
| V. Conclusions and Recommendations | 76 |
| Appendix A: Thin Wire Model Input | 78 |
| Appendix B: Wire Grid Model Input | 82 |
| Appendix C: Plate Model Programming | 87 |
| Bibliography | 92 |
| Vita | 94 |

List of Figures

| Figure | Page |
|---|------|
| 1. Equivalent Circuits for Transmitting Antennas | 3 |
| 2. Short-Circuited Scattering Antenna | 4 |
| 3. Loaded Scattering Antenna Model | 5 |
| 4. One Arm Archimedian Spiral | 10 |
| 5. Example of Current Distribution | 17 |
| 6. Three Pulse Approximation to Current | 17 |
| 7. Piecewise Sinusoidal Functions | 19 |
| 8. Overlapping Piecewise Sinusoidal Functions | 19 |
| 9. Delta Gap Model | 29 |
| 10. Two Arm Thin Wire Model | 32 |
| 11. Thin Wire Modelling | 33 |
| 12. Feed System | 34 |
| 13. Wire Grid Modelling | 36 |
| 14. Wire Grid Feed Connection | 37 |
| 15. Surface Patch Geometry | 39 |
| 16. Sum Pattern at 2 GHz, Phi Pol., Thin Wire Model | 44 |
| 17. Sum Pattern at 2 GHz, Theta Pol., Thin Wire Model | 45 |
| 18. Diff. Pattern at 2 GHz, Phi Pol., Thin Wire Model, Phi = 0 | 46 |
| 19. Diff. Pattern at 2 GHz, Theta Pol., Thin Wire Model, Phi = 0 | 46 |
| 20. Diff. Pattern at 2 GHz, Phi Pol., Thin Wire Model, Phi = 45 | 48 |
| 21. Diff. Pattern at 2 GHz, Theta Pol., Thin Wire Model, Phi = 45 | 49 |

| | Page |
|--|------|
| 22. Diff. Pattern at 2 GHz, Phi Pol., Thin Wire Model, Phi = 90 | 49 |
| 23. Diff. Pattern at 2 GHz, Theta Pol., Thin Wire Model, Phi = 90 | 50 |
| 24. Sum Pattern at 2 GHz, Phi Pol., Wire Grid | 51 |
| 25. Sum Pattern at 2 GHz, Theta Pol., Wire Grid | 51 |
| 26. Diff. Pattern at 2 GHz, Phi Pol., Wire Grid, Phi = 0 | 52 |
| 27. Diff. Pattern at 2 GHz, Theta Pol., Wire Grid, Phi = 0 | 52 |
| 28. Sum Pattern at 1 GHz, Phi Pol., Wire Grid | 53 |
| 29. Sum Pattern at 1 GHz, Theta Pol., Wire Grid | 54 |
| 30. Diff. Pattern at 1 GHz, Phi Pol., Wire Grid | 54 |
| 31. Diff. Pattern at 1 GHz, Theta Pol., Wire Grid | 55 |
| 32. Sum Pattern at 3.75 GHz, Phi Pol., Wire Grid | 55 |
| 33. Sum Pattern at 3.75 GHz, Theta Pol., Wire Grid | 56 |
| 34. Diff. Pattern at 3.75 GHz, Phi Pol., Wire Grid | 56 |
| 35. Diff. Pattern at 3.75 GHz, Theta Pol., Wire Grid | 57 |
| 36. Relative Amp. of Current at 500 MHz, Sum Pattern | 59 |
| 37. Relative Amp. of Current at 1 GHz, Sum Pattern | 60 |
| 38. Relative Amp. of Current at 2 GHz, Sum Pattern | 60 |
| 39. Relative Amp. of Current at 3.75 GHz, Sum Pattern | 61 |
| 40. Relative Amp. of Current at 5 GHz, Sum Pattern | 61 |

| | Page |
|---|------|
| 41. Relative Amp. of Current at 500 MHz, Diff. Pattern | 62 |
| 42. Relative Amp. of Current at 1 GHz, Diff. Pattern | 63 |
| 43. Relative Amp. of Current at 2 GHz, Diff. Pattern | 63 |
| 44. Relative Amp. of Current at 3.75 GHz, Diff. Pattern | 64 |
| 45. Relative Amp. of Current at 5 GHz, Diff. Pattern | 64 |
| 46. Phase of Current at 500 MHz, Sum Patt. | 66 |
| 47. Phase of Current at 1 GHz, Sum Patt. | 66 |
| 48. Phase of Current at 2 GHz, Sum Patt. | 67 |
| 49. Phase of Current at 3.75 GHz, Sum Patt. | 67 |
| 50. Phase of Current at 5 GHz, Sum Patt. | 68 |
| 51. Phase of Current at 1 GHz, Diff. Patt. | 68 |
| 52. Phase of Current at 2 GHz, Diff. Patt. | 69 |
| 53. Phase of Current at 3.75 GHz, Diff. Patt. | 69 |
| 54. Phase of Current at 5 GHz, Diff. Patt. | 70 |
| 55. Relative Amp. of Current at 2 GHz, Loaded Model, Sum Patt. | 72 |
| 56. Relative Amp. of Current at 2 GHz, Loaded Model, Diff. Patt. | 72 |
| 57. Sum Pattern at 2 GHz, Phi Pol., Loaded Model . . | 73 |
| 58. Sum Pattern at 2 GHz, Theta Pol., Loaded Model | 74 |
| 59. Diff. Patt. at 2 GHz, Phi Pol., Loaded Model . . | 74 |
| 60. Diff. Patt. at 2 GHz, Theta Pol., Loaded Model | 75 |

List of Tables

| Table | | Page |
|-------|--|------|
| I. | Feed Voltages | 35 |
| II. | Patch Model Computation Time | 41 |
| III. | Gain of Components in Two Arm Model | 42 |
| IV. | Gain of Circular Polarization (Two Arm Model) | 43 |
| V. | Mode Circumference Conversion | 58 |

Abstract

This study uses the method of moments with the Electromagnetic Surface Patch Code to analyze the radiation patterns and currents developed on a planar logarithmic spiral antenna. The study also outlines a method to analyze the radar cross section of the antenna. Three computer modelling concepts are explored. The first and most simple is the thin wire model, which is a set of straight thin wire segments which approximates the shape of the antenna. The second concept explored is that of wire grid modelling. The purpose of this model is to check the transverse components of current along the strips of the spiral's arms. The last model is a patch model, which is introduced to best model the structural scattering component of radar cross section. Unfortunately, this model proved to be infeasible unless a very fast computer system is used. Results are given for the sum and difference modes of radiation. These results show that the thin wire model is adequate for radiation analysis, but the tips of the arms must be modelled with an impedance to absorb the outward travelling energy in the current. Without this loading, the arms will develop a standing wave pattern for the current distribution, which is inconsistent with experimentation.

CHAPTER 1

Introduction

Background

One of the major contributors to the radar cross section of an air vehicle is antenna scattering. It is an inherent and desired property of an antenna to receive and/or radiate electromagnetic energy efficiently. Unfortunately, an antenna may radiate when excited by incident radiation, as well as when excited at the feed. It is this reradiation of energy which is known as antenna scattering and produces the radar cross section of the antenna. Several antennas are exposed to incident radiation on any conventional military airplane. At least one of these belongs to the radar warning receiver, which is designed to intercept and identify incident electromagnetic energy. It is not a trivial task to camouflage this antenna, while retaining its primary mission capabilities.

Conventional radar warning receivers use cavity backed flat spiral antennas. These antennas are broadband and polarization independent (for any linear polarization). However, these antennas may have an unacceptable radar cross section.

Problem

The scattering mechanisms of a radar warning receiver antenna must be investigated and understood to reduce the

radar cross section of the antenna. Also, a general method of analysis needs to be used to determine the radiation characteristics of the antenna.

General Approach

The scattering characteristics of a spiral antenna can be derived from the currents induced on the antenna by incident electromagnetic energy. In this study, the reaction integral equation is used to describe the interaction of the incident and scattered fields with the current distribution induced on the antenna. The reaction integral equation can also be used to describe the interaction of the current distribution with fields coming from other currents that together radiate. A solution to the reaction integral equation is obtained via the method of moments.

Theory

The scattering characteristics of an object are normally described by the radar cross section (RCS) of the object. The RCS is a parameter which is directly proportional to the power returned to a radar which illuminates the object. The RCS is defined mathematically as [1:335]

$$\sigma = \lim_{r \rightarrow \infty} 4 \pi r^2 \frac{|\bar{E}_s|^2}{|\bar{E}_i|^2} \quad (1-1)$$

where r = distance from the observation point to object

$|\vec{E}_s|$ = amplitude of scattered electric field at observation point

$|\vec{E}_i|$ = amplitude of incident electric field on object.

Although the RCS has units of length squared, it is not necessarily related to the physical size of the object.

R. B. Green presented the fundamental concepts of antenna scattering. He started by giving the simple circuit models for a transmitting antenna shown in Figure 1.

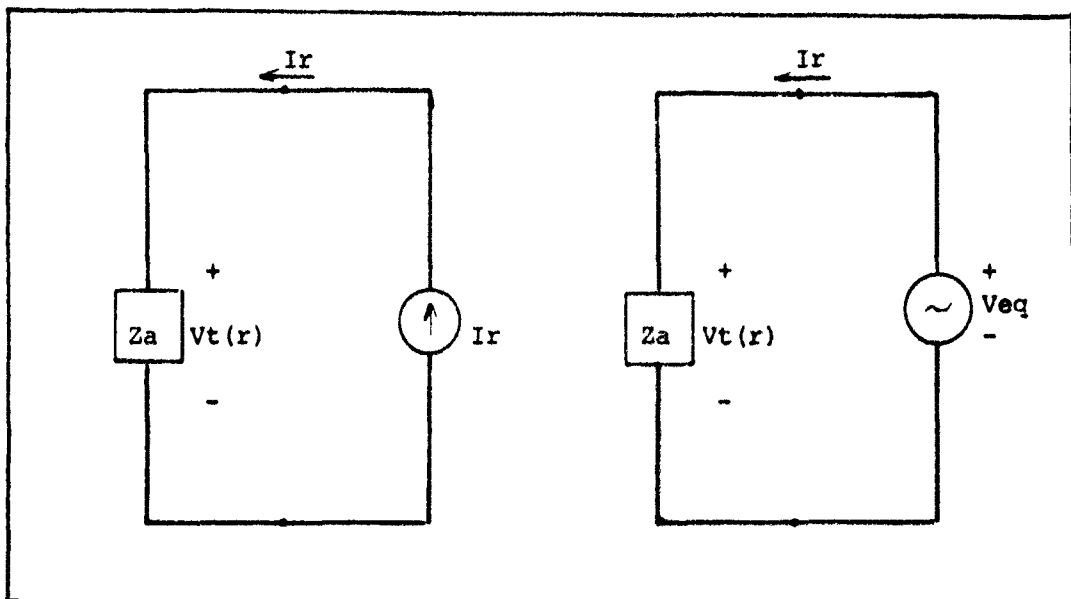


Figure 1. Equivalent Circuits for Transmitting Antennas
Source: [2]

The driving sources are the current and voltage sources. The nodes represent the terminals of the antenna. The terminal (input) current to the antenna is denoted I_r in each case. The subscript r denotes radiation. The input impedance of the antenna is Z_a . $V_t(r)$ is the voltage induced across the terminals of the antenna.

When the terminals of a receiving antenna are short-

circuited, the scattering antenna may be modelled with the simple circuit in Figure 2.

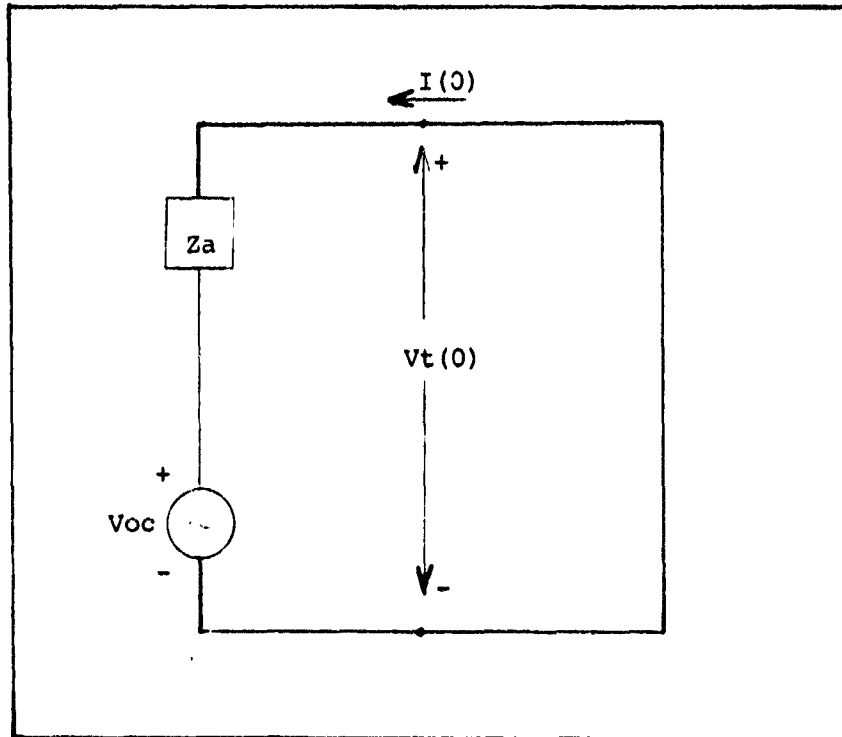


Figure 2. Short-Circuited Scattering Antenna
Source: [2]

For the short-circuited antenna, the terminal voltage, V_t , must be zero. The short-circuited terminal current is denoted $I(0)$. The voltage, V_{oc} , is the terminal voltage that would exist if the terminals were open-circuited. This is easily seen because no current would exist in the circuit model when the terminals are left open.

Now a general load impedance may be added to the antenna terminals to represent the input impedance of the radar warning receiver circuitry. This is shown in Figure 3, which follows.

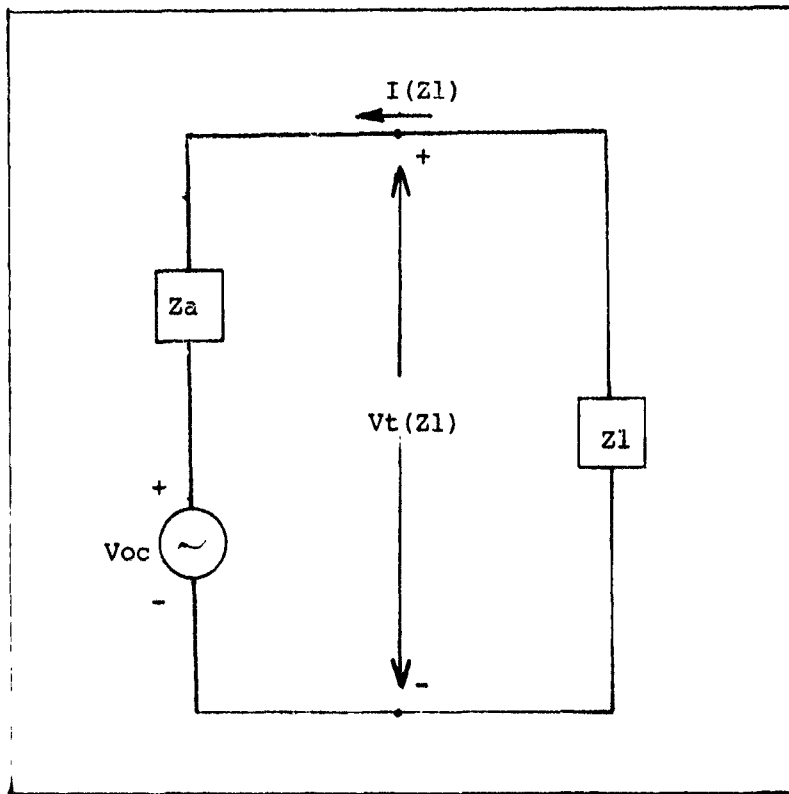


Figure 3. Loaded Scattering Antenna Model
Source:[2]

From simple circuit theory,

$$I(Zl) = -Voc / (Za + Zl) \quad (1-2)$$

From Figure 2, it is easily seen that

$$Voc = -Za * I(0) \quad (1-3)$$

Substituting equation (1-3) into (1-2),

$$I(Zl) = Za * I(0) / (Za + Zl) \quad (1-4)$$

Now the following linear equations may be written to describe the loaded terminal voltage and current in terms of the short-circuit and radiation voltages and currents.

$$I(Zl) = C1 * I(0) + C2 * Ir \quad (1-5)$$

$$Vt(Zl) = C1 * Vt(0) + C2 * Vt(r) \quad (1-6)$$

These equations are justified because each circuit model is linear and any signal which occurs at the terminals of the loaded scattering antenna (current or voltage) must be a linear combination of the terminal signals in the radiating and short-circuit models. Now $V_t(Z_1) = -Z_1 \cdot I(Z_1)$, $V_t(r) = Z_a \cdot I_r$, and $V_t(0)$ is zero. Therefore, equation (1-6) becomes

$$-Z_1 \cdot I(Z_1) = C_2 \cdot Z_a \cdot I_r \quad (1-7)$$

Substituting equation (1-7) into (1-5),

$$I(Z_1) = C_1 \cdot I(0) - Z_1 \cdot I(Z_1) / Z_a \quad (1-8)$$

$$\text{or } I(Z_1) \cdot (1 + Z_1 / Z_a) = C_1 \cdot I(0) \quad (1-9)$$

Substituting equation (1-4) into (1-9),

$$Z_a \cdot I(0) \cdot (1 + Z_1 / Z_a) / (Z_a + Z_1) = C_1 \cdot I(0) \quad (1-10)$$

This quickly reduces to $C_1 = 1$. Now from equation (1-5),

$$Z_a \cdot I(0) / (Z_a + Z_1) = I(0) + C_2 \cdot I_r \quad (1-11)$$

$$\text{or } (-1 + Z_a / (Z_a + Z_1)) \cdot I(0) = C_2 \cdot I_r \quad (1-12)$$

$$\text{or } C_2 = -Z_1 \cdot I(0) / (I_r \cdot (Z_a + Z_1)) \quad (1-13)$$

A similar linear combination is obtained for the scattered electric field from a loaded antenna. That is

$$\bar{E}_s(Z_1) = C_1 \cdot \bar{E}_s(0) + C_2 \cdot \bar{E}_r \quad (1-14)$$

where $\bar{E}_s(Z_1)$ = scattered electric field from antenna with load, Z_1

$\bar{E}_s(0)$ = scattered electric field from short-circuited antenna

\bar{E}_r = radiated electric field from antenna with a unit current driving source.

$$C_1 = 1$$

$$C_2 = -Z_1 \cdot I(0) / (I_r \cdot (Z_a + Z_1))$$

Therefore,

$$\bar{E}_s(Z_1) = \bar{E}_s(0) - Z_1 \cdot I(0) \cdot \bar{E}_r / (I_r \cdot (Z_a + Z_1)) \quad (1-15)$$

Suppose the load is the complex conjugate of the antenna impedance. Then

$$\bar{E}_s(Z_b) = \bar{E}_s(0) - Z_b \cdot I(0) \cdot \bar{E}_r / (2 \cdot R_a \cdot I_r) \quad (1-16)$$

where Z_b = complex conjugate of Z_a

R_a = real component of antenna impedance.

Now the scattered electric field from an antenna with a general load may be written in terms of the scattered field from an antenna with a conjugate matched load. Substituting equation (1-16) into (1-15),

$$\begin{aligned} \bar{E}_s(Z_1) = \bar{E}_s(Z_b) + Z_b \cdot I(0) \cdot \bar{E}_r / (2 \cdot R_a \cdot I_r) \\ - Z_1 \cdot I(0) \cdot \bar{E}_r / (I_r \cdot (Z_a + Z_1)) \end{aligned} \quad (1-17)$$

which may be rewritten,

$$\bar{E}_s(Z_1) = \bar{E}_s(Z_b) + (Z_b - Z_1) \cdot I(Z_b) \cdot \bar{E}_r / (I_r \cdot (Z_1 + Z_a)) \quad (1-18)$$

where $I(Z_b) = Z_a \cdot I(0) / (2 \cdot R_a)$, which comes from equation (1-4) when $Z_1 = Z_b$. The first term on the right hand side of equation (1-18), $\bar{E}_s(Z_b)$, is known as the structural mode scattering component [3:26]. The remaining term on the right hand side of equation (1-18) is the antenna mode scattering component [3:26]. It completely vanishes when the antenna load is conjugate matched to the antenna impedance.

The term, $(Z_b - Z_1) / (Z_a + Z_1)$, may be defined as the modified current reflection coefficient, R [3:26]. R is the same as a normal transmission line reflection coefficient when the antenna impedance is purely resistive.

Suppose the structural mode scattering component for

some antenna is exactly zero. Now all scattered fields arise from antenna mode scattering. The definition in equation (1-1) can be used to derive the RCS from antenna mode scattering.

$$\sigma = \lim_{r \rightarrow \infty} 4 \pi r^2 \frac{|\bar{E}_s(z_1)|^2}{|\bar{E}_i|^2}$$

$$\sigma = \lim_{r \rightarrow \infty} 4 \pi r^2 \frac{|R|^2 |I(z_b)|^2 |\bar{E}_r|^2}{|I_r|^2 |\bar{E}_i|^2} \quad (1-19)$$

Assume the antenna is used as a transmitter and the antenna load is conjugate matched to the antenna impedance (for optimum transmission). Now $I(z_b)$ is exactly I_r . The following manipulations can then be made to define the antenna mode RCS in terms of the transmitting antenna gain, G . The gain is defined as [1:37]

$$G = 4 \pi U / P_{in} \quad (1-20)$$

where U = radiation intensity

$$P_i = 3.14159265$$

P_{in} = antenna input power.

Since interest is primarily in monostatic RCS (that is, in the direction of backscatter), U should be found in the direction of backscatter. This is simply [1:33]

$$U = r^2 |\bar{E}_r|^2 / 2 \nu \quad (1-21)$$

where ν = free space impedance.

The input power to the antenna (for scattering) is merely the product of the incoming radiation intensity and the solid angle created by the effective aperture of the antenna. That is,

$$P_{in} = (r * |\bar{E}_i|^2 / 2 * \nu) * (A_e / r^2) \quad (1-22)$$

where $(r * |\bar{E}_i|^2 / 2 * \nu) =$ incoming radiation intensity

$A_e / r^2 =$ solid angle created by the effective aperture of the antenna

$A_e =$ effective aperture of the antenna.

Substituting equations (1-21) and (1-22) into (1-19),

$$\sigma = 4 * \pi * |R|^2 * U * A_e / P_{in} \quad (1-23)$$

Further substituting equation (1-20) into (1-23),

$$\sigma = |R|^2 * G * A_e \quad (1-24)$$

The effective aperture of the antenna can be expressed as

[1:61]

$$A_e = \lambda^2 * G / (4 * \pi) \quad (1-25)$$

where $\lambda =$ wavelength.

Therefore,

$$\sigma = |R|^2 * \lambda^2 * G^2 / (4 * \pi) \quad (1-26)$$

which is the simplest expression for the antenna mode RCS.

It is interesting to note that this expression completely vanishes when the modified current reflection coefficient goes to zero. Also, the antenna mode RCS is directly proportional to the square of the antenna gain in the backscatter direction. These mechanisms make sense because an antenna will receive and radiate power proportional to its gain and reradiation of incident power is a direct result of the current reflection (for antenna mode).

The structural mode scattering component arises from

the scattered field, $E_s(Zb)$, which is defined in equation (1-16). This scattered field can be put into equation (1-1) to form an RCS expression, but the result would only be a complicated RCS formula in terms of the short-circuit antenna conditions.

Literature Review

Several attempts have been made to describe the radiation properties of spiral antennas. One of the first was made by Walter Curtis in 1960 [4]. He concentrated on an Archimedian spiral as shown in Figure 4.

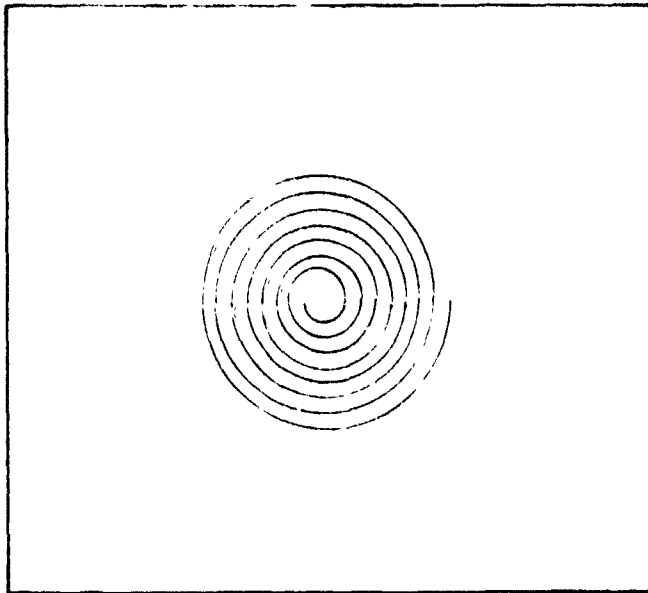


Figure 4. One Arm Archimedian Spiral

The geometry of this one arm antenna is characterized by the equation

$$r = r_0 + a \cdot \phi \quad (1-27)$$

where r = radial distance from the origin to any point on the spiral

ϕ = polar angle in the plane of the spiral
 r_0, a = constants.

Curtis's approach was to approximate the Archimedian spiral as a series of semicircles. He assumed a current distribution of the sum of outward and inward travelling waves, with a reflection coefficient at the open end of the spiral to account for the inward travelling wave. He then proceeded to solve the vector potential of a single semicircle in closed form. Once this was found, the radiation pattern for an entire arm was given by the sum of the contributions of the semicircles. Curtis made the analysis complete by including a second arm rotated 180 degrees physically from the first arm and driven with a current at the origin 180 degrees out of phase from the first arm current.

Curtis's work is limited in that it only concerns Archimedian spirals and assumed a current distribution on the antenna. The current distribution he used cannot be validated with theory or experimentation unless the antenna is extremely small with respect to a wavelength.

Cheo, Rumsey, and Welch [5] used Maxwell's equations to approach an exact solution for the radiation pattern of an antenna consisting of an infinite number of equally spaced wires in the form of coplanar equiangular spirals. This type of antenna is sometimes known as a logarithmic spiral and is characterized by the equation

$$r = e^{-a\phi} \quad (1-28)$$

where r = radial distance from origin to any point on the spiral

ϕ = polar angle in the plane of the spiral

a = constant of angle proportionality.

The solution obtained by Cheo, Rumsey, and Welch for the radiated electric field was a complicated integral expression involving Bessel functions. Using an asymptotic approximation for the Bessel functions, they obtained a somewhat simplified expression for the far-zone electric field. That expression is [5:530]

$$\left| \bar{E}_\phi \right| = \frac{\cos \theta (\tan \theta/2) e^{(1/a) \tan^{-1}(a \cos \theta)}}{\sin \theta \sqrt{1 + a^2 \cos^2 \theta}} \quad (1-29)$$

for a two arm logarithmic (equiangular) spiral in the x-y plane where

$\left| \bar{E}_\phi \right|$ = amplitude of phi-component of far-zone electric field

a = constant of angle proportionality

θ = angle from z-axis

ϕ = angle from x-axis projected on x-y plane.

The major limitation of their work was that it involved only radiation of the antenna. Cheo, Rumsey, and Welch did not predict the current causing scattering by the antenna.

K. K. Mei demonstrated the feasibility of numerically solving an integral equation that modelled the physics of a radiating equiangular spiral antenna [6]. He used Hallen's equation [7:79] to solve for the current distribution on the antenna, which he assumed was composed of a thin curved

wire. Mei's technique for solving the equation was essentially the method of moments, which is discussed in detail in Chapter 2. However, Mei's work may have been in vain, because Hallen's equation assumes the current distribution will have a constant phase velocity. This assumption proves to be poor when the wire has a small radius of curvature compared to a wavelength [8]. This is to be expected because the equation was originally developed for linear antennas.

Joseph Mosko discussed how a four arm spiral antenna can be used for direction finding applications, as in a radar warning receiver [9]. He showed that three different beam-forming modes may be found in the four arm antenna. These modes were formed by applying equal amplitude voltages with various phases to the four feed points.

The primary mode is known as the sum mode. It forms a large beam directly above the plane of the spiral. It is excited by generating equal amplitude voltages with phases of 0, -90, 180, and -270 degrees in a clockwise rotation about the four feed points. The sum mode creates a large current on the antenna around the region where the circumference of a loop is about one wavelength.

The other two modes are the azimuth and elevation difference modes. Together in quadrature, they form a single mode which is simply known as the difference mode. The difference mode is excited by equal amplitude voltages with clockwise feed-point phases of 0, 180, 0, and 180 degrees.

The difference mode is characterized by a large current on the antenna around the area where a loop circumference is approximately two wavelengths.

Mosko stated that direction finding is done by comparing the strengths of the antenna return through the three modes. This can be done for the passive antenna by using a network of phase shifters that may be implemented best with stripline [9:91].

CHAPTER 2

THE METHOD OF MOMENTS

Introduction

The method of moments, or moment method, may be simply described as a mathematical technique used to get an approximate solution to an integral equation. Such an integral equation may be in the form [1:306]

$$\int I(\bar{r}')K(\bar{r},\bar{r}')d\bar{r}' = -E^i(\bar{r}) \quad (2-1)$$

where \bar{r} = position vector in space
 \bar{r}' = position vector to any point on a scattering source.

This equation is actually a form of the electric field integral equation (EFIE), which is formulated from the boundary condition that the total electric field on the surface of a perfect conductor (scatterer) is zero. The term, $E^i(\bar{r})$, is the incident electric field on the scatterer. This term would usually be known. The unknown, $I(\bar{r}')$, is the current induced on the surface of the scatterer. The term, $K(\bar{r},\bar{r}')$, is referred to as the kernel of the equation, and will take on different forms for different problem geometries.

Expansion Functions

The method of moments assumes the unknown function in the integral equation may be approximated as a linear combination of some known functions. These known functions are called expansion functions or basis functions. They may

take many forms. In general, the unknown current function in equation (2-1) may be written [1:310]

$$I(\bar{r}') = \sum I_n F_n(\bar{r}') \quad (2-2)$$

In this form, n is the subscript for the n th expansion function, $F_n(\bar{r}')$. There are N total expansion functions. As will be seen later, allowing N to become large may give a more accurate representation of the unknown current function. I_n is the n th expansion coefficient, which may be a complex constant.

There are many forms an expansion function may assume. The choice is left to the user of the moment method. Perhaps the most simple is the pulse function. In this case, the prime coordinate space (scattering surface) is broken into N subsets. The n th expansion function can then be described as follows [1:310].

$$F_n(\bar{r}') = \begin{cases} 1 & \text{for } \bar{r}' \text{ in the } n\text{th subset} \\ 0 & \text{otherwise} \end{cases} \quad (2-3)$$

The pulse expansion function is conceptually simple to understand. However, it is usually a very inaccurate representation for an unknown function, unless many subsets are used. For example, suppose Figure 5 contains the actual current distribution on a thin wire antenna.

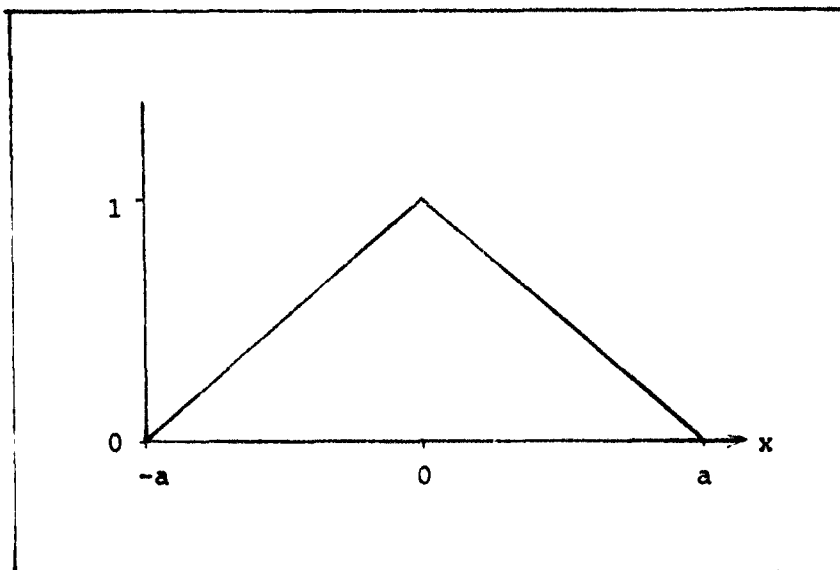


Figure 5. Example of Current Distribution

As can be seen in the figure, many pulse functions would be needed (at various heights) to accurately represent the actual distribution. To attempt to represent the distribution with only three pulse functions, as shown in Figure 6, is clearly a poor approximation.

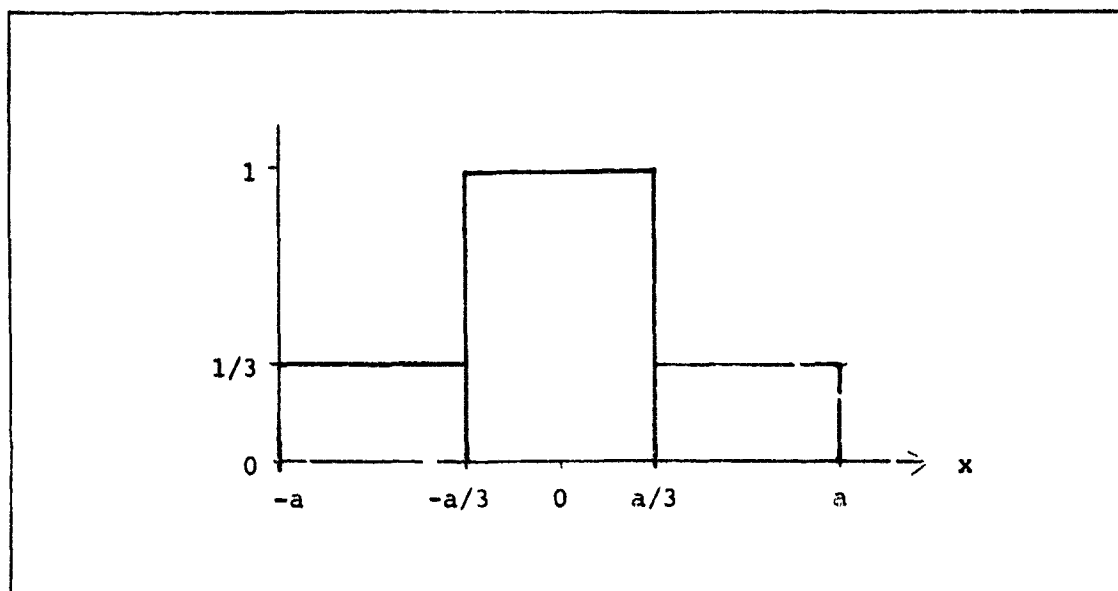


Figure 6. Three Pulse Approximation to Current Distribution

For the previous example, perhaps as many as one hundred pulse functions would be desired for an accurate representation of the function. The number of expansion functions needed to accurately represent the function can be substantially reduced by the choice of expansion functions. For example, a triangle function may be defined such that

$$F_n(x) = \begin{cases} \frac{-(x - (n-1)a)}{a} - 1 & \text{for } (n-1)a - 2a < x < (n-1)a \\ 0 & \text{otherwise.} \end{cases} \quad (2-4)$$

For this triangle function, a single expansion function ($n=1$) with an expansion coefficient of one would exactly represent the distribution.

The Piecewise Sinusoidal Expansion Function

One of the more popular expansion functions used in the method of moments is the piecewise sinusoidal function. It is characterized by the following equation [1:323].

$$F_n(x) = \begin{cases} \frac{\sin\beta(x-x_{n-1})}{\sin\beta(x_n-x_{n-1})} & \text{for } x_{n-1} < x < x_n \\ \frac{\sin\beta(x_{n+1}-x)}{\sin\beta(x_{n+1}-x_n)} & \text{for } x_n < x < x_{n+1} \\ 0 & \text{otherwise} \end{cases}$$

and

$$\beta = 2\pi/\lambda$$

$$\lambda = \text{wavelength.}$$

(2-5)

This function is shown on the next page in Figure 7.

The piecewise sinusoidal expansion function is usually spaced evenly so that $x_{n+1} - x_n$ is a constant for all n .

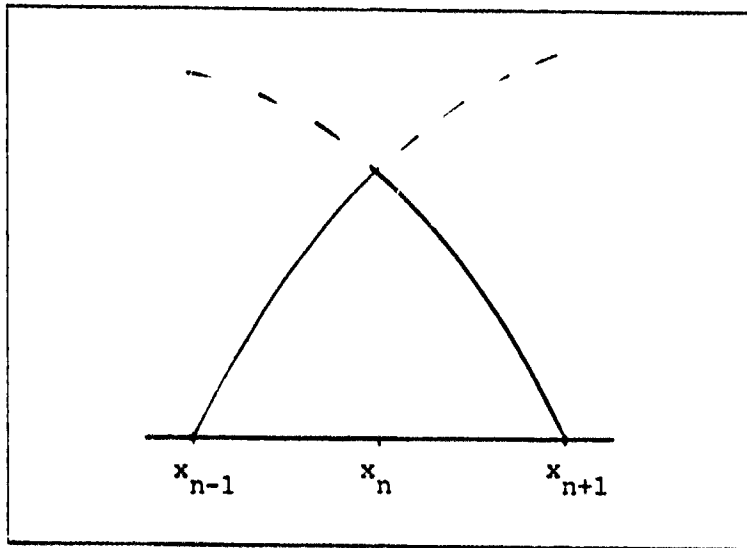


Figure 7. Piecewise Sinusoidal Function
Source: [1:324]

Furthermore, the functions overlap when they represent an unknown distribution. This is shown below in Figure 8.

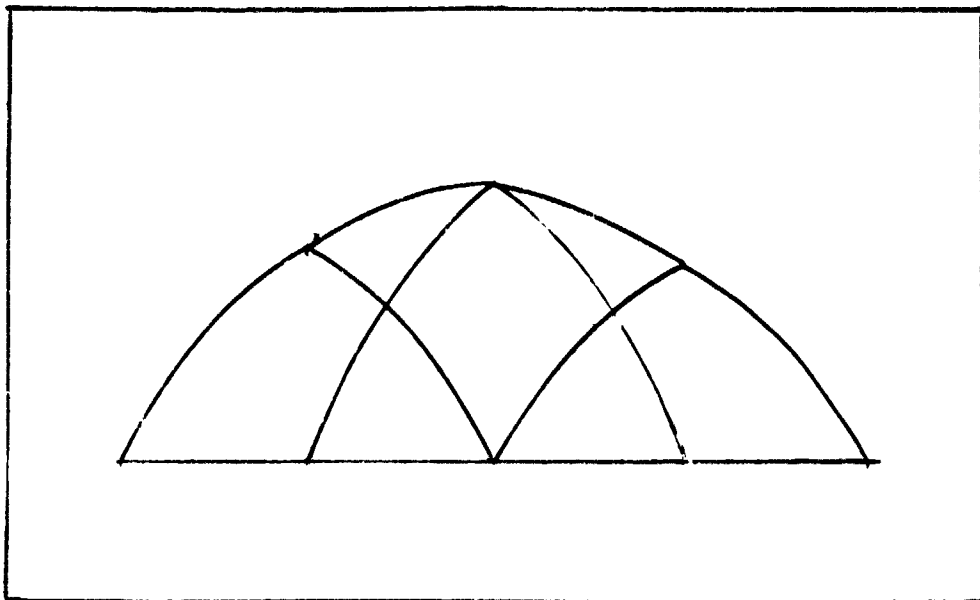


Figure 8. Overlapping Piecewise Sinusoidal Functions
Source: [1:324]

When $x_{n+1} - x_n$ is small compared to a wavelength,

the piecewise sinusoidal function approaches the triangle function described earlier.

Testing Functions

Once the unknown function in an integral equation is written as a linear combination of expansion functions with unknown coefficients, a testing procedure can be applied to convert the integral equation into a set of linear equations. For example, consider the integral equation (2-1) with the expansion functions of equation (2-2) substituted for the current distribution. That is

$$\int \sum_n F_n(\vec{r}') K(\vec{r}, \vec{r}') d\vec{r}' = -E^i(\vec{r}). \quad (2-6)$$

A general testing procedure is to multiply each side of equation (2-6) by some testing (or weighting) function and integrate over the unprimed coordinate space. The summation and double integration can then be interchanged to give

$$\sum_n \iint F_n(\vec{r}') G_m(\vec{r}) K(\vec{r}, \vec{r}') d\vec{r}' d\vec{r} = -\int E^i(\vec{r}) G_m(\vec{r}) d\vec{r} \quad (2-7)$$

where $G_m(\vec{r})$ = the mth testing function.

Suppose N testing functions are used. Now there are N equations, each of the form

$$\sum_n Z_{mn} = V_m \quad (2-8)$$

where

$$Z_{mn} = \iint F_n(\vec{r}') G_m(\vec{r}) K(\vec{r}, \vec{r}') d\vec{r}' d\vec{r}$$

$$V_m = -\int E^i(\vec{r}) G_m(\vec{r}) d\vec{r}.$$

In the application of the method of moments, all terms necessary to find Z_{mn} and V_m would either be known or assumed (the testing and expansion functions). The problem is then reduced to a matrix problem. This can be written as

$$[Z][I] = [V] . \quad (2-9)$$

$[Z]$ is the impedance matrix with entries, Z_{mn} , for the m th row and n th column. It is a square matrix of order N . $[I]$ is a single column matrix with the coefficient, I_n , in the n th row. $[V]$ is a single column matrix with V_m in the m th row. $[I]$ and $[V]$ each have N entries.

To solve the matrix problem, the impedance matrix must be inverted. The solution is written notationally as

$$[I] = [Z]^{-1}[V] \quad (2-10)$$

With the coefficients, I_n for $n = 1$ to N , found from equation (2-10), the unknown current distribution on the scattering surface is determined by equation (2-2).

The solution from the moment method is not necessarily the true current distribution on a scattering surface. It is only an approximation because the true continuous integral equation representing the physics is approximated by a set of discrete linear equations. The approximation becomes better when more linear equations are used to replace the integral equation. Hence, to get a better solution, more expansion and testing functions must be used.

Another approach to improving the moment method solution is to make intelligent choices for expansion and testing functions. As seen in Figures 5 and 6, the pulse func-

tion is not a very intelligent choice for an expansion function in some cases, unless many pulse functions are used. Using many pulse functions may seem like a reasonable approach, but this would create a large impedance matrix, which would be difficult to invert. In fact, the amount of computer time necessary to invert the impedance matrix and solve equation (2-10) is proportional to N^3 [1:340]. The computation time consideration makes an intelligent choice of expansion and testing functions to reduce the order of the impedance matrix, an attractive approach to a real moment method problem.

Point Matching

One of the easiest ways to implement the method of moments is to use point matching. This is just the name for the procedure of using delta functions for testing functions. These are defined below.

$$\delta(x-a) = 0 \text{ for all } x \neq a \quad (2-11)$$

$$\int_b^c \delta(x-a) dx = \begin{cases} 1 & \text{for } b < a < c \\ 0 & \text{otherwise} \end{cases} \quad (2-12)$$

The delta function also has the property that [10:273]

$$\int_{-\infty}^{\infty} \delta(x-a)f(x)dx = f(a) \quad (2-13)$$

for any function $f(x)$.

Point matching is used when N expansion functions are chosen so that each expansion function is non-zero over one of N subsets of the prime coordinate space (scattering surface). These subsets may overlap, but only one expansion

function can be non-zero at a particular point on each subset where point matching will be used. Either the pulse or piecewise sinusoidal functions may be used for the point matching procedure.

For an example of point matching, suppose a straight wire along the x-axis becomes a scatterer in a problem. The wire may be divided into N non-overlapping subsets and pulse expansion functions may be used for the induced current distribution on each subset. Point matching may be applied to the median location in each subset. These points would be designated x_n , where $n = 1$ to N.

Using the electric field integral equation in equation (2-1), the moment method gives the entries to the impedance and voltage matrices in equation (2-8). Now the mth testing function, $G_m(\vec{r})$, is just the delta function at x_m . That is

$$G_m(\vec{r}) = \delta(x-x_m). \quad (2-14)$$

Using the property of equation (2-13), the voltage matrix entries become

$$\begin{aligned} V_m &= -\int E^i(x) \delta(x-x_m) dx \\ &= -E^i(x_m) \end{aligned} \quad (2-15)$$

and the impedance matrix entries become

$$\begin{aligned} Z_{mn} &= \iint F_n(x') \delta(x-x_m) K(x, x') dx' dx \\ &= \int F_n(x') K(x_m, x') dx'. \end{aligned} \quad (2-16)$$

The main advantage of point matching is that entries for the voltage and impedance matrices may be found easier than if any other testing function were used. This is a

direct consequence of the property in equation (2-13), which removes one of the integrations required for computing each of the entries. This advantage makes point matching an attractive way to implement the method of moments when calculations are done by hand. However, if numerical integration can be performed on a computer, point matching does not offer significant advantages over other methods.

Point matching ensures that the original integral equation representing the physics of a problem is exactly satisfied at the point matching locations. What happens between these points is determined by the choice of expansion functions. As in all moment method procedures, accuracy in the solution will greatly increase when more expansion functions are used. In the case of point matching, this will mean the points where the solution is exact (integral equation is enforced) are close together.

Galerkin's Method

Another popular procedure used to implement the method of moments is Galerkin's method. This method can simply be described as the procedure of using the same functions for both expansion and testing functions.

One of the interesting applications of Galerkin's method is to use piecewise sinusoidal expansion and testing functions. Experience has shown that this procedure is both numerically efficient and highly accurate [1:324]. It is also possible to use Galerkin's method with other expansion

functions, such as the pulse function. However, experience has shown that the additional accuracy obtained by the pulse-pulse Galerkin procedure versus the pulse point matching procedure is not worth the extra effort [1:324].

In general, Galerkin's method will result in the minimum mean squared error for a given number and type of expansion function [2].

Reaction Integral Equation

The reaction integral equation is a convenient expression relating the reaction of various fields to each other for many problems. To understand the development of the equation, the concept of reaction must first be understood. This concept was developed by V. H. Rumsey in 1954.

Suppose there are two electromagnetic sources in an isolated universe. These sources can be denoted by the names, a and b. Suppose source a contains the electric and magnetic currents of $d\vec{J}(a)$ and $d\vec{K}(a)$, respectively, on some differential volume in the source. $\vec{E}(a)$ and $\vec{H}(a)$ can represent the electric and magnetic fields generated by source a. Similarly, $\vec{E}(b)$ and $\vec{H}(b)$ represent the fields generated by source b. Now the reaction of sources a and b, $\langle a, b \rangle$, can be defined below [11:1483].

$$\langle a, b \rangle = \iiint [\vec{E}(b) \cdot d\vec{J}(a) - \vec{H}(b) \cdot d\vec{K}(a)] \quad (2-17)$$

This integration is done over the volume of source a.

Using the reciprocity theorem [12:477], it follows that

$$\langle a, b \rangle = \langle b, a \rangle, \quad (2-18)$$

as long as the sources have finite volumes and the medium between the sources is isotropic.

The concept of reaction can now be applied to a moment method problem. Suppose a thin wire is a scatterer with a plane wave incident to induce an unknown current on the wire. The wire can be broken into a finite number of segments with pulse expansion functions representing the unknown current distribution. Let s denote the source of scattered fields and i denote the source of incident fields. Assuming the thin wire is a perfect conductor, the fields from s and i should equal zero on the surface of the wire. It is desired to have no reaction, or coupling, between the incident and scattered fields with a test source (the m th testing function, denoted m). Therefore

$$\langle s+i, m \rangle = 0. \quad (2-19)$$

This can be directly transformed by a property of reaction [11:1484] into

$$\langle s, m \rangle + \langle i, m \rangle = 0. \quad (2-20)$$

Using the definition of reaction, equation (2-17), this becomes

$$\iiint [\bar{E}_m \cdot d\bar{J}^s - \bar{H}_m \cdot d\bar{K}^s] + \iiint [\bar{E}_m \cdot d\bar{J}^i - \bar{H}_m \cdot d\bar{K}^i] = 0 \quad (2-21)$$

which is the reaction integral equation (RIE).

If a set of electric or magnetic test sources are used, the reaction integral equation reduces to the electric and magnetic field integral equations, respectively [13:6].

To obtain a more convenient form of the RIE for the method of moments, the property of equation (2-18) can be applied to the second term of equation (2-21). Therefore

$$\iiint [\bar{E}_m \cdot d\bar{J}^S - \bar{H}_m \cdot d\bar{K}^S] + \iiint [\bar{E}^i \cdot d\bar{J}_m - \bar{H}^i \cdot d\bar{K}_m] = 0. \quad (2-22)$$

Assuming a scatterer is almost a perfect conductor, the magnetic current causing scattering and the magnetic current on a test source (on the body) can be neglected. Now the RIE reduces to

$$\iiint \bar{E}_m \cdot d\bar{J}^S + \iiint \bar{E}^i \cdot d\bar{J}_m = 0. \quad (2-23)$$

The unknown in this equation is the current on the surface of the scatterer, $d\bar{J}_S$, which may be more conveniently written as $\bar{J}^S dV$. Equation (2-2) can be used to represent the unknown current distribution. Therefore,

$$\sum_{I_n} \iint \bar{E}_m \cdot \bar{F}_n dS + \iiint \bar{E}^i \cdot d\bar{J}_m = 0. \quad (2-24)$$

Note that it has been assumed that all scattering current will be on the surface of the scatterer. The voltage and impedance matrix elements may then be defined as follows.

$$V_m = \iiint \bar{E}^i \cdot d\bar{J}_m \quad (2-25)$$

$$Z_{mn} = -\iiint \bar{E}_m \cdot \bar{F}_n dV \quad (2-26)$$

These elements may be easily calculated once expansion and testing functions are assumed, and the electric field from the mth testing function, \bar{E}_m , is derived. This electric field may be computed by the standard radiation integral approach [1:25] on the source, \bar{J}_m . The solution to the E field for a piecewise sinusoidal testing function on a thin wire is known in closed form [14:368-370].

The form of the RIE in equation (2-23) can still be used if the conductor is not perfect, as long as it is a reasonably good conductor so that the magnetic current induced is small. The only modification to the previous

procedure is to add a small impedance term to the diagonal entries in the impedance matrix. This addition is simply the actual surface impedance on the mth subset (for the Z_{mm} entry) of the scatterer. This is the same impedance matrix modification used in lumped loading [1:345].

One of the main advantages of the RIE over the EFIE in equation (2-1) is the evaluation of the diagonal impedance matrix entries, Z_{mm} . In the EFIE, these terms become unstable, because the kernel of the equation (the free space Green's function) has a singularity. This singularity is avoided in computing Z_{mm} from equation (2-26).

The solution to the reaction integral equation only gets the current that causes scattering. Once this is found, the actual scattered fields from the surface may be obtained by the standard radiation integral approach of antenna theory [1:25]. The radar cross section of the scatterer can then be calculated using equation (1-1) with the range, r , some large finite number (unless the electric field is found by exact integration, in which case the range dependence will cancel in the RCS formula).

Radiation Problems

Although the entire chapter thus far has been devoted to applying the method of moments to scattering problems, the radiation problem of an antenna may also be approached. For this problem, the moment method only finds the current distribution driven on the antenna for radia-

tion.

The only difference between radiation and scattering problems is the source of the current distribution. For scattering problems, the source is an incident electric field. As shown in equations (2-8), (2-25), and (2-26), the incident field is used for voltage matrix entries only. This suggests that the impedance matrix entries are independent of the current distribution source, which is true. The same impedance matrix is used for both radiation and scattering problems on the same antenna. This makes sense because the impedance matrix entries are only mutual impedances between different subsets of the antenna.

There are several possible source models that can be used for radiation problems. The most popular for wire antenna radiation is the delta gap model [1:336] which is shown below in Figure 9.

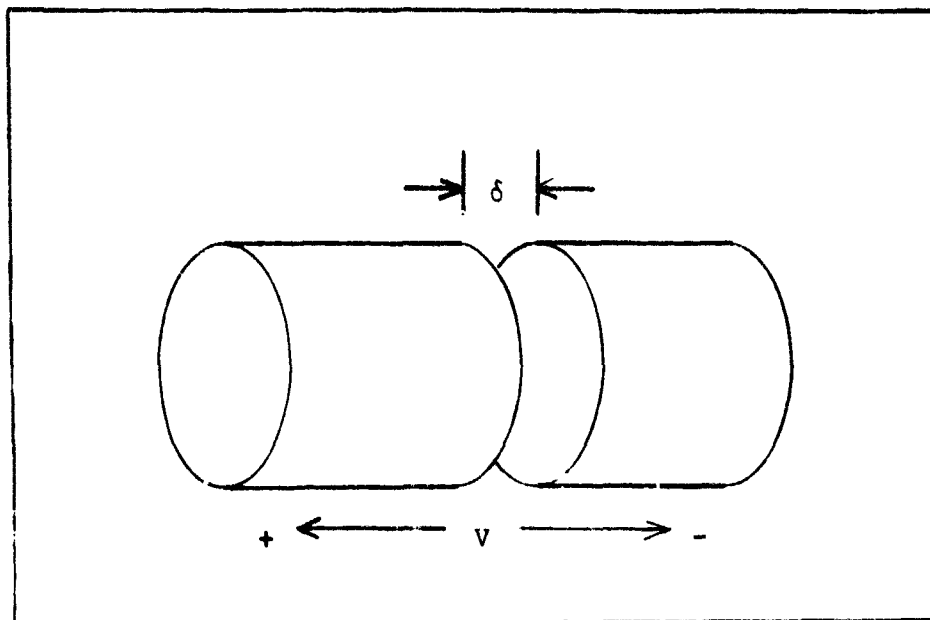


Figure 9. Delta Gap Model

What is shown in Figure 9 is one subset of a wire antenna in which a delta gap generator is found. The delta gap generator maintains a finite voltage over an extremely small gap. The same finite voltage is found across the entire wire subset. The delta gap generator has the advantage of making the calculation of the voltage matrix entries trivial. Each voltage matrix entry is simply the voltage across the corresponding segment of wire. Therefore, each entry is zero except for those for segments which have delta gap generators, in which case the finite voltage is the entry.

Regardless of how the sources are modelled in a radiation problem, the moment method procedure is to multiply the inverted impedance matrix and the source-obtained voltage matrix. This will give the coefficients for the expansion functions representing the current distribution. This current distribution can be translated into the radiated field pattern through the standard radiation integral technique [1:25].

CHAPTER 3

Computer Modelling

This project makes use of the Electromagnetic Surface Patch (ESP) Code, Version II - Polygonal Plates and Wires. This code was chosen for its versatility in creating a quadrilateral patch antenna model which accurately models the structural mode scattering. This is further explained later in this chapter.

The antenna to be modelled in this study is a four arm planar equiangular (logarithmic) spiral composed of flat curving strips. The strips flange outward as the radius of the spiral increases to help preserve the frequency independence of the antenna. The feed to the four arms of the antenna is hidden inside an electromagnetic shield.

Thin Wire Modelling

The first and most simple model considered for the antenna is the thin wire model. This model consisted of straight thin wire segments to approximate the median curve of the arm strips. Straight segments are used because the exact radiation pattern from a straight segment with a piecewise sinusoidal distribution of current is known. The first thin wire model used was a two arm model, in which two opposite arms of the four arm antenna were left out. This is shown on the next page in Figure 10.

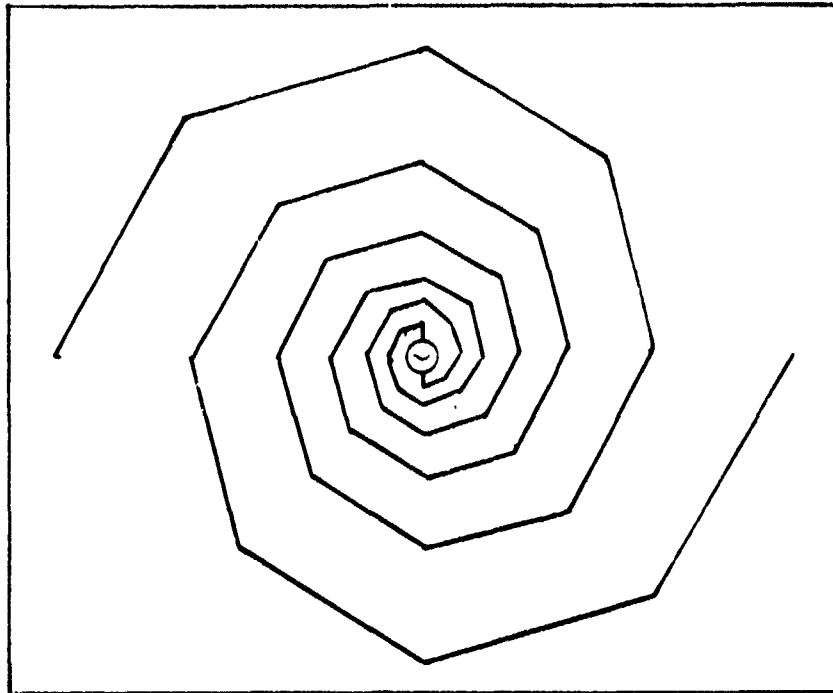


Figure 10. Two Arm Thin Wire Model

The feed for this model is a pair of collinear segments with a delta gap generator in the middle. The feed must be constructed in this manner because delta gap generators must be placed on the ends of wire segments in the ESP code. This feed is only accurate for frequencies where it is small compared to a wavelength. The two arm model was constructed to inspect the frequency characteristics of the flat spiral. However, the upper cutoff of the frequency band could not be checked because the feed is not a good model for smaller wavelengths. In other words, the feed corrupts the high frequency performance near the center of the spiral.

A four arm thin wire model was developed to determine

far field radiation patterns and current distributions from feed excitations. The four arm thin wire model consisted of short (less than a quarter wavelength) segments spaced at ten degree increments of rotation. In other words, 36 segments formed a loop in one arm. This is illustrated below in Figure 11.

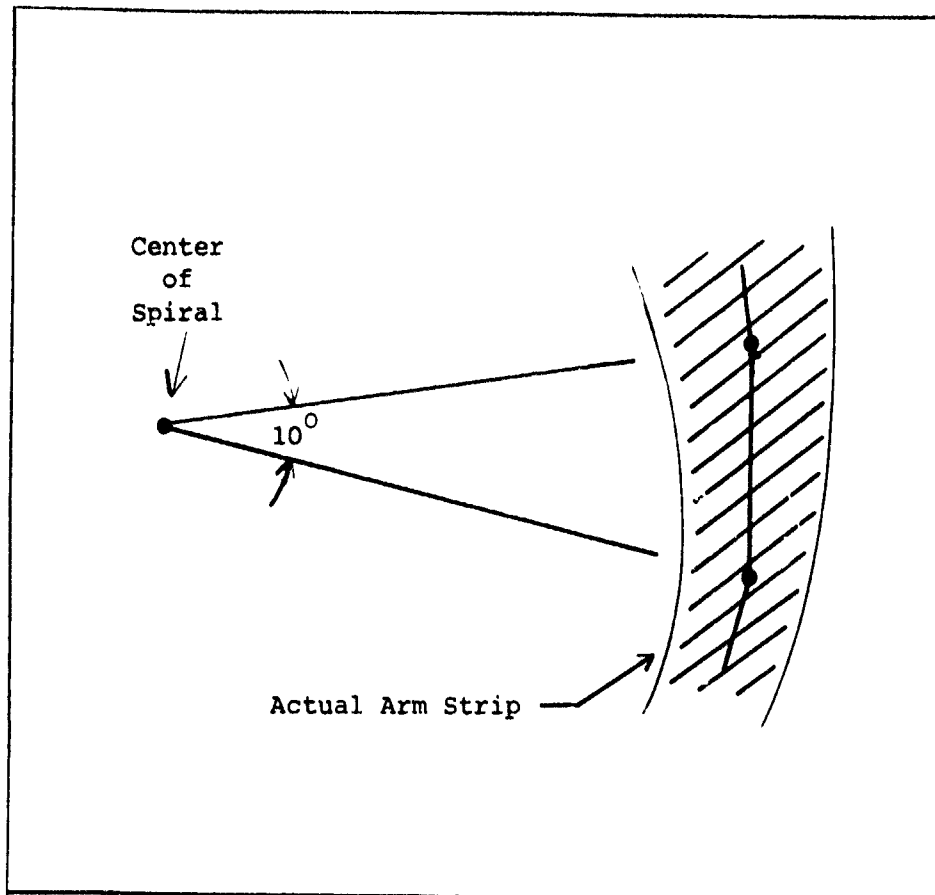


Figure 11. Thin Wire Modelling

Figure 11 also shows the way the thin wire modelling approximates the median curve of the arm strips. In the original modelling with thin wires, the ends of each of the arms was left as an open circuit. That is, the out-most segment of the arm merely terminated in free space. Wire

segments were assumed to be perfect conductors and no impedances were introduced in the arms. However, as computer experimentation evolved, a loading impedance was added to each arm, and is discussed in the next chapter.

The in-most segment of each arm was connected to a feed system, shown below in Figure 12.

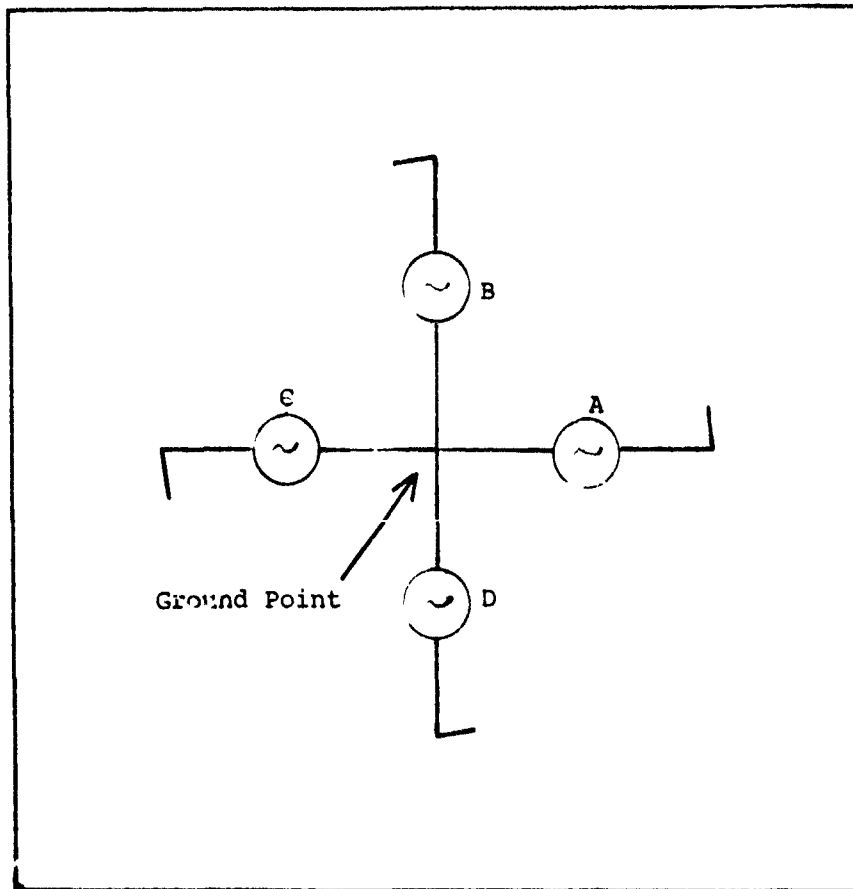


Figure 12. Feed System

The feed system model consisted of eight thin wire segments and four delta gap generators. Eight segments had to be used because the ESP code allowed delta gap generators to be placed only on an endpoint of a segment.

This feed model offered geometrical symmetry and the versatility of quickly interchanging feed voltages to produce different modes of radiation. The feed voltages to produce the sum and difference modes of radiation, as described in the first chapter, are given below in Table I.

Table I
Feed Voltages

| Feed Arm | Sum Patt. Vol. (V) | Diff. Patt. Vol. (V) |
|----------|----------------------------------|----------------------------------|
| A | 1 $\underline{\angle 0^\circ}$ | 1 $\underline{\angle 0^\circ}$ |
| B | 1 $\underline{\angle 90^\circ}$ | 1 $\underline{\angle 180^\circ}$ |
| C | 1 $\underline{\angle 180^\circ}$ | 1 $\underline{\angle 0^\circ}$ |
| D | 1 $\underline{\angle 270^\circ}$ | 1 $\underline{\angle 180^\circ}$ |

A subroutine listing the geometry input for this model (four arms) is given in Appendix A.

Wire Grid Modelling

A wire grid model was developed to check if transverse currents could be formed on the arms to significantly affect the radiation patterns. Figure 13, on the next page, shows the concept of wire grid modelling of the arms.

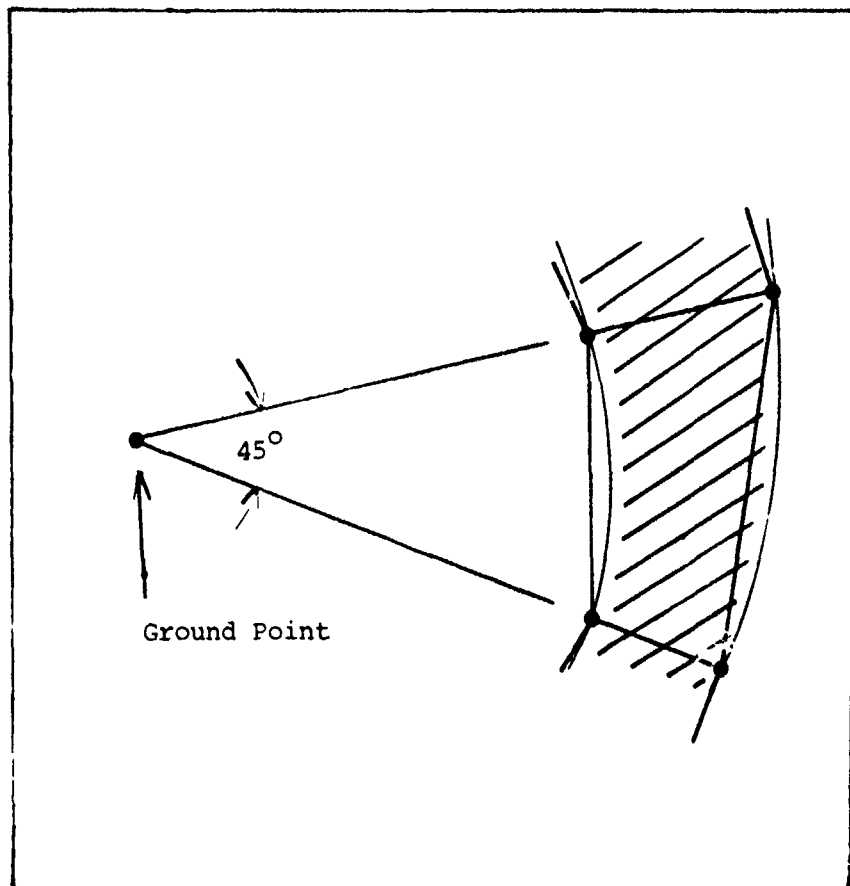


Figure 13. Wire grid Modelling

As seen in the figure, the wire grid model is a set of straight wire segments connecting points chosen on the inner and outer edges of the arm strips. The points are chosen at polar increments of 45 degrees by using empirical logarithmic equations derived to closely fit the actual strip edges. The polar increment angle (45 degrees) was increased from the thin wire model (in which it was 10 degrees) because the wire grid model used more expansion modes with its cross hatches.

The empirical equations for the inner and outer edges of the strips are given as follows.

$$\text{Inner Edge } R = 0.00395*(10.**{(0.00108*PHI)}) \quad (3-1)$$

$$\text{Outer Edge } R = 0.004437*(10.**{(0.00106*PHI)}) \quad (3-2)$$

where R = polar radial distance in meters

PHI = polar angle in degrees.

Since the model is considered to be in the X-Y plane, the point coordinates are given by the following equations.

$$x = R*\cos(PHI) \quad (3-3)$$

$$y = R*\sin(PHI) \quad (3-4)$$

$$z = 0 \quad (3-5)$$

For the radiation of the wire grid model, the same feed system used in thin wire modelling is used (ref. Fig. 12). The feed system is connected to each arm in the manner shown in Figure 14.

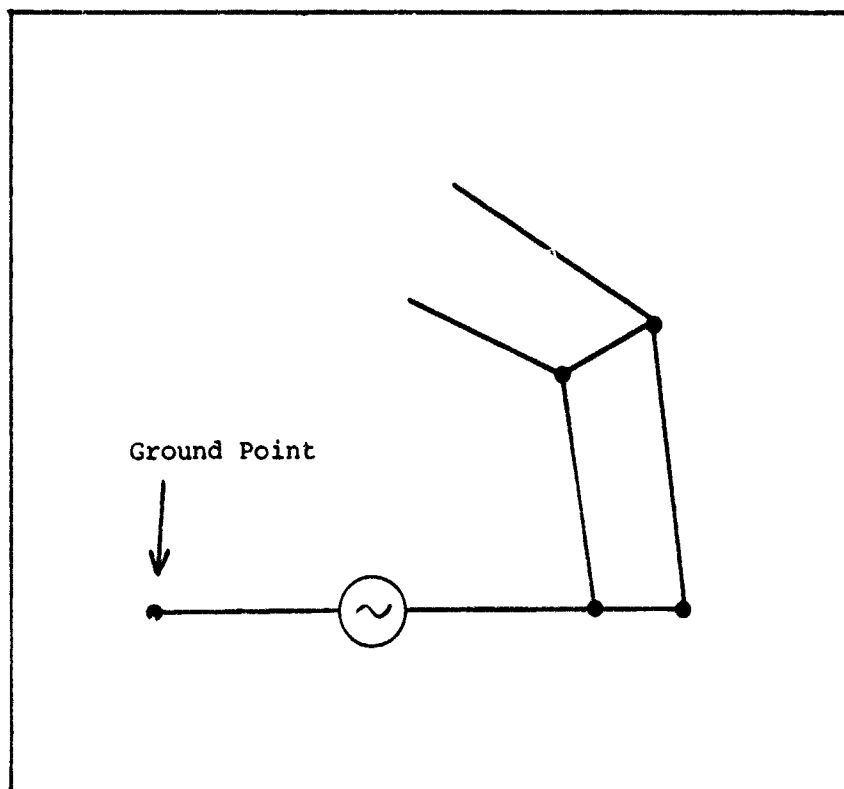


Figure 14. Wire Grid Feed Connection

It should be noted that the ground point is at the origin of a Cartesian coordinate system while the wire grid model lies in the X-Y plane. This is similar to the geometry of the thin wire model. A subroutine listing for the geometry input of this model is given in Appendix B.

Patch Modelling

The third model considered is the patch model. It consists of thin quadrilateral coplanar plates which conform to the shape of the actual arm strips. The corners of the quadrilaterals are the same as the points used in the wire grid model. The centers of the segments of wire in the wire grid model are the edges for the quadrilateral patches. Therefore, the wire grid modelling in Figure 13 also demonstrates the geometry of patch modelling.

The success of patch modelling is highly dependent on the ability to calculate the mutual impedance terms that determine the impedance matrix. The difficulty in finding the patch to patch impedances constrains the computation time dramatically. This is very different from the cases of thin segment impedances, which can be computed by a line integral of a simple dot product (ref. eq. 2-26). In these cases (e.g. thin wire modelling and wire grid modelling) the impedance matrix inversion (ref. eq. 2-10) dominates the computation time for the computer.

In order to understand the impedance matrix entries of the patch model, the expansion functions should first be

studied. The expansion function for patches used in the ESP code is a modified version of the piecewise sinusoidal function. It is defined by

$$J_s = c \hat{l} \frac{\sin kl}{\sin kL} \quad (3-6)$$

where $k = 2\pi/\lambda$

The terms in equation (3-6) are illustrated in Figure 15, which gives the surface patch geometry.

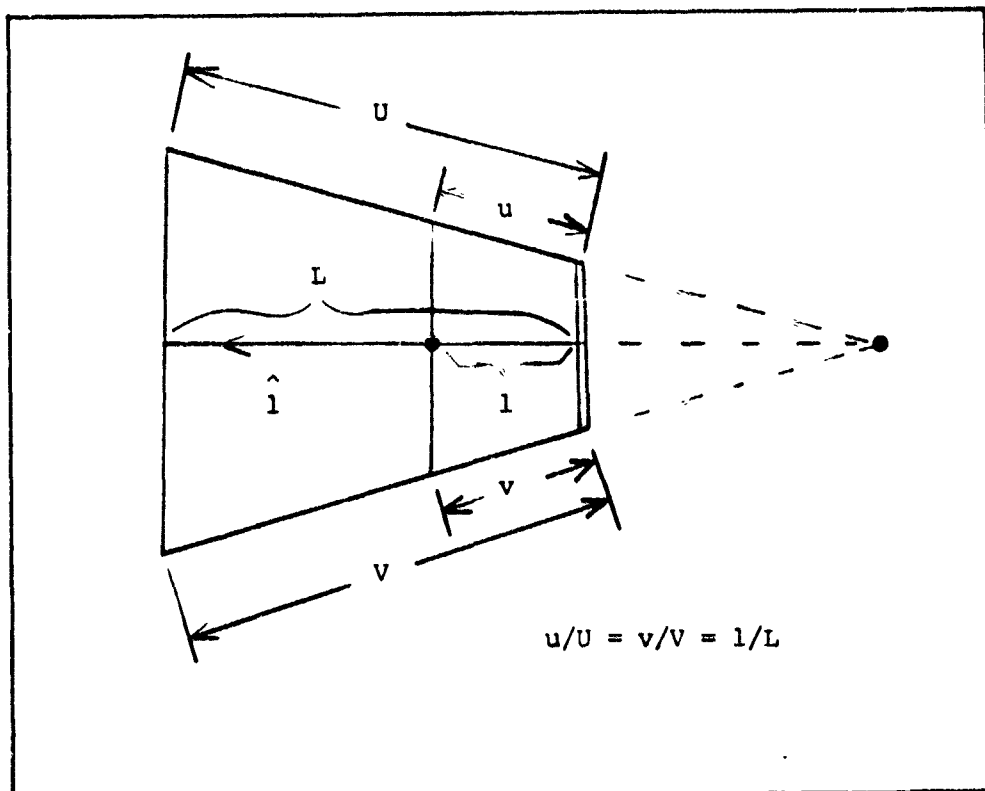


Figure 15. Surface Patch Geometry
Source: [13:12]

The constant, c , in equation (3-6) is chosen so that the expansion function has an amplitude of one ampere all along the edge of the patch marked with a double line.

The impedance entry calculation involves the surface integral of a dot product of the modified expansion function in equation (3-6) with the electric field radiated by another patch with a similar expansion function representing its current distribution. There are two reasons why this impedance calculation is much more difficult than wire to wire impedance calculations. First, integration must be done over two dimensions instead of one. And second, the radiated electric field from this modified piecewise sinusoid is not as simple as the radiated electric field from a thin wire segment.

To illustrate the enormous amount of computation required to solve patch model problems, the following experiment was devised. The ESP code was used to produce radar cross section results for some patch models. The first model was simply one patch conforming to the first (most inward) patch of one arm of the antenna (ref. Fig. 1⁴). The second model was the first two patches of one arm of the antenna. The final models used five and ten patches of one arm. Table II, on the next page, gives the CPU (central processing unit) computation time for a VAX 11/750 computer to get similar RCS data on each of these models.

Table II

Patch Model Computation Time

| # Patches in Model | CPU Time |
|--------------------|------------|
| 1 | 1 minute |
| 2 | 6 minutes |
| 5 | 46 minutes |
| 10 | 8 hours |

To adequately model the entire antenna, 88 patches are necessary (at 45 degree polar angle increments). Since the computation time grows almost exponentially with the number of patches, a very conservative estimate of the time required to get RCS data of the full antenna is over two weeks of CPU time. With time sharing, the actual calculation could be much longer.

It is a shame that full patch modelling of the antenna is not feasible, since it is believed the patch model would most accurately represent the structural mode scattering of the antenna's RCS.

An explanation of how the main program of the ESP code is altered to handle patch modelling, along with a sample patch generating subroutine, is given in Appendix C.

Chapter 4

Results

The first model used for experimentation was the two arm thin wire model shown in Figure 10. The purpose of this experiment was to verify the lower frequency cutoff of 1 GHz for the spiral antenna. This corresponds roughly to the frequency where one wavelength equals the outer circumference of the antenna. Table III gives the maximum gain (along the z axis as the antenna sits in the X-Y plane) of the theta and phi components of radiation of this model for various frequencies. In this study, the theta and phi components are from the standard spherical coordinate system with theta being the angle from the x axis of a projection on the X-Y plane [15:364].

Table III

Gain of Components in Two Arm Model

| Frequency (MHz) | Theta Comp. Gain (dB) | Phi Comp. Gain (dB) |
|-----------------|-----------------------|---------------------|
| 250 | 1.094 | -7.527 |
| 500 | 1.031 | -4.705 |
| 1000 | -2.101 | 1.099 |
| 1500 | -6.307 | 3.173 |
| 2000 | 1.663 | 0.944 |
| 3750 | 3.043 | 2.404 |

To check the bandwidth of this circularly polarized antenna, it is better to determine whether the antenna is polarized

left hand or right hand and then find the maximum gain of that component. This can be done by taking the square root of the sum of the squares of the components of the fields. To do this, the field first must be found by converting gain from decibels by the formula

$$\text{Gain} = 20 * \ln (\text{FS}) \quad (4-1)$$

where FS = field strength.

This is done to get the field strength of the components, and once the field strength of circular polarization is found, the formula can be used to reconvert into decibels. The result is shown in Table IV.

Table IV

Gain of Circular Polarization (Two-Arm Model)

| Frequency (MHz) | Circ. Pol. Gain (dB) |
|-----------------|----------------------|
| 250 | 4.62 |
| 500 | 5.50 |
| 1000 | 6.56 |
| 1500 | 6.45 |
| 2000 | 8.24 |
| 3750 | 9.66 |

Assuming the maximum gain is about 9.66 dB, the antenna bandwidth cutoff gain should be around 6.66 dB, which is 3 dB lower. This is almost exactly what happens at 1 GHz. Therefore, the cutoff limit of a wavelength fitting the outer circumference has been demonstrated.

Since the validity of the ESP code has been

demonstrated with the two arm model, the four arm thin wire model was used for experimentation. The sum patterns for the phi and theta components of polarization are shown for a frequency of 2 GHz in Figures 16 and 17. The maximum gain for the phi and theta polarizations are 3.328 dB and 3.330 dB, respectively. The bandwidths (3 dB) of the phi and theta polarizations are 68.2 and 66.6 degrees, respectively.

SUM PATTERN AT 2GHZ. PHI=0

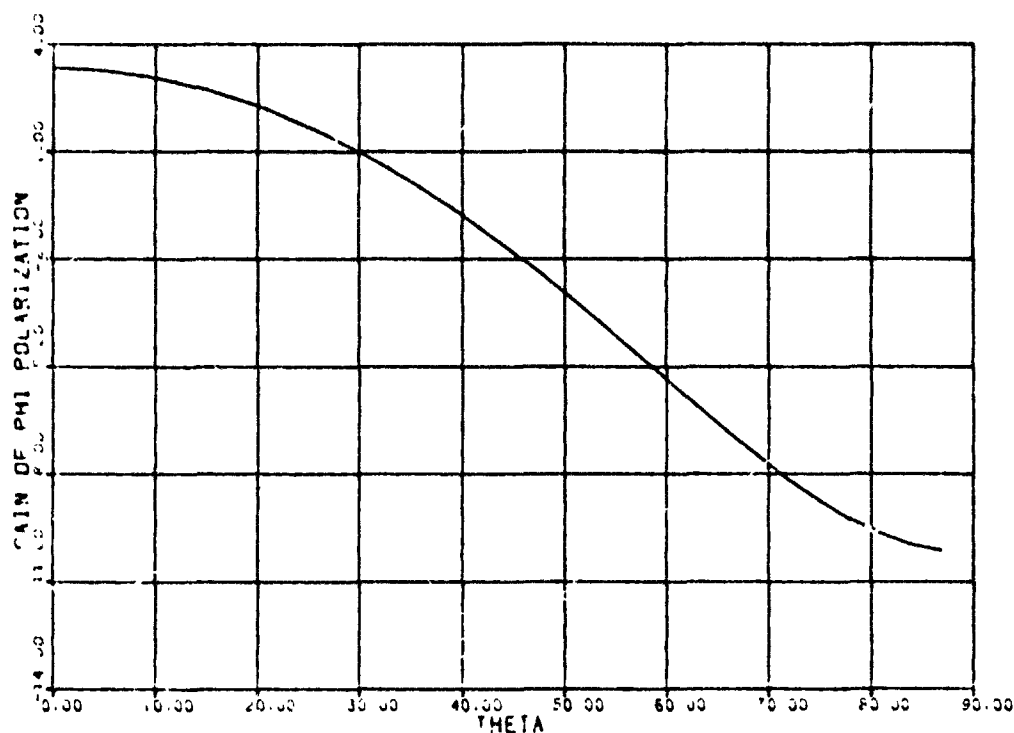


Figure 16.

SUM PATTERN AT 2 GHZ, PHI=0

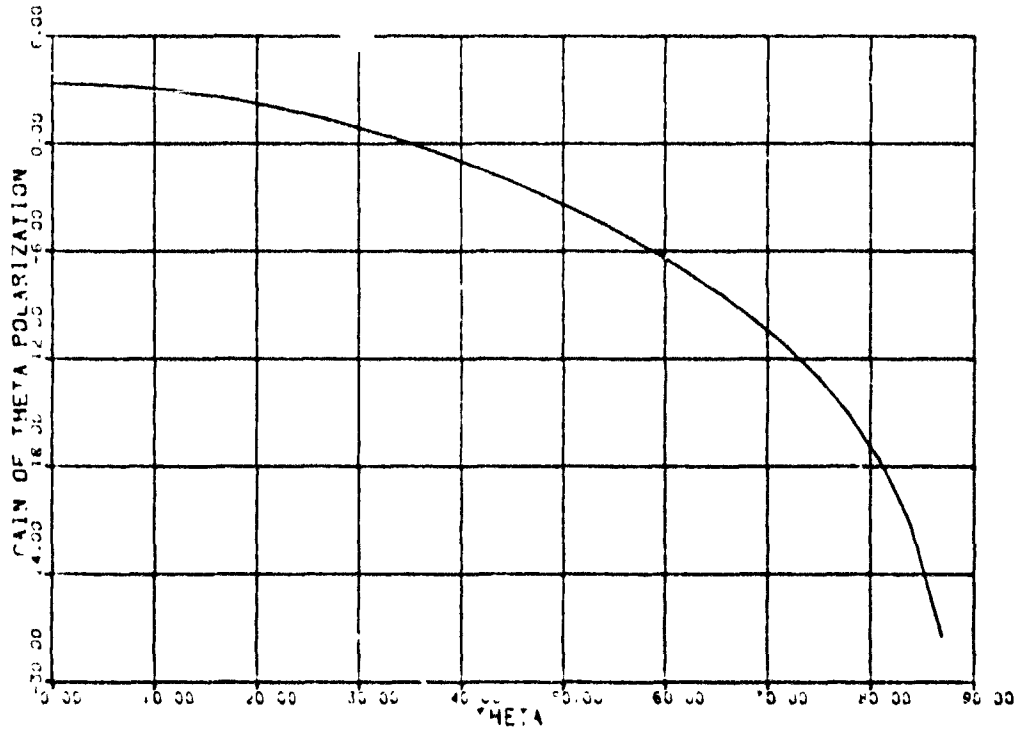


Figure 17.

Figures 16 and 17 seem to suggest that the linear polarization independence of a four arm spiral breaks down for large angles off the antenna boresight (the z axis).

The difference patterns for the phi and theta components of radiation at 2 GHz is shown in Figures 18 and 19.

DIFF. PATTERN AT 2GHZ. THIN. PHI=0

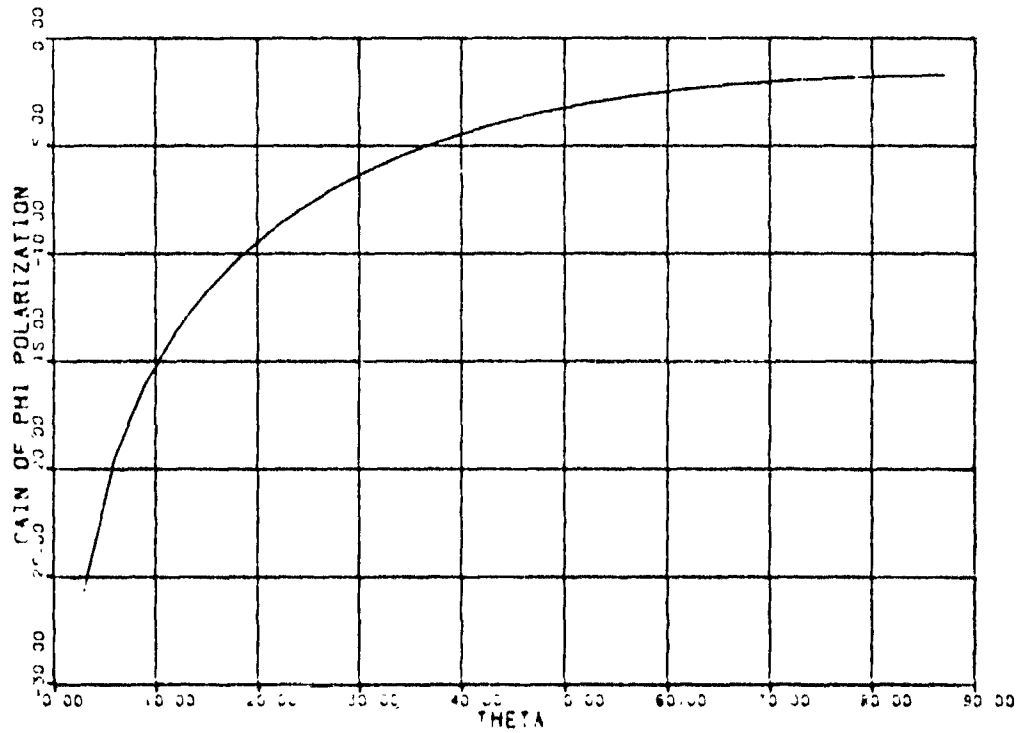


Figure 18.

DIFF. PATTERN AT 2GHZ. THIN. PHI=0

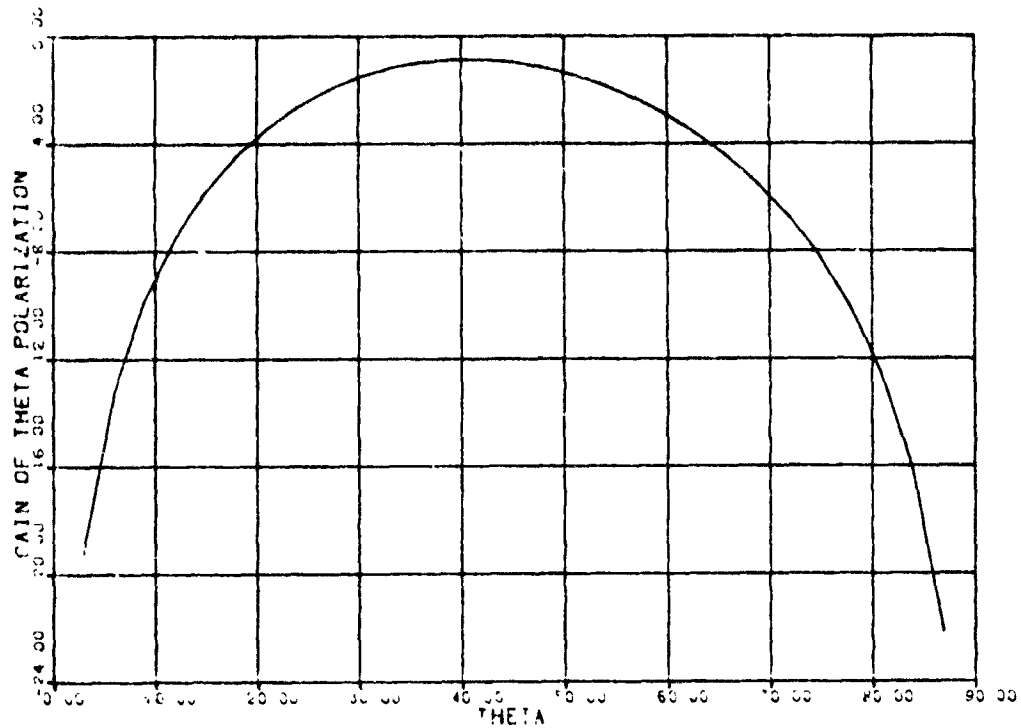


Figure 19.

Figures 18 and 19 also show a dramatic breakdown in the polarization independence beyond 60 degrees from the z axis. The theta polarization pattern, Figure 19, shows a maximum gain at about 42 degrees from the z axis. This agrees well with the 38 degree maximum typically observed in experiments [8:92].

Figures 20 through 23 show the difference patterns of the thin wire model for different planes of observation. Instead of looking in the X-Z plane ($\phi=0$), these patterns are taken 45 degrees from the X-Z plane and 90 degrees from the X-Z plane, which is the Y-Z plane. These figures indicate the patterns in the Y-Z plane (Fig. 22 and 23) are almost exactly the same as those in the X-Z plane (Fig. 18 and 19). But the patterns at $\phi = 45$ degrees are different. The pattern at $\phi = 45$ degrees for theta polarization is shaped the same as that for $\phi = 0$ or 90 degrees. However, the theta polarization pattern at 45 degrees is shifted about 6 dB lower than the other patterns. This suggests that a three dimensional view of the theta component of the difference pattern is a "warped donut" with valleys between the principal planes. Unfortunately, this illustrates the antenna has less than perfect circular symmetry.

The pattern at 45 degrees for the phi polarization (Fig. 20) is about 2 dB higher than its counterparts. This "reverse shift" also indicates there is a relative polarization breakdown in the difference pattern as the

azimuth is changed. In other words, the difference between the gains of the two polarization components in the difference pattern changes as the plane of observation is rotated.

DIFF. PATTERN AT 20HZ, THIN, PHI=45

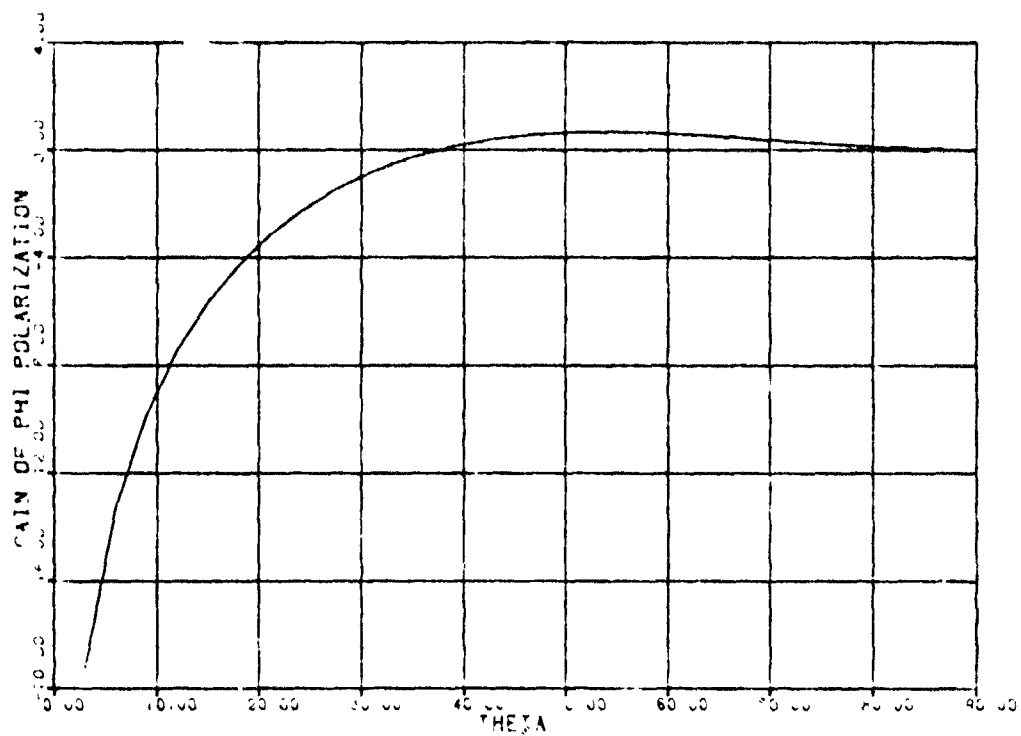


Figure 20.

DIFF. PATTERN AT 2GHZ. THIN. PHI=45

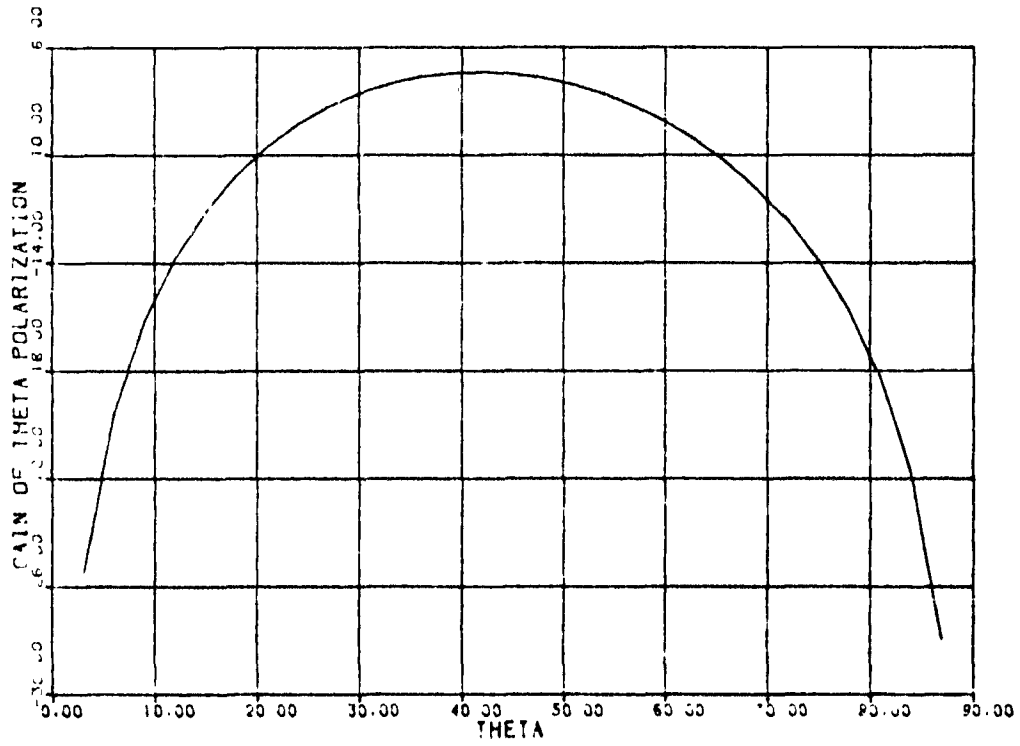


Figure 21.

DIFF. PATTERN AT 2GHZ. THIN. PHI=90

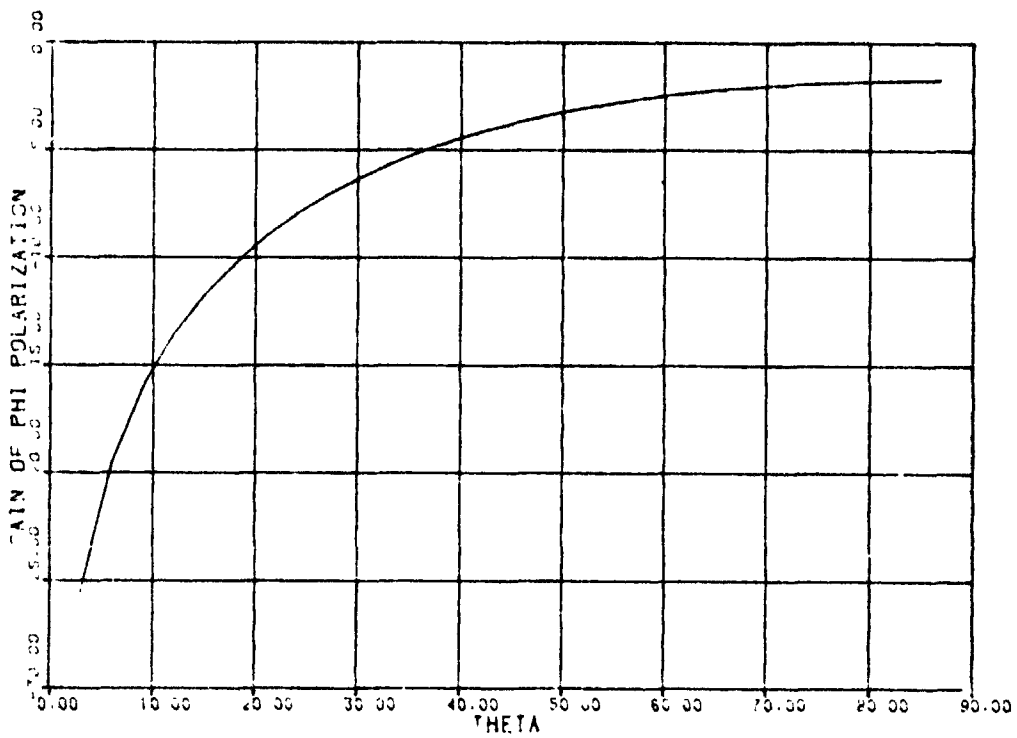


Figure 22.

DIFF. PATTERN AT 2GHZ. θ_{MIN} . $\phi=90$

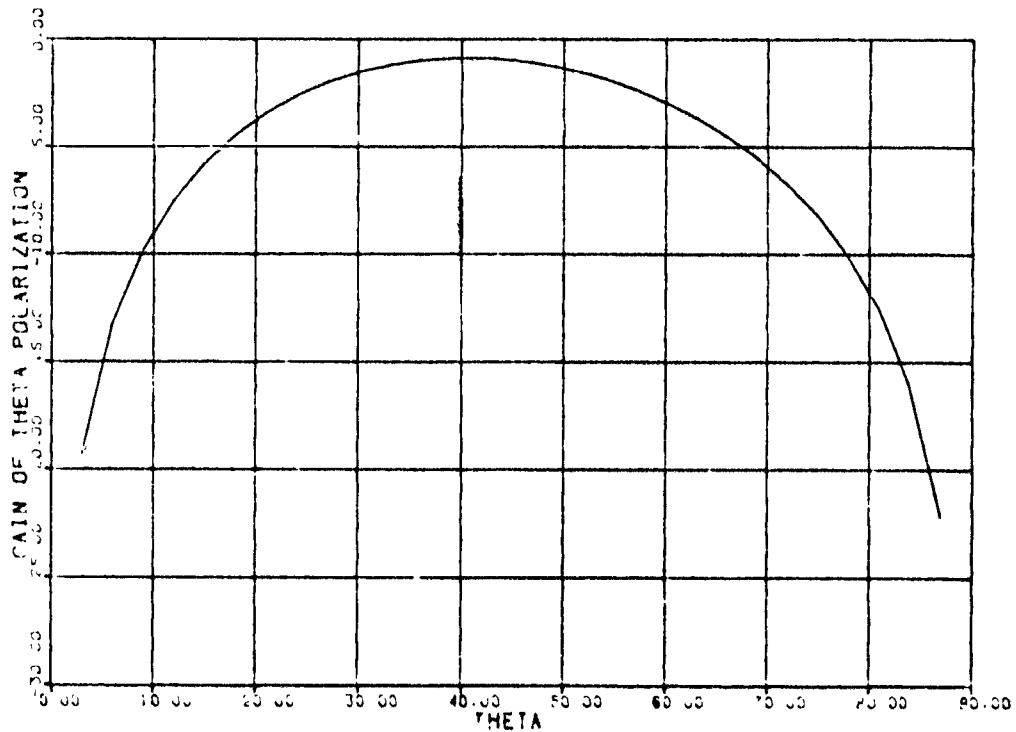


Figure 23.

Figures 24 through 27 show the sum and difference patterns at 2 GHz for the wire grid model. The maximum gain of the sum patterns for the phi and theta polarizations are 2.582 dB and 3.545 dB, respectively. This is close to the 3 dB maximum linear polarization gain expected from a spiral antenna. The beamwidths (3 dB) for the phi and theta sum patterns are 71.0 and 64.7 degrees, respectively.

GRID MODEL. 2GHZ. SUM PATTERN

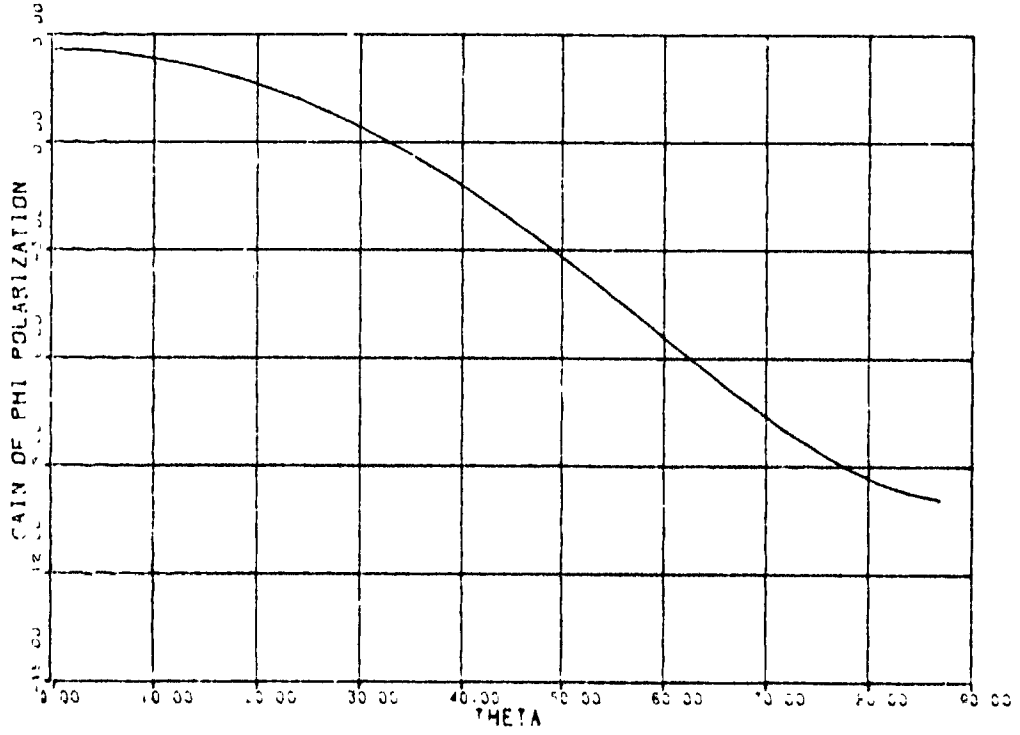


Figure 24.

GRID MODEL. 2GHZ. SUM PATTERN

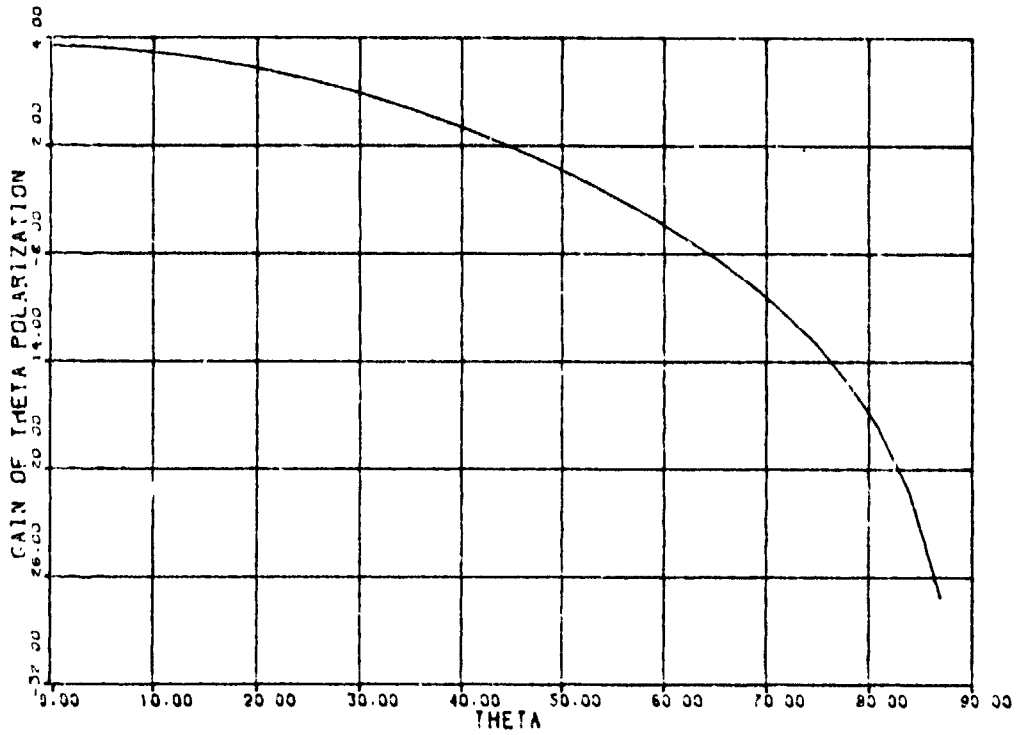


Figure 25.

GRID MODEL, 1.0CHZ, DIFF. PATTERN

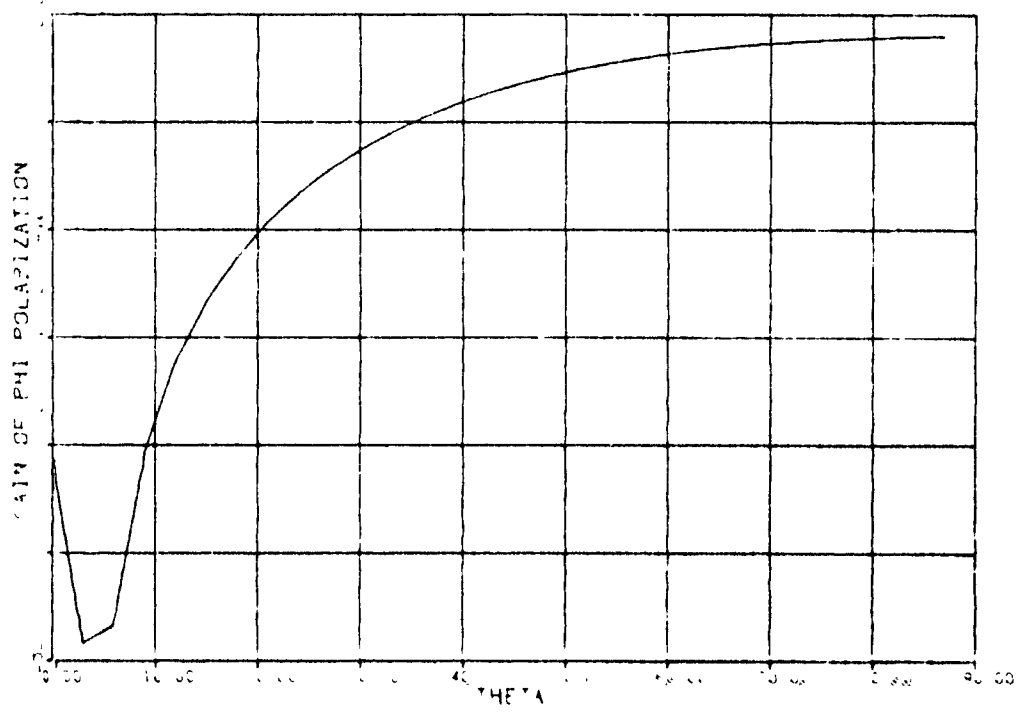


Figure 26.

GRID MODEL, 1.0CHZ, DIFF. PATTERN

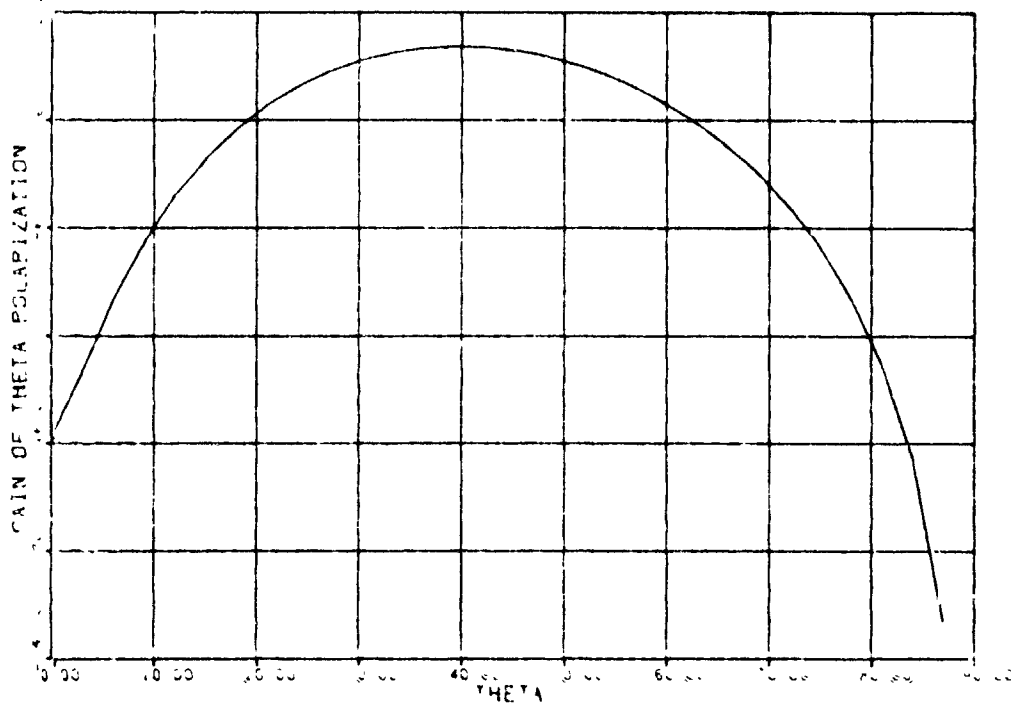


Figure 27.

Overall, the wire grid model results are very similar to the thin wire model results. There is a slight discrepancy in the phi polarization difference patterns. The wire grid result (Fig. 26), which is taken in the X-Z plane, shows a measurable gain on the z axis. This behavior is unexplained.

Figures 28 through 31 and 32 through 35 show more wire grid model patterns at 1 GHz and 3.75 GHz, respectively. All patterns are taken in the X-Z plane.

GRID MODEL 1 GHz PH POLARIZATION PATTERN

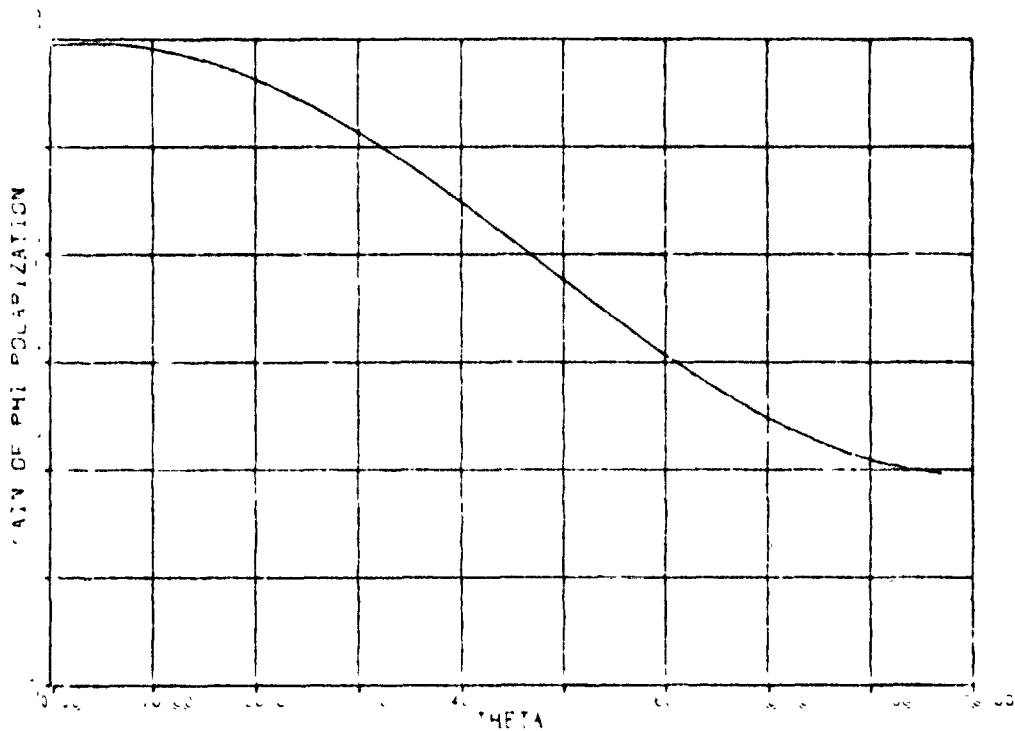


Figure 28.

GRID MODEL, 1642, LCM PATTERN

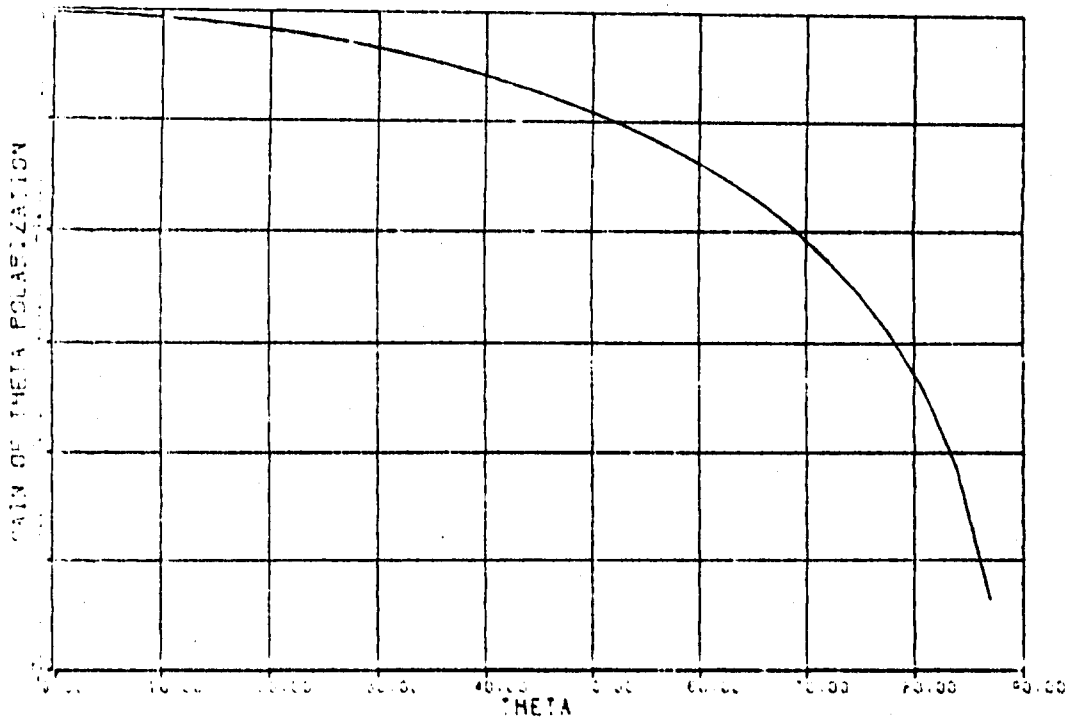


Figure 29.

GRID MODEL, 1642, DIFF. PATTERN

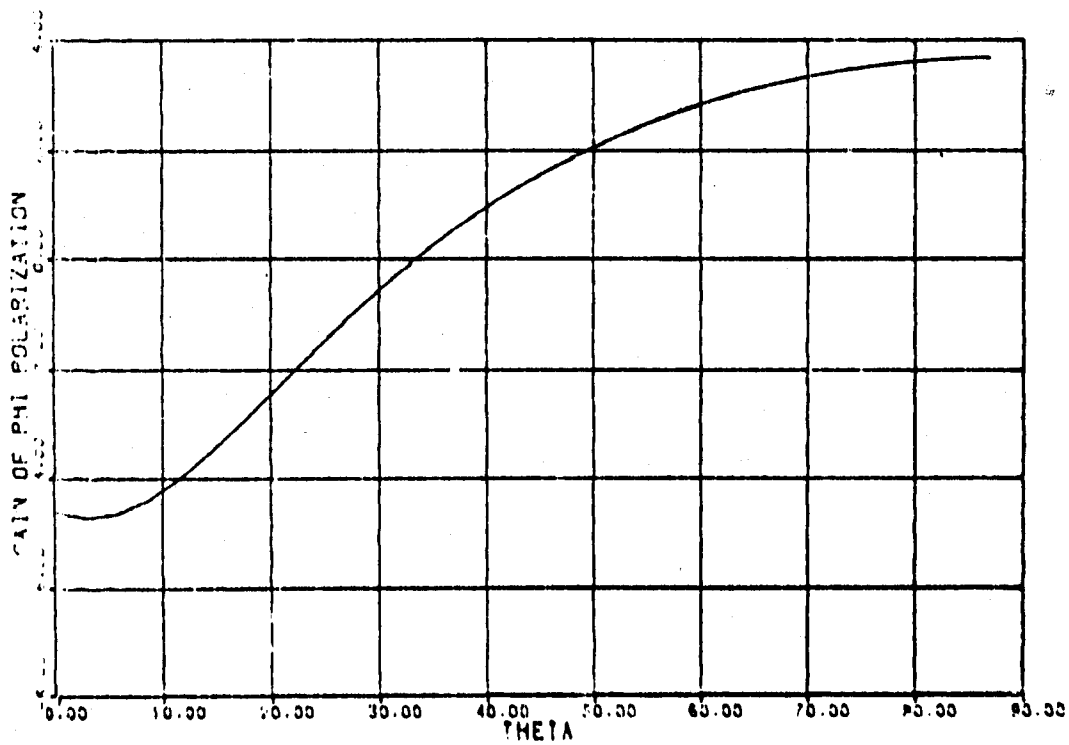


Figure 30.

GRID MODEL. 1.9HZ. DIFF. PATTERN

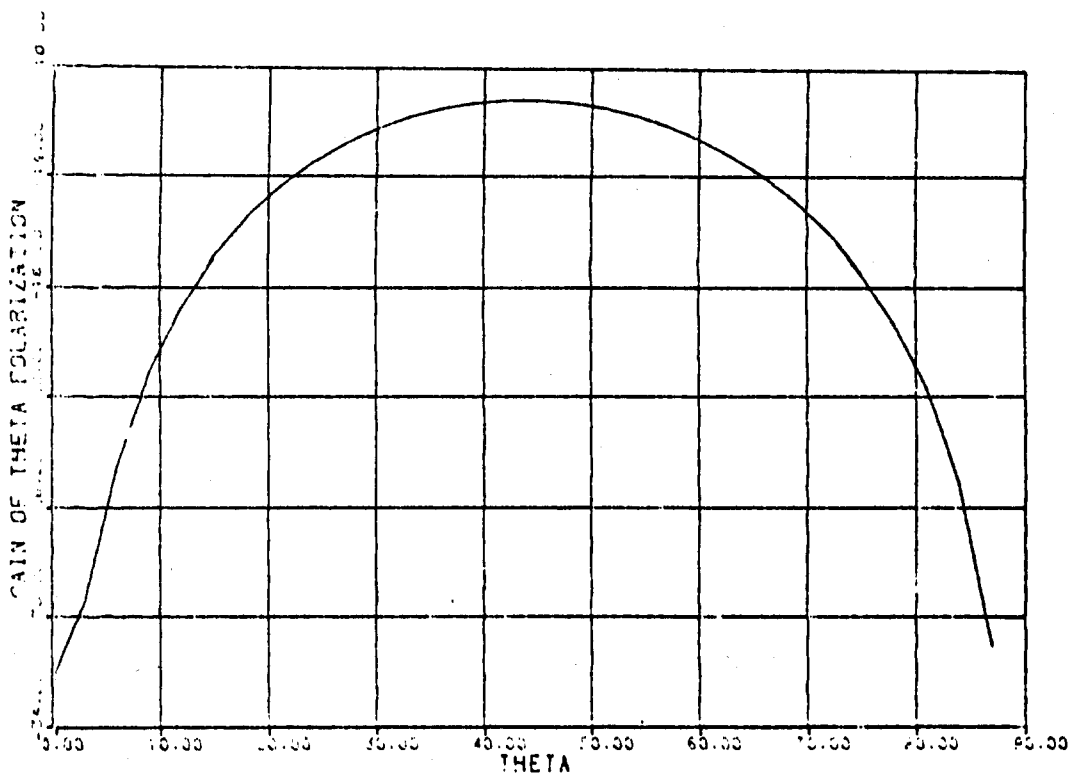


Figure 31.

GRID MODEL. 3.78HZ. SUM PATTERN

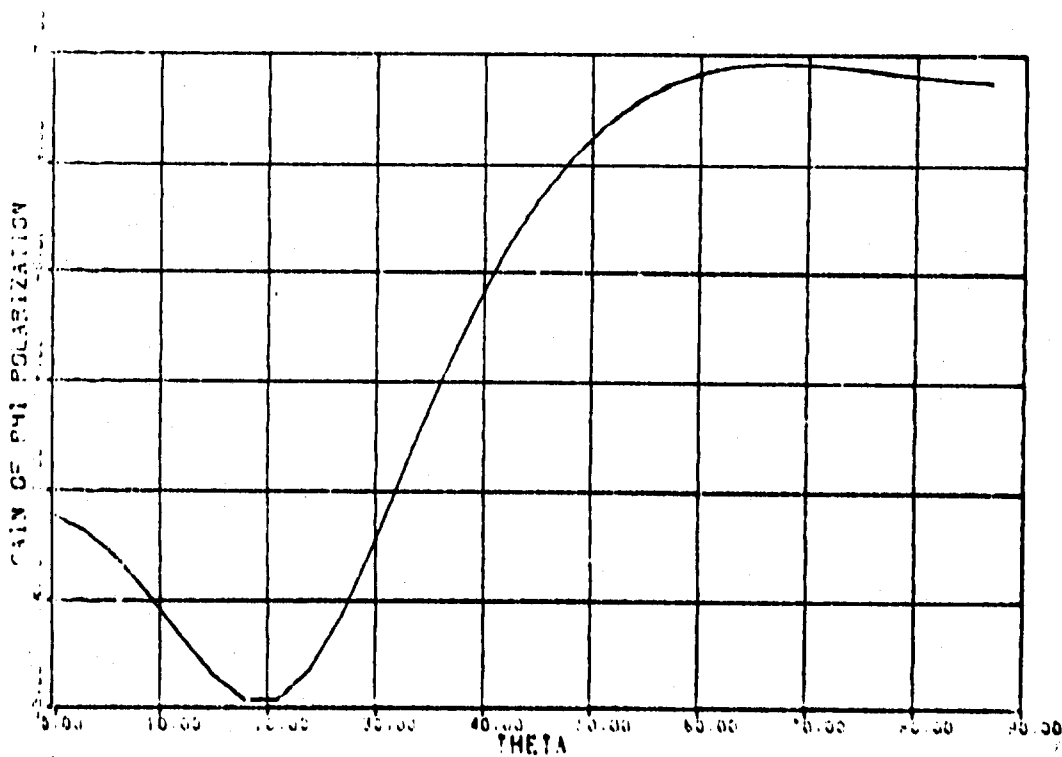


Figure 32.

GRID MODEL, 3.75GHZ, SUM PATTERN

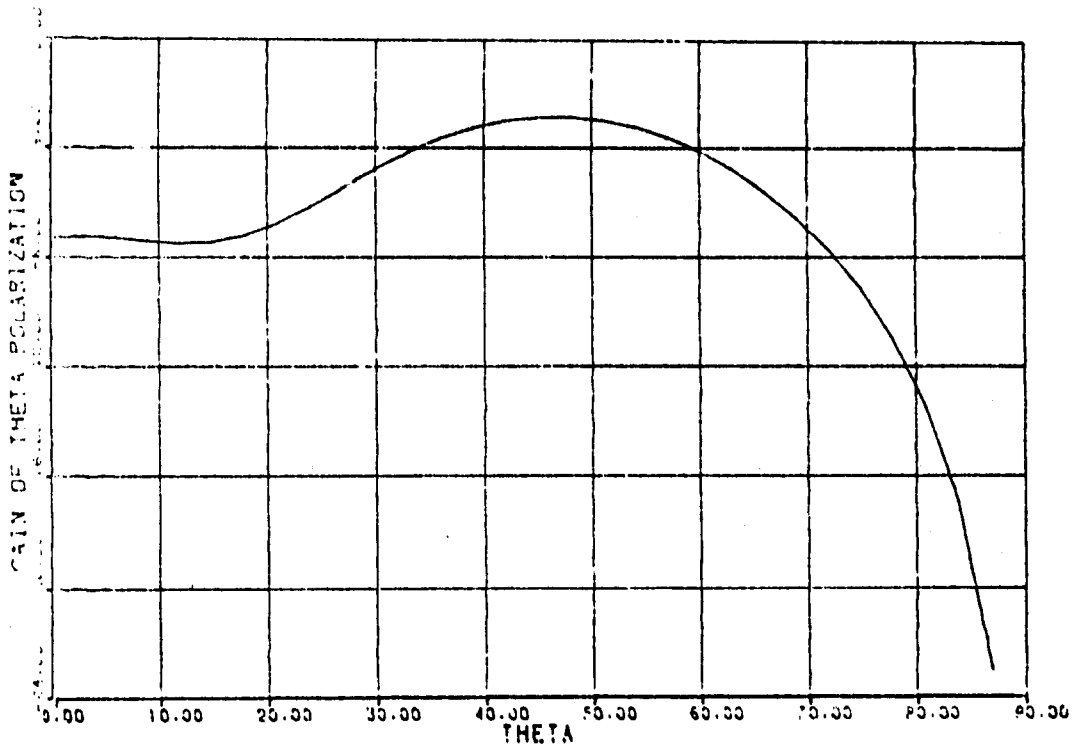


Figure 33.

GRID MODEL, 3.75GHZ, DIFF. PATTERN

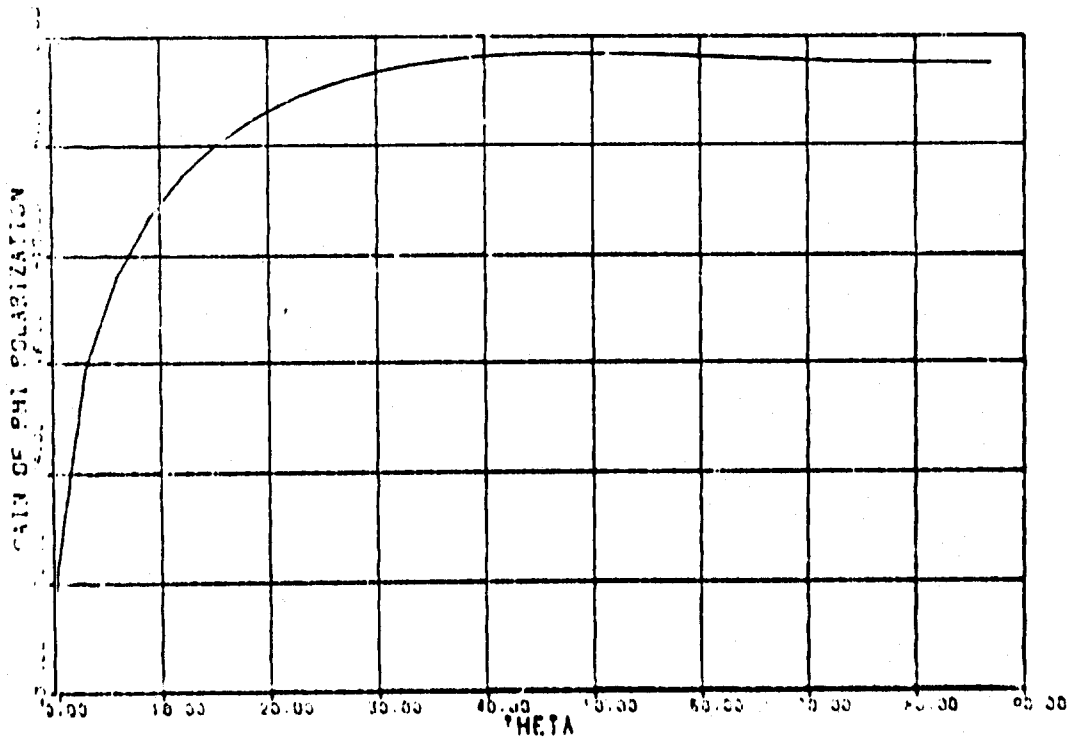


Figure 34.

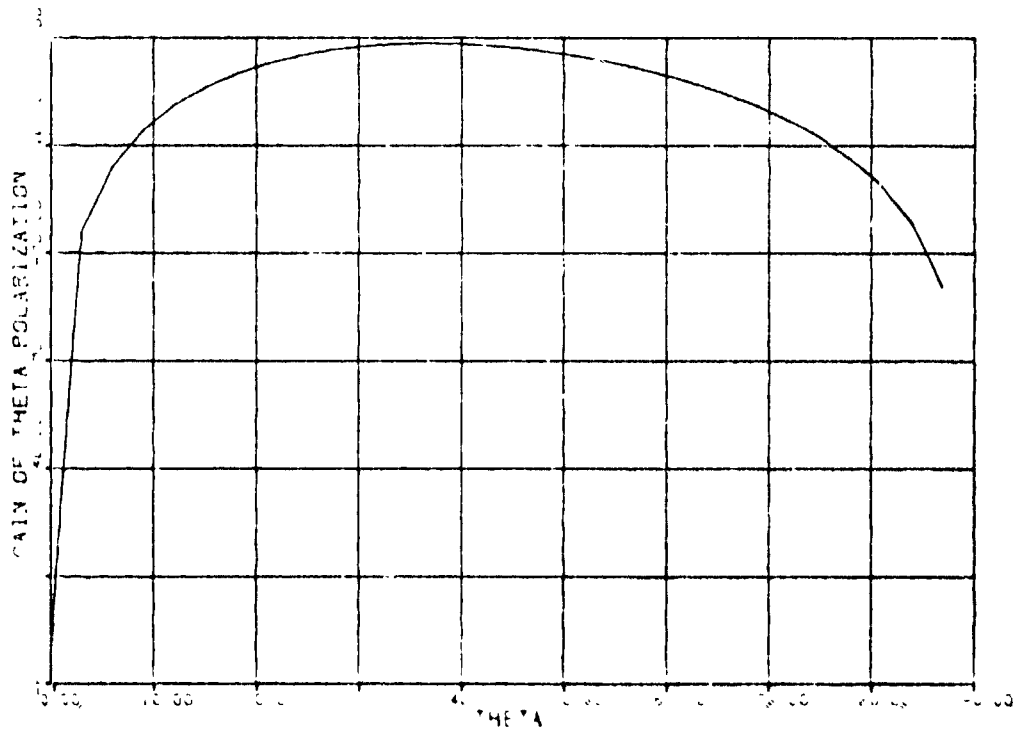


Figure 35.

Another interesting aspect of radiation study, beside the radiation patterns themselves, is to observe the currents developed on the antenna. In this study, the currents have been plotted along one arm of the thin wire model. The actual plots show the expansion mode numbers versus the coefficients of the current expansion. The expansion mode numbers are merely an indexing of the piecewise sinusoidal functions that go from 1 to 99 as the

arm is traversed from the feed to the outer tip. To understand the meaning of the plots, the mode number must be converted into something meaningful. This is done in Table V. This table converts the mode number into the circumference about the antenna in which the particular expansion function is centered.

Table V
Mode Circumference Conversion

| Mode | Number | | Circumference (cm) | | |
|------|--------|----|--------------------|-------|-------|
| 1 | 34 | 67 | 2.50 | 5.83 | 13.53 |
| 2 | 35 | 68 | 2.57 | 5.97 | 13.88 |
| 3 | 36 | 69 | 2.63 | 6.12 | 14.24 |
| 4 | 37 | 70 | 2.70 | 6.28 | 14.61 |
| 5 | 38 | 71 | 2.77 | 6.44 | 14.99 |
| 6 | 39 | 72 | 2.84 | 6.61 | 15.38 |
| 7 | 40 | 73 | 2.92 | 6.78 | 15.78 |
| 8 | 41 | 74 | 2.99 | 6.96 | 16.19 |
| 9 | 42 | 75 | 3.07 | 7.14 | 16.61 |
| 10 | 43 | 76 | 3.15 | 7.32 | 17.04 |
| 11 | 44 | 77 | 3.23 | 7.52 | 17.48 |
| 12 | 45 | 78 | 3.31 | 7.71 | 17.93 |
| 13 | 46 | 79 | 3.40 | 7.91 | 18.40 |
| 14 | 47 | 80 | 3.49 | 8.12 | 18.87 |
| 15 | 48 | 81 | 3.58 | 8.32 | 19.36 |
| 16 | 49 | 82 | 3.67 | 8.54 | 19.86 |
| 17 | 50 | 83 | 3.77 | 8.76 | 20.38 |
| 18 | 51 | 84 | 3.86 | 8.91 | 20.91 |
| 19 | 52 | 85 | 3.96 | 9.22 | 21.48 |
| 20 | 53 | 86 | 4.07 | 9.46 | 22.01 |
| 21 | 54 | 87 | 4.17 | 9.70 | 22.57 |
| 22 | 55 | 88 | 4.28 | 9.95 | 23.16 |
| 23 | 56 | 89 | 4.39 | 10.21 | 23.76 |
| 24 | 57 | 90 | 4.50 | 10.48 | 24.38 |
| 25 | 58 | 91 | 4.62 | 10.75 | 25.01 |
| 26 | 59 | 92 | 4.74 | 11.03 | 25.65 |
| 27 | 60 | 93 | 4.86 | 11.31 | 26.32 |
| 28 | 61 | 94 | 4.99 | 11.61 | 27.00 |
| 29 | 62 | 95 | 5.12 | 11.91 | 27.70 |
| 30 | 63 | 96 | 5.25 | 12.22 | 28.42 |
| 31 | 64 | 97 | 5.39 | 12.53 | 29.16 |
| 32 | 65 | 98 | 5.53 | 12.86 | 29.91 |
| 33 | 66 | 99 | 5.67 | 13.19 | 30.69 |

Figures 36 through 40 show the amplitude of the current coefficients (normalized to one) at various frequencies for sum pattern generation. These currents are taken from the four arm thin wire model.

SUM MODE AT 500 MHZ

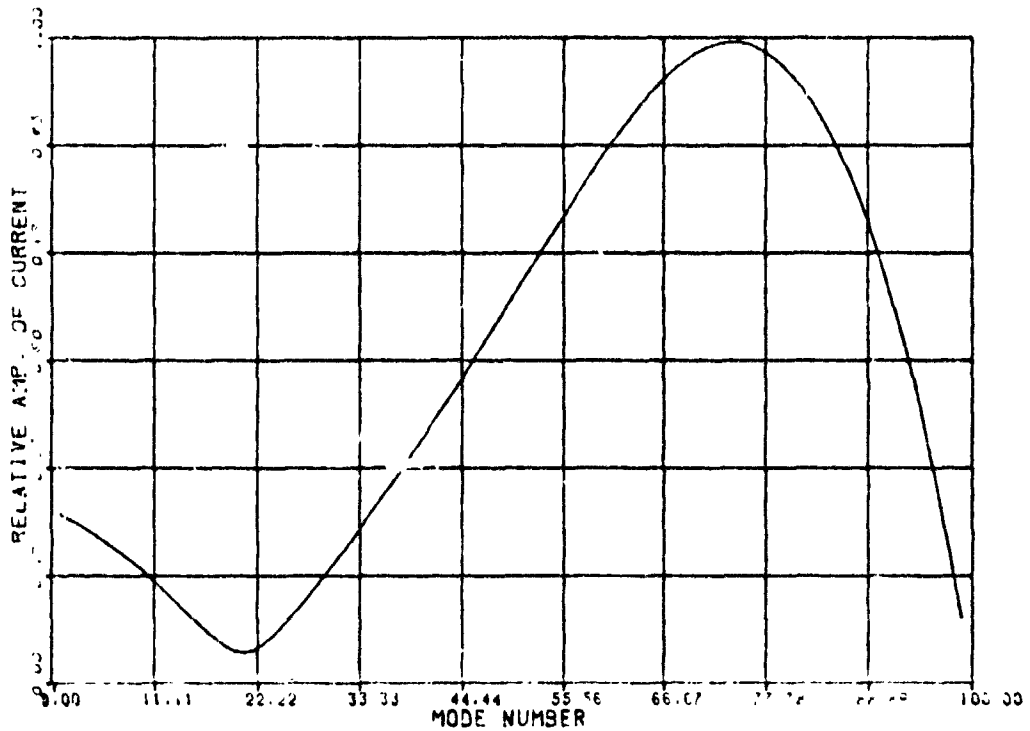


Figure 36.

SUM MODE AT 1 GHZ

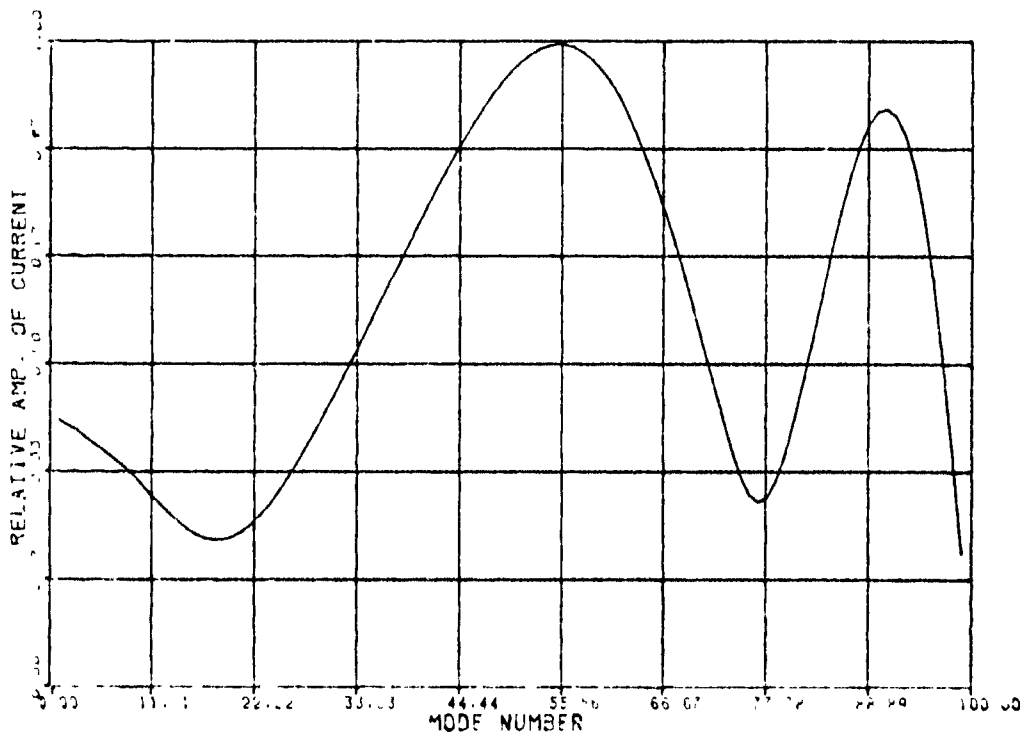


Figure 37.

SUM MODE AT 2 GHZ

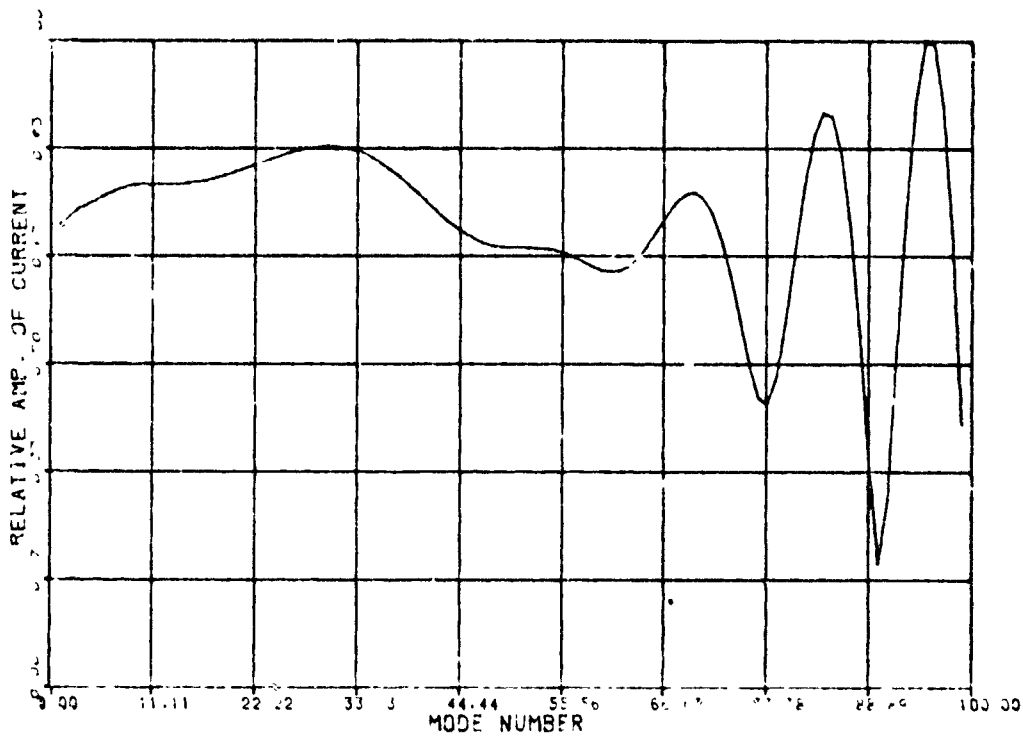


Figure 38.

SUM MODE AT 3.75 GHZ

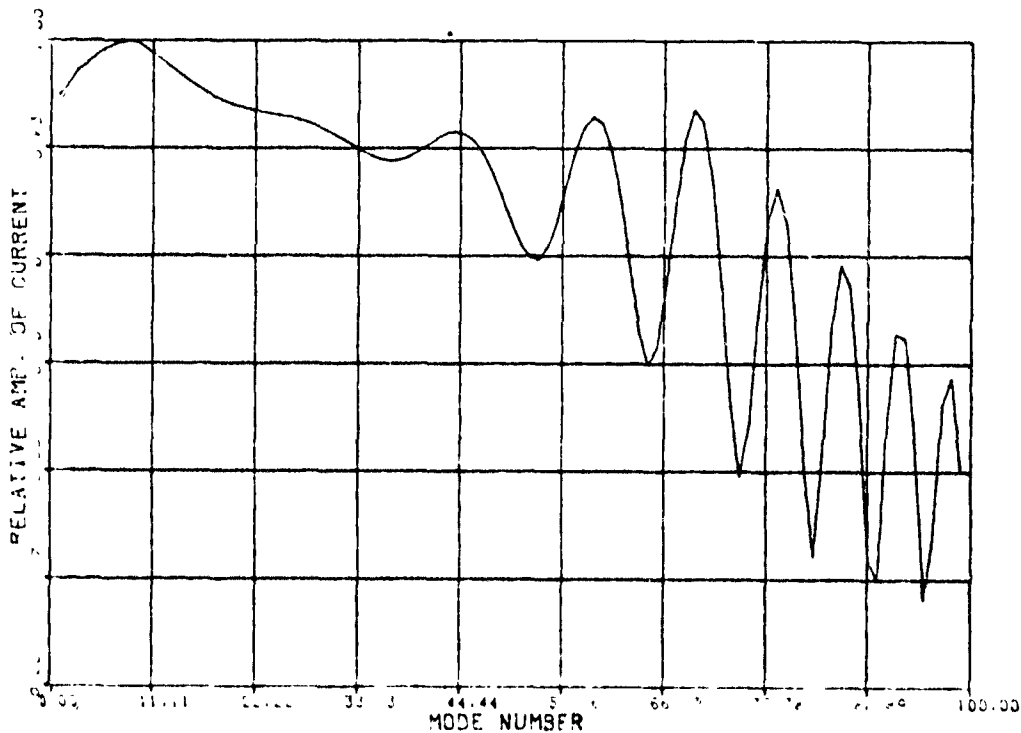


Figure 39.

SUM MODE AT 5 GHZ

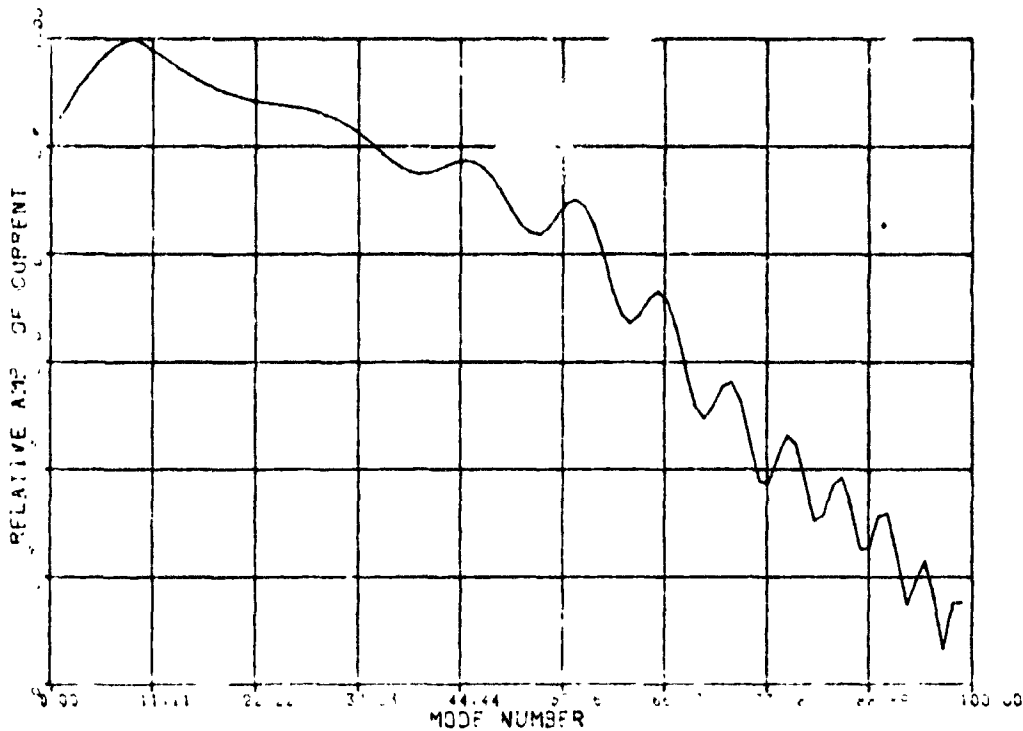


Figure 40.

As Mosko [9] indicated, there should be current resonance where the circumference of the antenna is one wavelength for sum patterns. Figure 38, the 2 GHz case, shows resonance around circumferences of 15 cm, 21 cm, and 29 cm. The wavelength in this case is 15 cm. There are two extra resonance areas on the spiral. Extra resonance peaks also occur in currents forming difference patterns. These currents, from the thin wire model, are plotted in Figures 41 through 45.

DIFF. MODE AT 300 MHZ

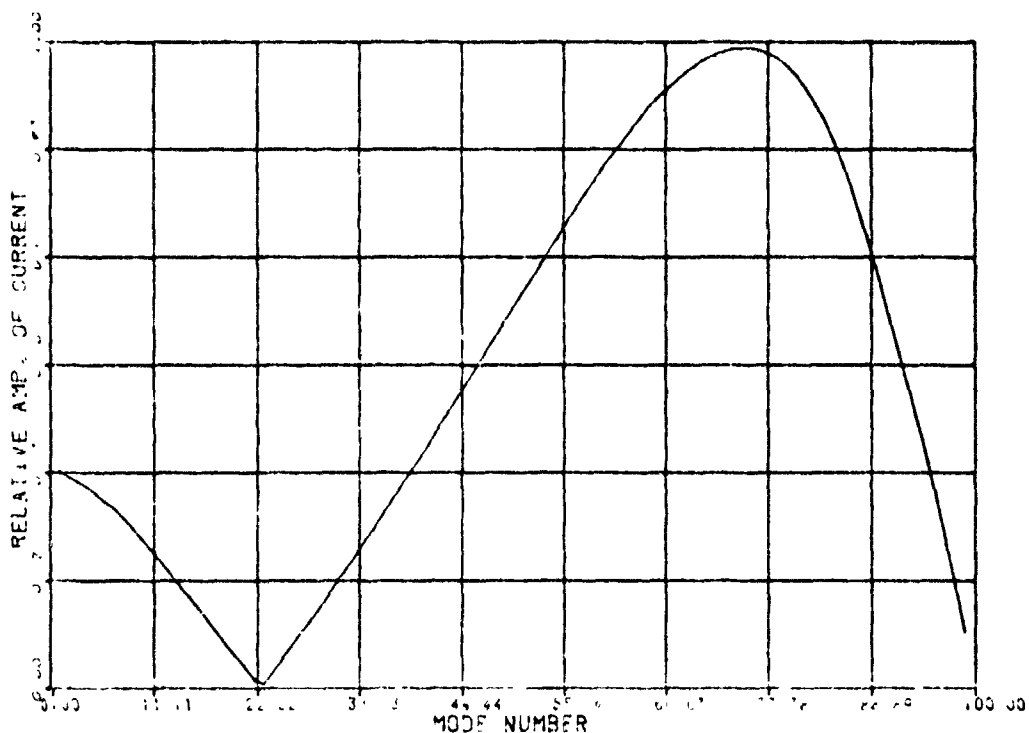


Figure 41.

DIFF. MODE AT 1 GHZ

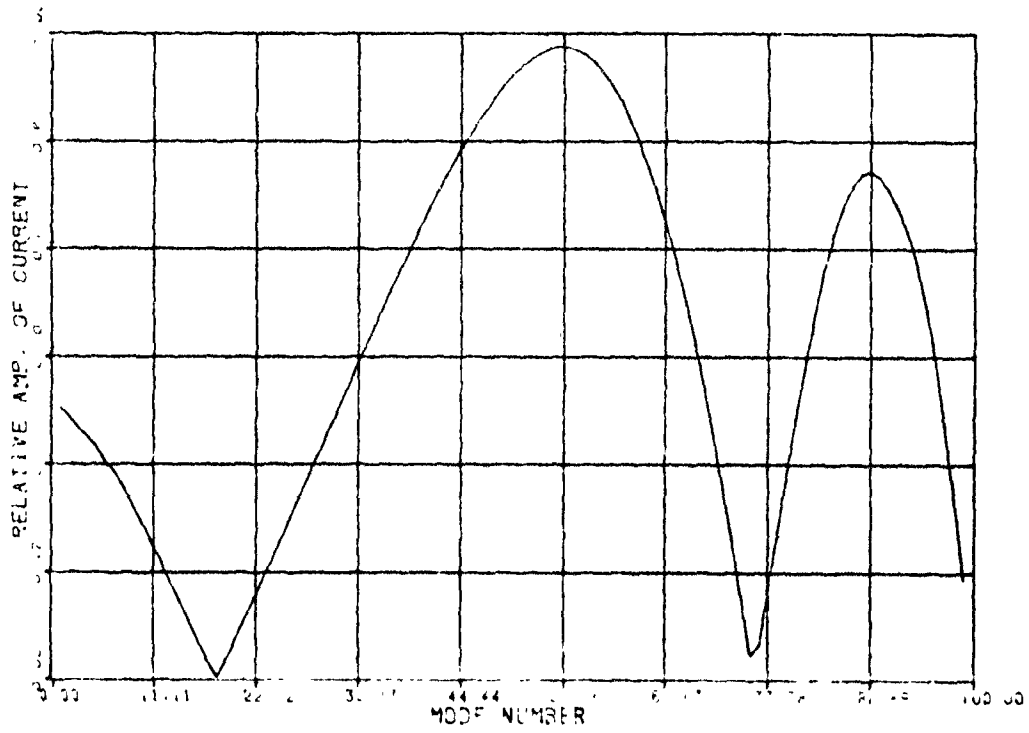


Figure 42.

DIFF. MODE AT 2 GHZ

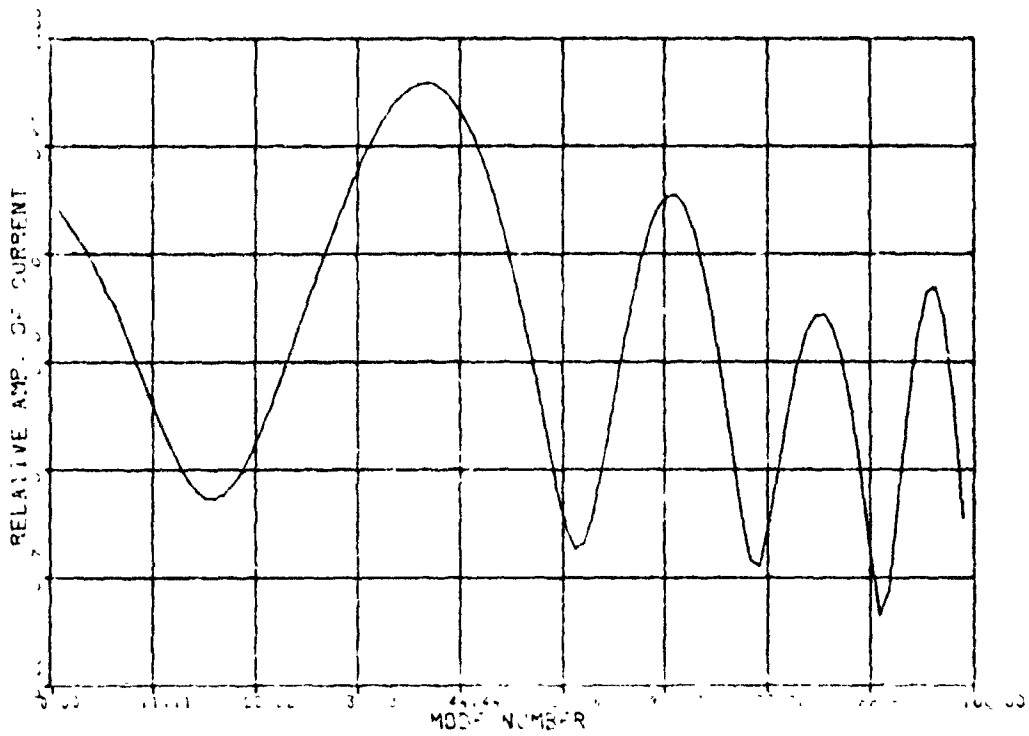


Figure 43.

DIFF. MODE AT 3.75 GHZ

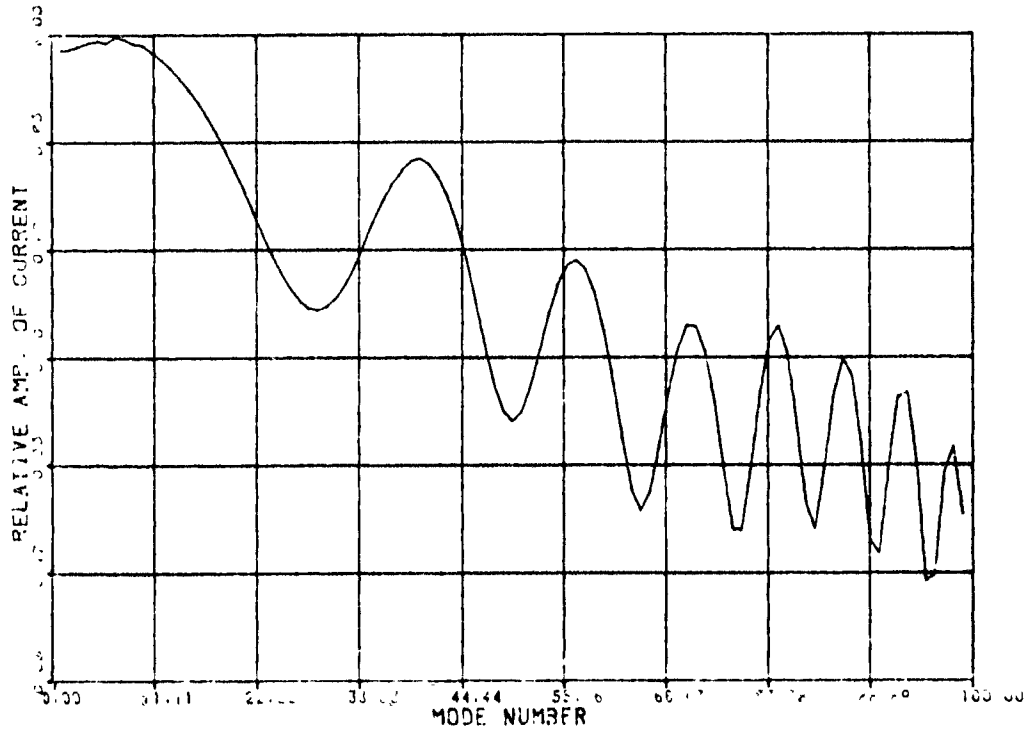


Figure 44.

DIFF. MODE AT 5 GHZ

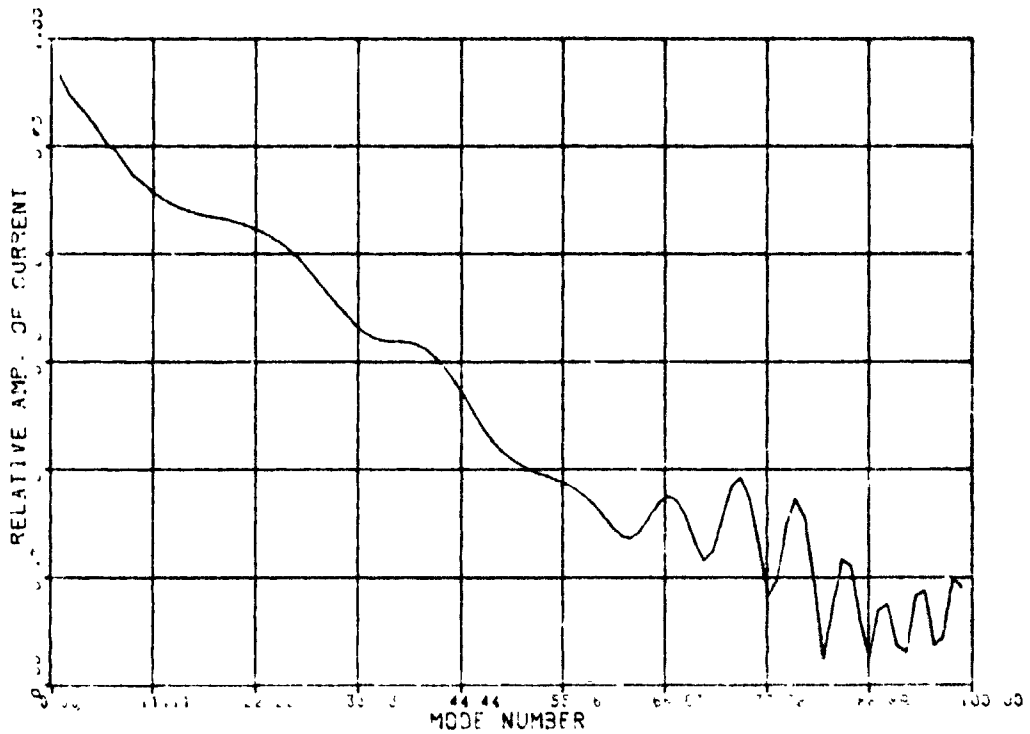


Figure 45.

Mosko [9] explained there should be current resonance where the circumference equals two wavelengths in the difference pattern generation. This has also been supported from near field measurements done by John Dyson at the University of Illinois. However, Figure 43, the case of 2 GHz, shows resonances at circumferences of 7 cm, 14 cm, 20 cm, and 28 cm. The only resonance should occur at a circumference of 30 cm. This is probably where the last resonance peak "wants" to be, but it must shift to allow the current to die on the tip of the arm.

Figures 46 through 54 show the phases of current coefficients producing sum and difference patterns at various frequencies. They show that the phase of the current changes rapidly in low amplitude areas. Again, these plots are taken from the currents formed in the four arm thin wire model.

SUM MODE AT 500 MHZ

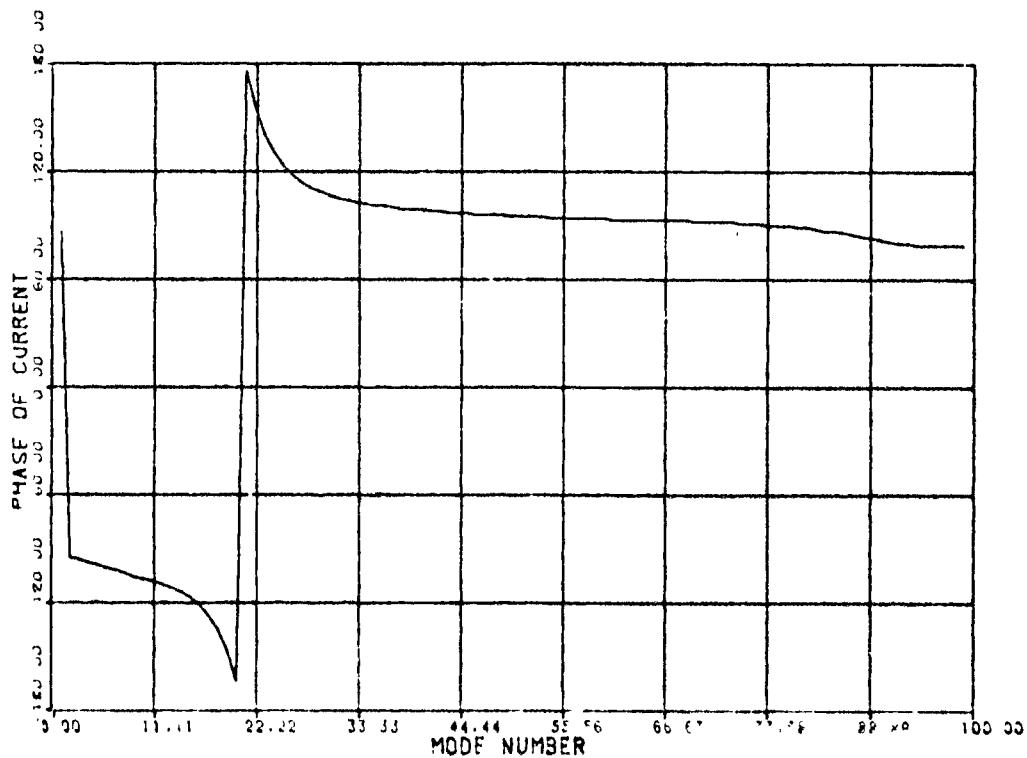


Figure 46.

SUM MODE AT 1 GHZ

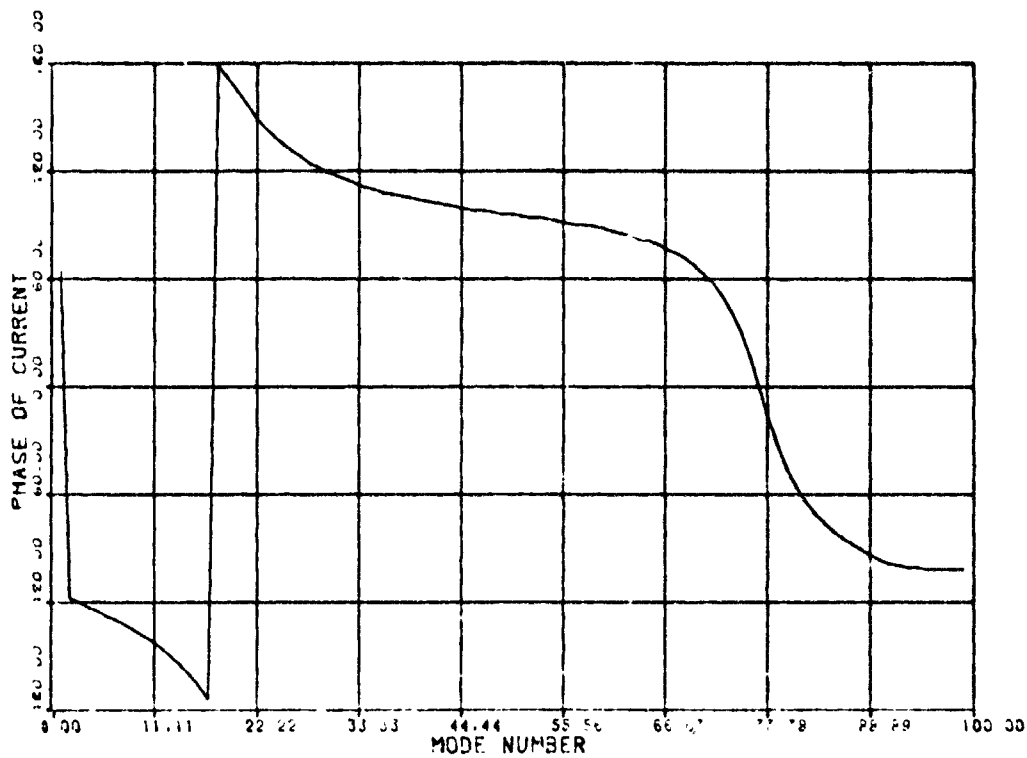


Figure 47.

SUM MODE AT 2 GHZ

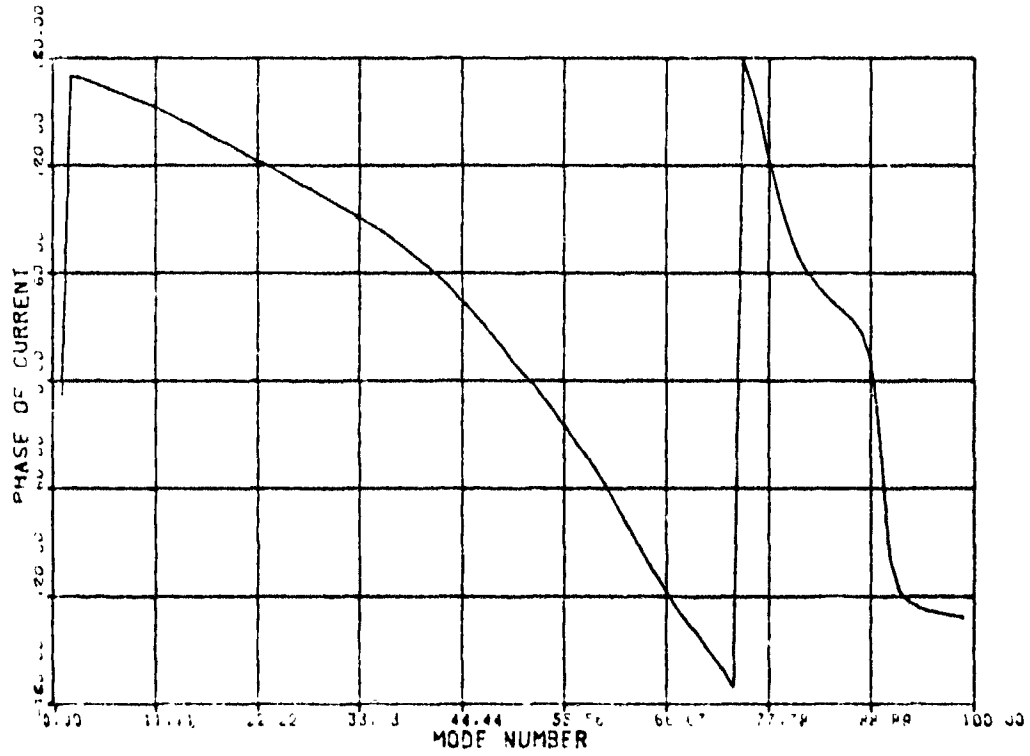


Figure 48.

SUM MODE AT 3.75 GHZ

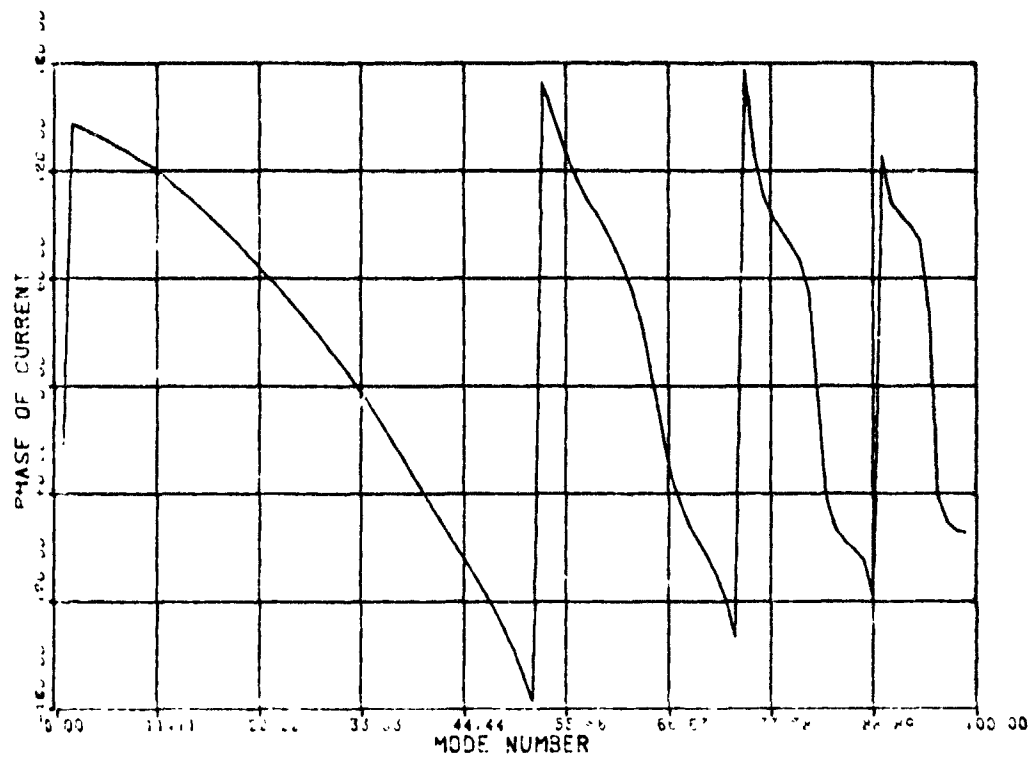


Figure 49.

COM MODE AT 5 GHZ

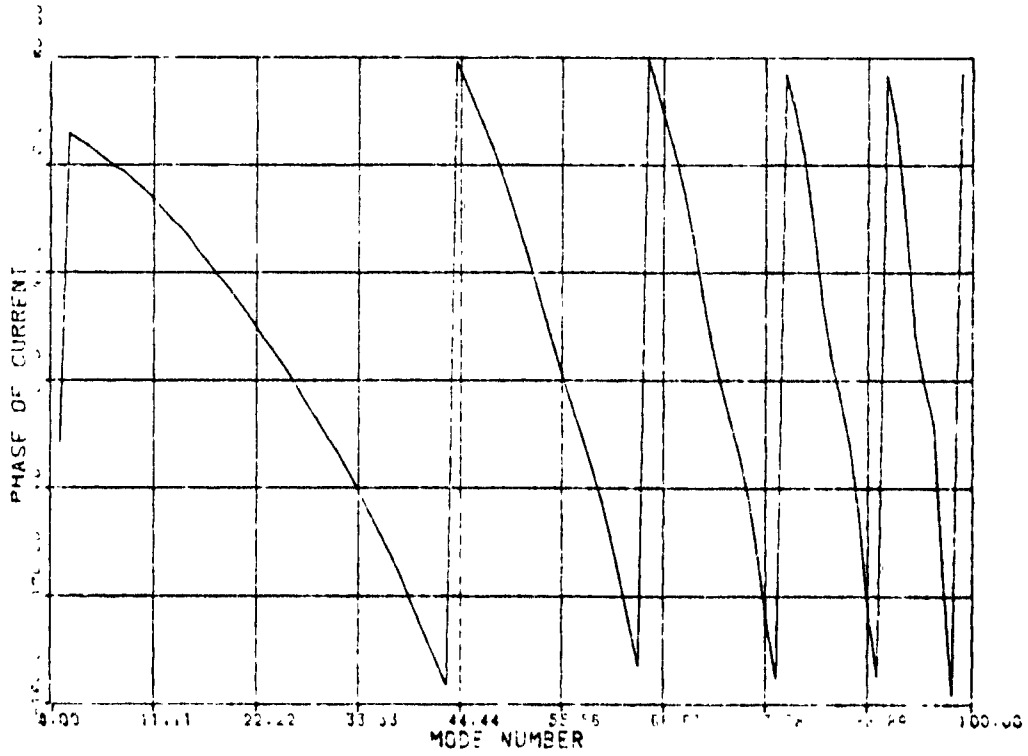


Figure 50.

DIFF. MODE AT 1 GHZ

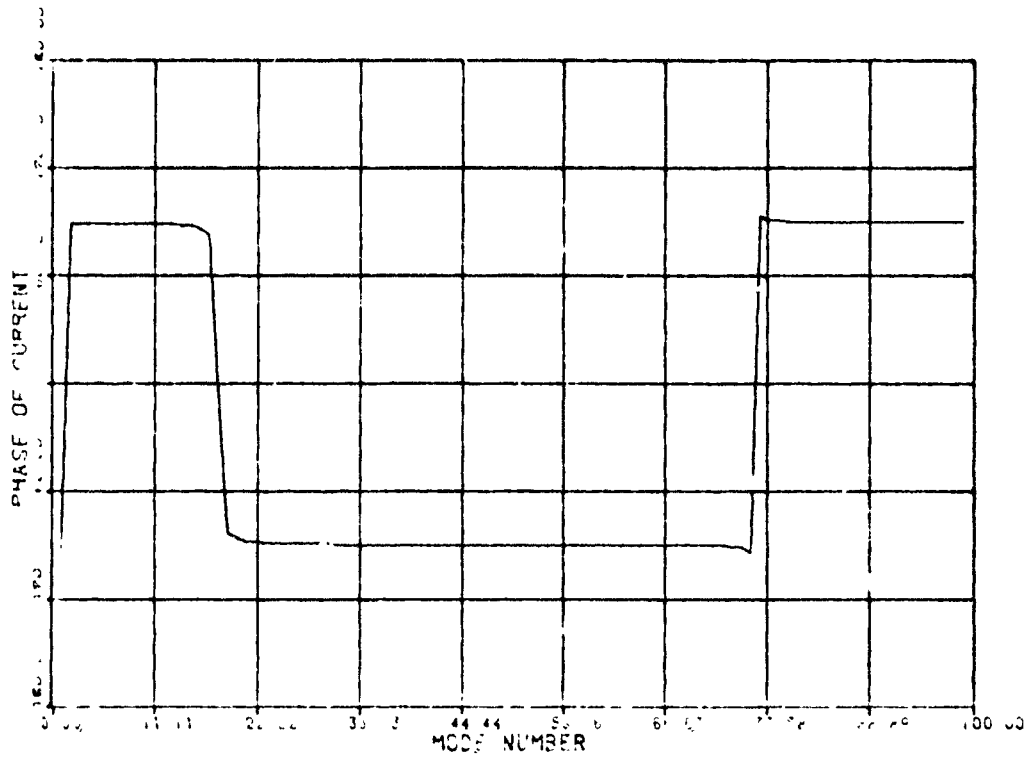


Figure 51.

DIFF. MODE AT 2 GHz

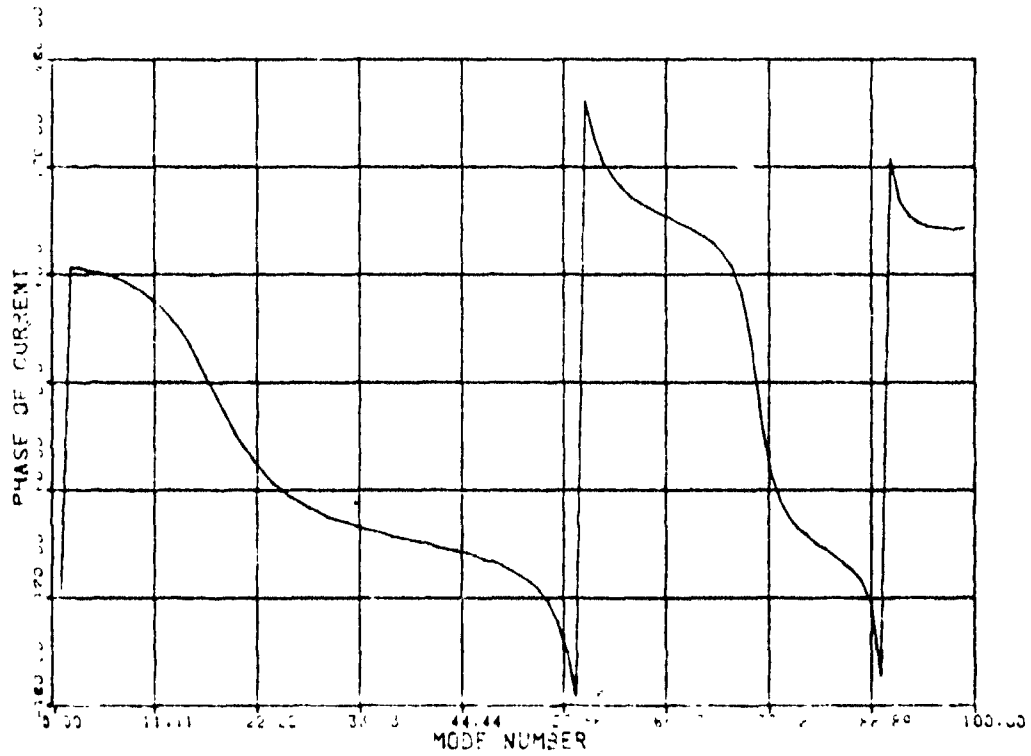


Figure 52.

DIFF. MODE AT 3.1 GHz

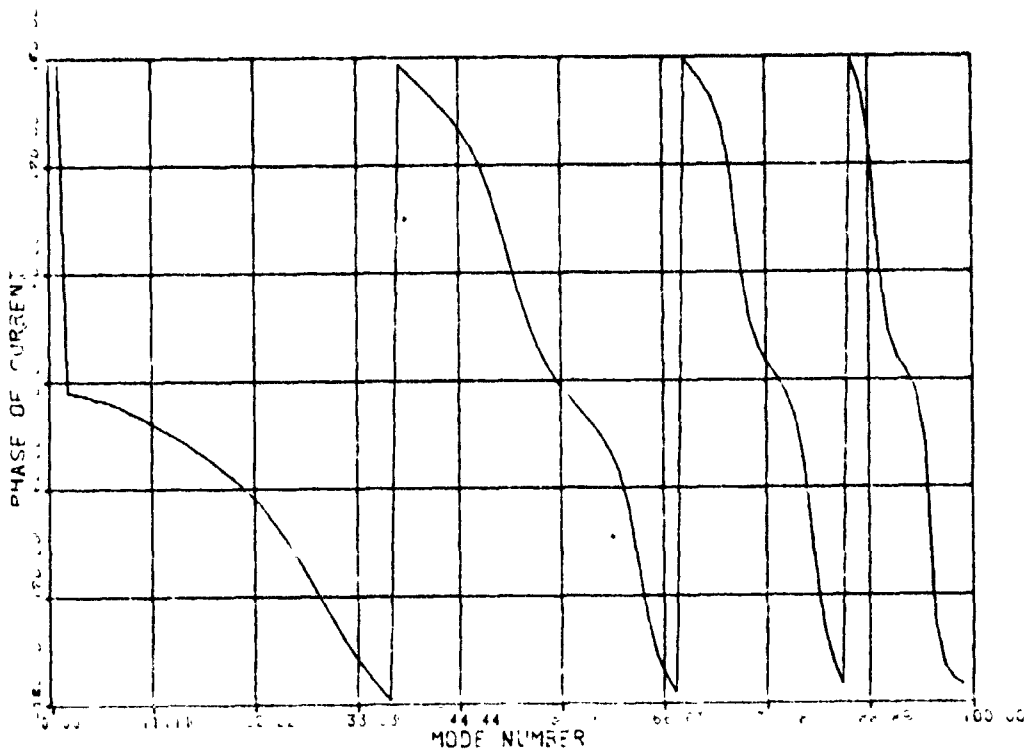


Figure 53.

DIFF. MODE AT 8 GHZ

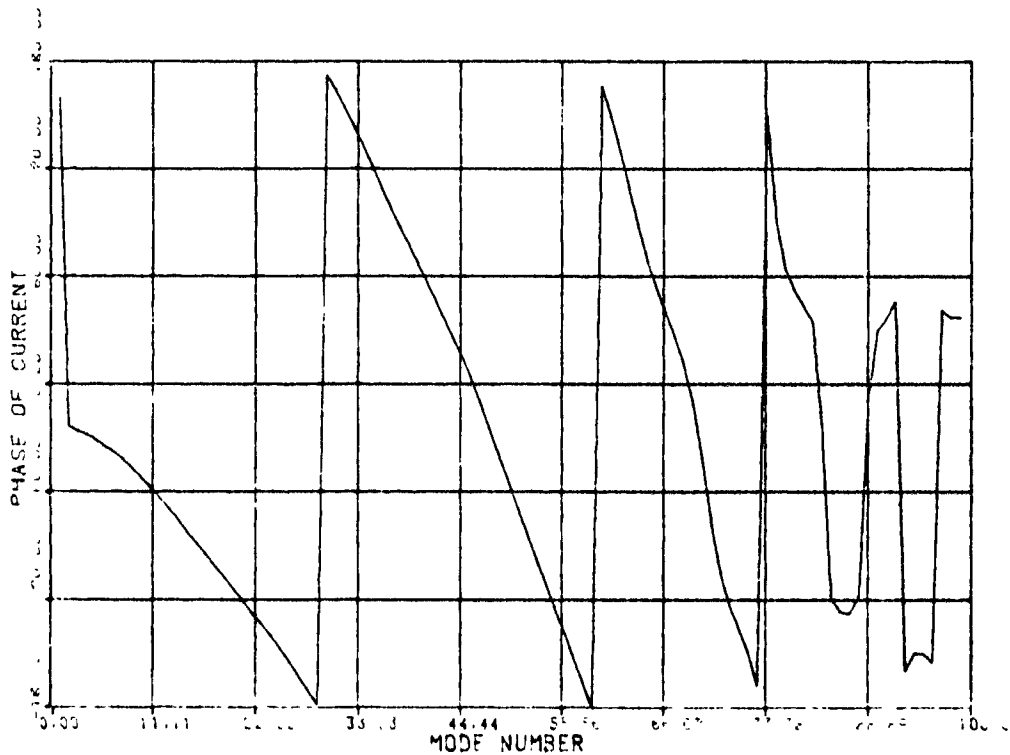


Figure 54.

The currents on the arms of the wire grid model cannot be plotted as easily as those in the thin wire model because many expansion functions overlap transverse and longitudinal segments of wire. However, it was noted in this model that the expansion functions that contained cross hatches had very insignificant coefficients, except near the center of the antenna. This would help explain why the wire grid difference patterns differed more with the thin wire results

than the sum patterns. This is because, in general, the bulk of the difference pattern current is closer to the center of the antenna than the bulk of the sum pattern current.

The extra resonance areas in the current distributions may best be explained by an inadequacy in the modelling. The open circuited tips on the ends of the arms cause a reflection of the outward travelling current. What results is a standing wave pattern. To correct this situation, it has been suggested that a resistive-inductive load be placed on the tips of the arms to absorb the outward travelling energy [16]. To do this, a $50 + j50$ ohm load was placed in the thin wire model on the point connecting the outer two segments of each arm. The resulting current distributions for the sum and difference pattern generation at 2 GHz are given in Figures 55 and 56.

LOADED THIN WIRE, 2GHZ, COM PATTERN

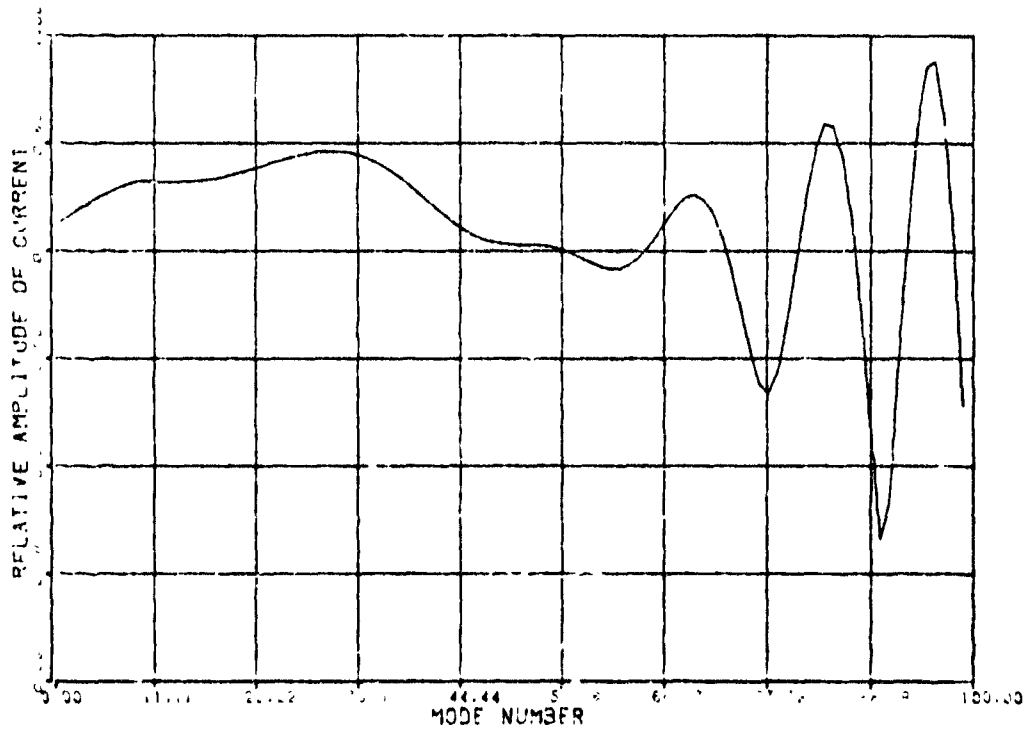


Figure 55.

LOADED THIN WIRE, 2GHZ, DIFF. PATT.

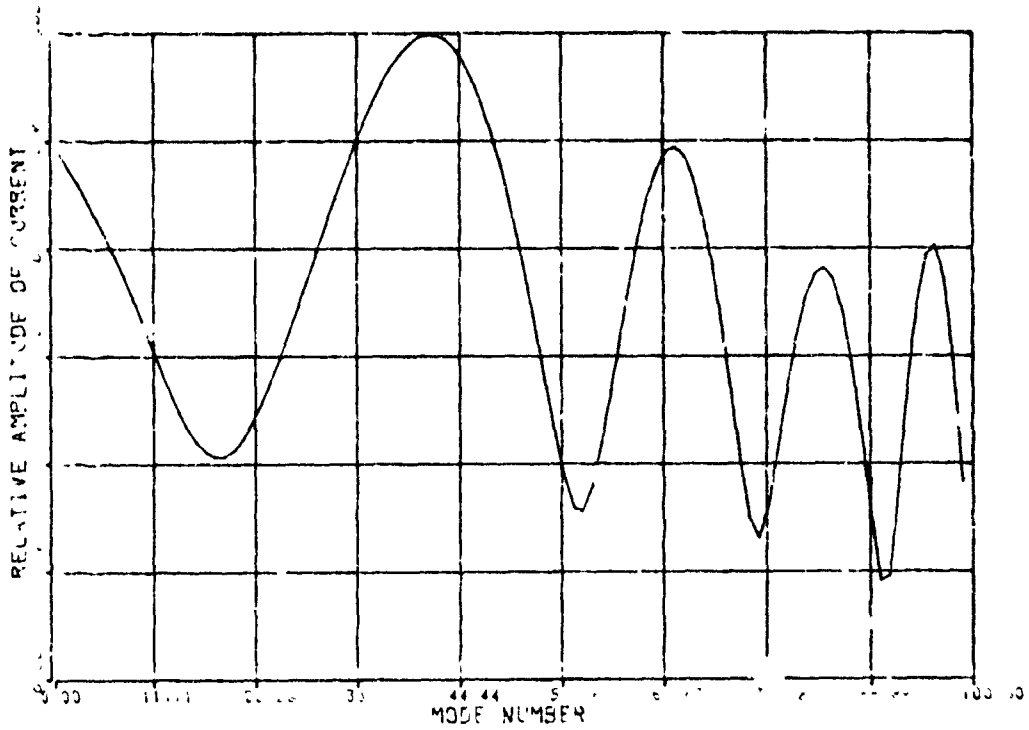


Figure 56.

There is very little change in the current distributions for the loaded and unloaded thin wire models. Perhaps a much larger impedance would show more improvement. There is also very little change in the loaded radiation patterns from the patterns shown previously. Figures 57 through 60 give these patterns in the X-Z plane at 2 GHz.

LOADED THIN WIRE, 2GHZ, JM PATTERN

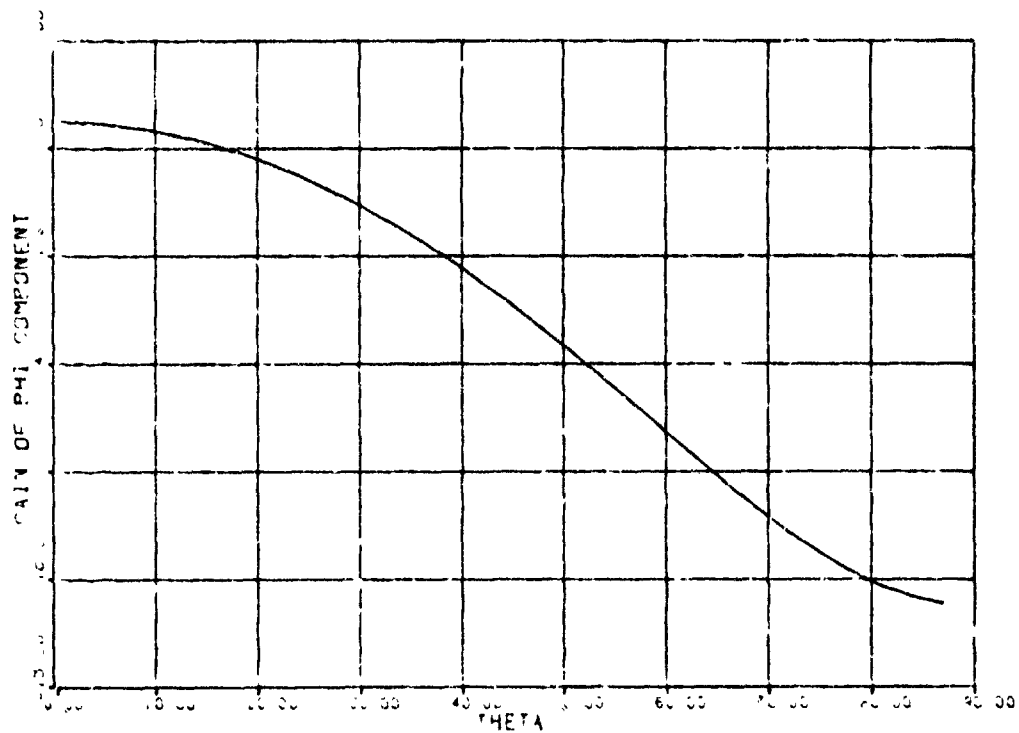


Figure 57.

LOADED THIN WIRE, 2GHZ, SUM PATTERN

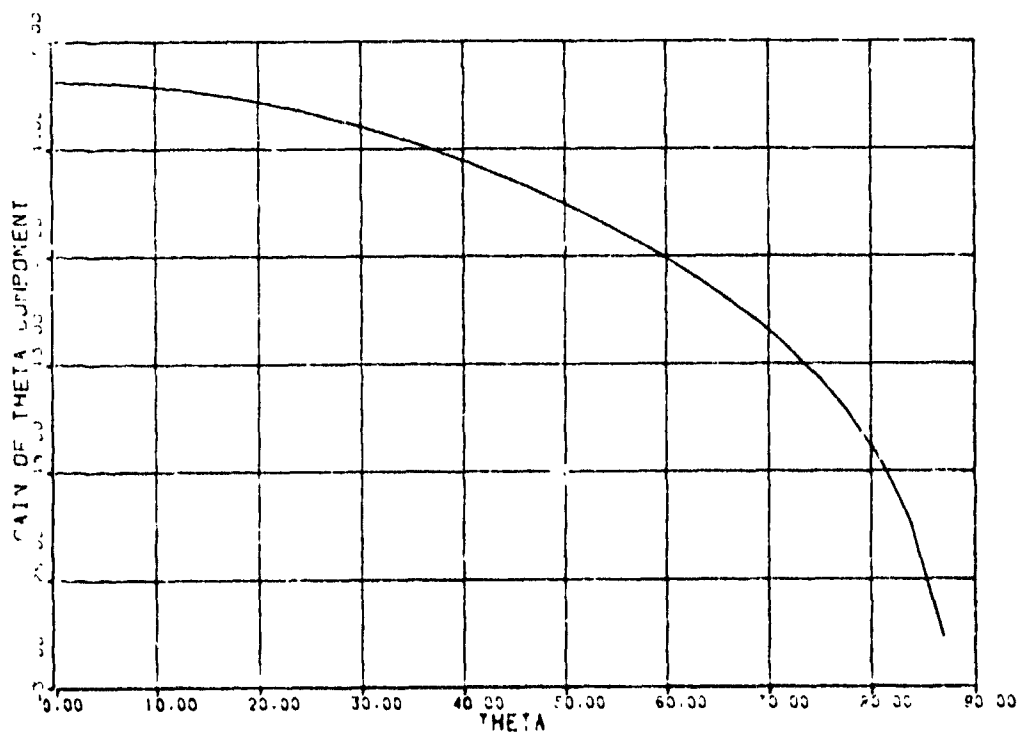


Figure 58.

LOADED THIN WIRE, 2GHZ, DIFF. PATT.

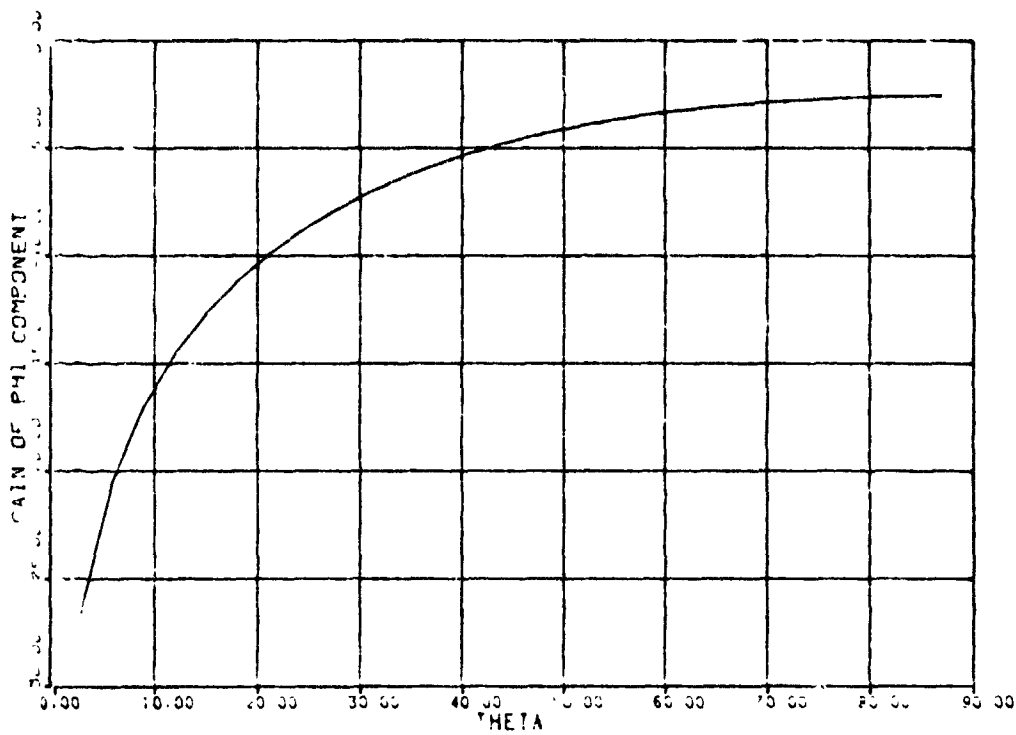


Figure 59.

LOADED THIN WIRE, 2GHZ, DIFF. PATT.

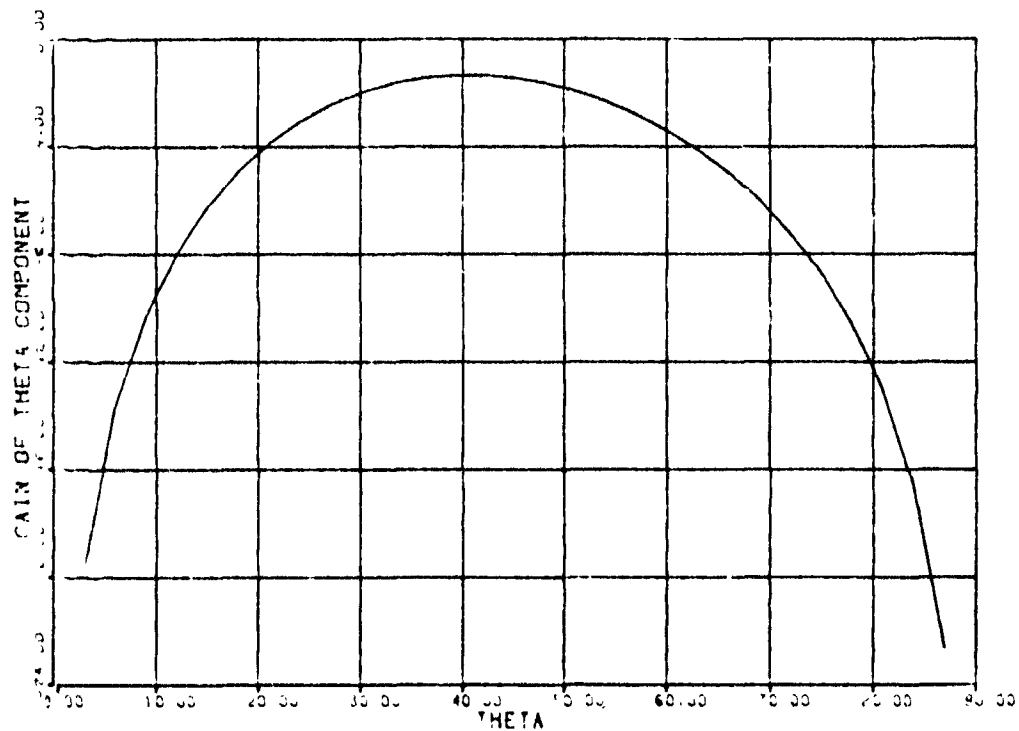


Figure 60.

Results for radar cross section are not given in this report.

Chapter 5

Conclusions and Recommendations

The ESP code produced radiation patterns very close to what was expected, even though the models produced a standing wave current distribution on the antenna arms. This standing wave pattern results from the models' inadequacy in absorbing the outward travelling current on the tips of the arms.

Since there are so few differences in the results with the thin wire grid modelling, it is only necessary to use thin wire modelling to explore radiation patterns or currents of interest. However, it is still necessary to use patch modelling, which is not feasible on a VAX 11/750 computer, to explore the structural mode characteristics of radar cross section.

Further work may be done to experiment with various loads on the ends of the arms to attempt to isolate a single area of current amplitude resonance in a radiating arm. This load should be the complex conjugate of the impedance seen by the outward travelling current at the tip of each arm. This load will change with frequency, as the impedance seen at the tip changes with frequency. The load will also affect the bandwidth. In particular, it may raise the lower frequency cutoff.

If a single load cannot eliminate the current reflection, which will certainly occur when a large

frequency range is tested, another solution may be to attempt a series of loads near the ends of each arm. This may further restrict the antenna operating bandwidth.

Regardless of how the loading is attempted, the elimination of current reflection would probably produce more accurate radiation patterns. This is because actual spiral antennas usually radiate far enough from the outer circumference so that the tip reflection is negligible. The patterns from a correctly loaded model may better demonstrate over what angular sector the frequency independence holds. Also, the radar cross section may be checked to see if loading on the arm tips validate the theory given in Chapter 1.

Appendix A

Thin Wire Model Input

The input defining the thin wire model geometry for the ESP code can be given by a subroutine. The ESP code gives the option of reading the rectangular coordinates of the wire segment endpoints, or generating them through a subroutine called WGEOM. The option to use subroutine WGEOM is determined by a variable known as IRGM in the first read statement of the main program. If this variable is zero, the program uses WGEOM to define the wire geometry [13:32].

The goal of subroutine WGEOM is to define the following variables.

IA(I) = an array (dimensioned by the total number of segments) which defines endpoint A of the Ith segment with a point number

IB(I) = an array (dimensioned by the total number of segments) which defines endpoint B of the Ith segment with a point number

X,Y,Z = arrays (dimensioned by the total number of points) which define the rectangular coordinates of the point location in meters

NM = total number of segments

NP = total number of points

NAT = total number of wire to plate attachments

NWG = number of wire geometries - this variable is passed from the main program to subroutine WGEOM

VG(I) = complex voltage at the A endpoint of the Ith segment

ZLD(I) = complex impedance at the A endpoint of the Ith segment

WV = wavelength - this variable is passed from the main program to subroutine WGEOM

In addition, the array variables NSA, NPLA, VGA, BDSK, and ZLDA exist for a general subroutine WGEOM, but need not be defined unless wire to plate attachments are involved in the geometry. Also, the variables NFS1 and NFS2 exist and need to be defined as zero when mutual coupling between feed points is neglected, as in this study.

The subroutine used to define this input information for the four arm thin wire model is listed as follows.

```
      SUBROUTINE WGEOM(IA,IB,X,Y,Z,NM,NP,NAT,NSA,NPLA,VGA,
*      BDSK,ZLDA,NWG,VG,ZLD,WV,NFS1,NFS2)
      DIMENSION IA(1),IB(1),X(1),Y(1),Z(1),NSA(1),NPLA(1),
*      BDSK(1)
      COMPLEX VGA(1),ZLDA(1),VG(1),ZLD(1)
      NM = 404
      NP = 405
C      DEFINE POINTS FOR ARM #1
      DO 83 I=1,100
      Z(I) = 0.0
      FF = REAL(I)
      PHEE = (FF-1.0)*10.
      PHEEP = PHEE*3.14159265/180.
      PH900 = PHEE/900.
      R = 0.398*(10.**PH900)*0.01
      X(I) = R*COS(PHEEP)
      83 Y(I) = R*SIN(PHEEP)
C      DEFINE ENDPOINTS FOR SEGMENTS FOR ARM#1
      DO 84 I=1,99
      IA(I) = I
      84 IB(I) = I+1
C      DEFINE POINTS FOR ARM#2
      DO 85 I=101,200
      Z(I) = 0.0
      FF = REAL(I)
      PHEE = (FF-101.)*10.
      PHEEP = (PHEE+90.)*3.14159265/180.
      PH900 = PHEE/900.
      R = 0.398*(10.**PH900)*0.01
      X(I) = R*COS(PHEEP)
      85 Y(I) = R*SIN(PHEEP)
C      DEFINE ENDPOINTS FOR SEGMENTS FOR ARM#2
      DO 86 I=100,198
      IA(I) = I+1
```

```

86 IB(I) = I+2
C   DEFINE POINTS FOR ARM#3
   DO 87 I=201,300
     Z(I) = 0.0
     FF = REAL(I)
     PHEE = (FF-201.)*10.
     PHEEP = (PHEE+180.)*3.14159265/180.
     PH900=PHEE/900.
     R = 0.398*(10.**PH900)*0.01
     X(I) = R*COS(PHEEP)
87 Y(I) = R*SIN(PHEEP)
C   DEFINE ENDPOINTS FOR SEGMENTS FOR ARM#3
   DO 88 I=199,297
     IA(I) = I+2
88 IB(I) = I+3
C   DEFINE POINTS FOR ARM#4
   DO 89 I=301,400
     Z(I) = 0.0
     FF = REAL(I)
     PHEE = (FF-301.)*10.
     PHEEP = (PHEE+270.)*3.14159265/180.
     PH900 = PHEE/900.
     R = 0.398*(10.**PH900)*0.01
     X(I) = R*COS(PHEEP)
89 Y(I) = R*SIN(PHEEP)
C   DEFINE ENDPOINTS FOR SEGMENTS FOR ARM#4
   DO 90 I=298,396
     IA(I) = I+3
90 IB(I) = I+4
C   INDICATE NO ATTACHMENTS OR COUPLING
   NAT = 0
   NFS1 = 0
   NFS2 = 0

C
C   DEFINE FEED STRUCTURE FOR SUM PATTERN
C
X(401) = 0.
Y(401) = 0.
Z(401) = 0.
X(402) = 0.00199
Y(402) = 0.
Z(402) = 0.
X(403) = 0.
Y(403) = 0.00199
Z(403) = 0.
X(404) = -0.00199
Y(404) = 0.
Z(404) = 0.
X(405) = 0.
Y(405) = -0.00199
Z(405) = 0.
IA(397) = 1
IE(397) = 402

```

```

IA(398) = 402
IB(398) = 401
IA(399) = 101
IB(399) = 403
IA(400) = 403
IB(400) = 401
IA(401) = 201
IB(401) = 404
IA(402) = 404
IB(402) = 401
IA(403) = 301
IB(403) = 405
IA(404) = 405
IB(404) = 401
VG(398) = (1.0,0.0)
VG(400) = (0.0,1.0)
VG(402) = (-1.0,0.0)
VG(404) = (0.0,-1.0)
RETURN
END

```

When difference pattern feeding is desired, the last six lines of the subroutine can be substituted with the following.

```

VG(398) = (1.0,0.0)
VG(400) = (-1.0,0.0)
VG(402) = (1.0,0.0)
VG(404) = (-1.0,0.0)
RETURN
END

```

When a complex impedance of $50+j50$ ohms is placed between the last two segments of each arm, the following statements must be added before the RETURN statement.

```

ZLD(99) = (50.0,50.0)
ZLD(198) = (50.0,50.0)
ZLD(297) = (50.0,50.0)
ZLD(396) = (50.0,50.0)

```

Appendix B

Wire Grid Model Input

A subroutine WGEOM is written to provide the input data for the geometry of the wire grid model. An explanation of the purpous and a general description of a subroutine WGEOM is given in Appendix A and need not be repeated here. The following is a listing of the WGEOM fortran subroutine for the wire grid model, with comments to aid in understanding the accomplishments of each section of code.

```

SUBROUTINE WGEOM(IA,IB,X,Y,Z,NM,NP,NAT,NSA,NPLA,VGA,
*BDISK,ZLDA,NWG,VG,ZLD,WV,NFS1,NFS2)
DIMENSION IA(1),IB(1),X(1),Y(1),Z(1),NSA(1),NPLA(1),
*BDISK(1)
COMPLEX VGA(1),ZLDA(1),VG(1),ZLD(1)
C   DEFINE INNER AND OUTER EDGE POINTS FOR SPIRAL#1 WITH
C   45 DEGREE INCREMENTS.  THE FIRST 23 POINTS ARE INNER.
C   THE SECOND 23 POINTS ARE OUTER.
DO 150 I=1,23
  FF = REAL(I)
  PHEE = (FF-1.)*45.
  PHEEP = PHEE*3.14159265/180.
  BB = 0.00108*PHEE
  RR = (10.**BB)*0.395*0.01
  X(I) = RR*COS(PHEEP)
  Y(I) = RR*SIN(PHEEP)
  Z(I) = 0.
150 CONTINUE
DO 151 I=24,46
  FF = REAL(I)
  PHEE = (FF-24.)*45.
  PHEEP = PHEE*3.14159265/180.
  BB = 0.00106*PHEE
  RR = (10.**BB)*0.4437*0.01
  X(I) = RR*COS(PHEEP)
  Y(I) = RR*SIN(PHEEP)
  Z(I) = 0.
151 CONTINUE
C   SEGMENTATION FOR ARM#1.  THE FIRST 22 SEGMENTS FORM
C   THE INNER EDGE.  SEG. 23-44 FORM THE OUTER EDGE.  SEG.
C   45-67 FORM CROSS HATCHES.
DO 152 I=1,22
  IA(I) = I

```

```

    IB(I) = I+1
152 CONTINUE
    DO 153 I=23,44
    IA(I) = I+1
    IB(I) = I+2
153 CONTINUE
    DO 154 I=45,67
    IA(I) = I-44
    IB(I) = I-21
154 CONTINUE
C    DEFINE INNER AND OUTER EDGE POINTS FOR SPIRAL#2.
C    POINTS 47-69 ARE INNER.  POINTS 70-92 ARE OUTER.
    DO 155 I=47,69
    FF = REAL(I)
    PHEE = (FF-47.)*45.
    PHEEP = (PHEE+90.)*3.14159265/180.
    BB = 0.00108*PHEE
    RR = (10.**BB)*0.395*0.01
    X(I) = RR*COS(PHEEP)
    Y(I) = RR*SIN(PHEEP)
    Z(I) = 0.
155 CONTINUE
    DO 156 I=70,92
    FF = REAL(I)
    PHEE = (FF-70.)*45.
    PHEEP = (PHEE+90.)*3.14159265/180.
    BB = 0.00106*PHEE
    RR = (10.**BB)*0.4437*0.01
    X(I) = RR*COS(PHEEP)
    Y(I) = RR*SIN(PHEEP)
    Z(I) = 0.
156 CONTINUE
C    SEGMENTATION FOR ARM#2.  SEG.68-89 FORM THE INNER
C    EDGE.  SEG.90-111 FORM THE OUTER EDGE.  SEG.112-134
C    CROSS HATCHES.
    DO 157 I=68,89
    IA(I) = I-21
    IB(I) = I-20
157 CONTINUE
    DO 158 I=90,111
    IA(I) = I-20
    IB(I) = I-19
158 CONTINUE
    DO 159 I=112,134
    IA(I) = I-65
    IB(I) = I-42
159 CONTINUE
C    DEFINE INNER AND OUTER EDGE POINTS FOR SPIRAL#3.
C    POINTS 93-115 ARE INNER, 116-138 ARE OUTER.
    DO 160 I=93,115
    FF = REAL(I)
    PHEE = (FF-93.)*45.
    PHEEP = (PHEE+180.)*3.14159265/180.

```

```

BB = 0.00108*PHEE
RR = (10.**BB)*0.395*0.01
X(I) = RR*COS(PHEEP)
Y(I) = RR*SIN(PHEEP)
Z(I) = 0.
160 CONTINUE
DO 161 I=116,138
FF = REAL(I)
PHEE = (FF-116.)*45.
PHEEP = (PHEE+180.)*3.14159265/180.
BB = 0.00106*PHEE
RR = (10.**BB)*0.4437*0.01
X(I) = RR*COS(PHEEP)
Y(I) = RR*SIN(PHEEP)
Z(I) = 0.
161 CONTINUE
C SEMENTATION FOR ARM#3. SEG.135-156 FORM THE INNER
C EDGE. SEG.157-178 FORM THE OUTER EDGE. SEG.179-201
C ARE CROSS HATCHES.
DO 162 I=135,156
IA(I) = I-42
IB(I) = I-41
162 CONTINUE
DO 163 I=157,178
IA(I) = I-41
IB(I) = I-40
163 CONTINUE
DO 164 I=179,201
IA(I) = I-86
IB(I) = I-63
164 CONTINUE
C DEFINE INNER AND OUTER EDGE POINTS FOR SPIRAL#4.
C POINTS 139-161 ARE INNER, 162-184 ARE OUTER.
DO 165 I=139,161
FF = REAL(I)
PHEE = (FF-139.)*45.
PHEEP = (PHEE+270.)*3.14159265/180.
BB = 0.00108*PHEE
RR = (10.**BB)*0.395*0.01
X(I) = RR*COS(PHEEP)
Y(I) = RR*SIN(PHEEP)
Z(I) = 0.
165 CONTINUE
DO 166 I=162,184
FF = REAL(I)
PHEE = (FF-162.)*45.
PHEEP = (PHEE+270.)*3.14159265/180.
BB = 0.00106*PHEE
RR = (10.**BB)*0.4437*0.01
X(I) = RR*COS(PHEEP)
Y(I) = RR*SIN(PHEEP)
Z(I) = 0.
166 CONTINUE

```

```

C   SEGMENTATION OFR ARM#4.  SEG.202-223 FORM THE INNER
C   EDGE.  SEG.224-245 FORM THE OUTER EDGE.  SEG.246-268
C   ARE CROSS HATCHES.
    DO 167 I=202,223
      IA(I) = I-63
      IB(I) = I-62
167 CONTINUE
    DO 168 I=224,245
      IA(I) = I-62
      IB(I) = I-61
168 CONTINUE
    DO 169 I=246,268
      IA(I) = I-107
      IB(I) = I-84
169 CONTINUE
C   THE ARMS AND SEGMENTS ARE DEFINED.
C   THE REST IS FOR THE FEED STRUCTURE.
    X(185) = 0.
    Y(185) = 0.
    Z(185) = 0.
    X(186) = 0.0019
    Y(186) = 0.
    Z(186) = 0.
    X(187) = 0.
    Y(187) = 0.0019
    Z(187) = 0.
    X(188) = -0.0019
    Y(188) = 0.
    Z(188) = 0.
    X(189) = 0.
    Y(189) = -0.0019
    Z(189) = 0.
    IA(269) = 1
    IB(269) = 186
    IA(270) = 186
    IB(270) = 185
    IA(271) = 47
    IB(271) = 187
    IA(272) = 187
    IB(272) = 185
    IA(273) = 93
    IB(273) = 188
    IA(274) = 188
    IB(274) = 185
    IA(275) = 139
    IB(275) = 189
    IA(276) = 189
    IB(276) = 185
    NM = 276
    NP = 189
    NAT = 0
    NFS1 = 0
    NFS2 = 0

```

```
C THE FOLLOWING FOUR DELTA GAP GENERATORS ARE FOR SUM
C PATTERN FEEDING.
  VG(270) = (1.0,0.0)
  VG(272) = (0.0,1.0)
  VG(274) = (-1.0,0.0)
  VG(276) = (0.0,-1.0)
  RETURN
  ENL
```

When difference pattern feeding is desired, the last six lines of the subroutine can be substituted with the following.

```
  VG(270) = (1.0,0.0)
  VG(272) = (-1.0,0.0)
  VG(274) = (1.0,0.0)
  VG(276) = (-1.0,0.0)
  RETURN
  END
```

Appendix C

Plate Model Programming

In a program involving plates, the geometry input may be defined by allowing the main program of the ESP code to read the rectangular coordinates of each corner of each plate. However, when many plates are used in a model and equations can be used to generate these coordinates, it is simpler to use a subroutine to give the geometry. Such a subroutine can be used by a slight alteration of the main program of the ESP code. The following is a section of the main program before the alteration.

```
TOUCH = 0.001*WV
IOK = 1
READ(5,*)NPLTS
IF(NPLTS.EQ.0) GOTO 462
IOKT = 1
DO 464 NPL=1,NPLTS
  READ(5,*) NCNRS(NPL),SEGM(NPL),IREC(NPL),IPN(NPL),
  *IGS(NPL)
  DO 466 NCNP=1,NCNRS(NPL)
    READ(5,*)PCN(1,NCNP,NPL),PCN(2,NCNP,NPL),
    *PCN(3,NCNP,NPL)
466 CONTINUE
  CALL PLPLCK(PCN,IPL,ICN,NCNRS(NPL),TOUCH,NPL,IOK)
  IF(IOK.EQ.0)IOKT=0
464 CONTINUE
  IF(IOKT.EQ.0)GOTO9374
```

The READ statement in the third line is the seventh READ statement in the main program. The variable being read, NPLTS, is the total number of plates in the geometry. If the number of plates is zero, the program goes to line 462, which occurs just before the tenth READ statement.

The loop denoted by DO 464 is used to read the following variables [13:36].

NCNRS(NPL) = the number of corners in plate NPL

SEGM(NPL) = maximum segment size of a surface patch monopole
(1/2 of expansion function) in wavelengths,
typically 0.25

IREC(NPL) = plate indicator for plate NPL; it is zero when
plate is polygonal, one when plate is
rectangular

IPN(NPL) = polarization indicator, chosen to be three when
both polarizations of expansion functions are on
the plate

IGS(NPL) = number of generating side in a later subroutine
for mode expansion; it is chosen to be zero when
the longest side is used

The loop denoted by DO 466 is used to define the X, Y,
and Z coordinates for each corner of plate NPL. Then
SUBROUTINE PLPLCK is used to check the plate geometry to
make sure the corners of each plate are in the same plane
[13:106]. Finally, the variables IOK and IOKT are used as
flag variables which are used to abort the program when
SUBROUTINE PLPLCK sends the main program the abort message.
The GOTO 9374 sends the program to the end of execution.

To modify the program to accept a plate defining
subroutine, a new variable must be read by the main program
to indicate that a subroutine called WPLATE is being used.
This new variable is named NPIND. It may assume the
following values.

NPIND = 0 for plates defined conventionally with DO 464 and
DO 466 loops

NPIND = 1 for plates defined by SUBROUTINE WPLATE

NPIND must be set to zero when there are no plates. The
same passage of the ESP main program with the program

modifications is given below. New and changed statements are indicated with stars in the left hand column.

```
      TOUCH = 0.001*WV
*      IOKT = 1
      IOK = 1
*      READ(5,*) NPLTS, NPIND
      IF(NPLTS.EQ.0) GOTO 462
*      IF(NPIND.EQ.0) GOTO 2891
*      CALL WPLATE(NPLTS,NCNRS,SEGM,IREC,IPN,IGS,PCN)
*      DO 3245 NPL=1,NPLTS
*      CALL PLPLCK(PCN,IPL,ICN,NCNRS(NPL) TOUCH,NPL,IOK)
*      IF(IOK.EQ.0)IOKT=0
*3245 CONTINUE
*      GOTO 3333
      IOKT = 1
*2891 DO 464 NPL=1,NPLTS
      READ(5,*) NCNRS(NPL),SEGM(NPL),IREC(NPL),IPN(NPL),
*IGS(NPL)
      DO 466 NCNR=1,NCNRS(NPL)
      READ(5,*) PCN(1,NCNR,NPL),PCN(2,NCNR,NPL),
*PCN(3,NCNR,NPL)
      466 CONTINUE
      CALL PLPLCK(PCN,IPL,ICN,NCNRS(NPL),TOUCH,NPL,IOK)
      IF(IOK.EQ.0)IOKT=0
      464 CONTINUE
*3333 IF(IOKT.EQ.0) GOTO 9374
```

At this point, it is necessary to point out that the corner number NCNR should be placed on either consecutively clockwise or counterclockwise corners around a plate. If not, SUBROUTINE PLPLCK will reject the geometry. Also note that the only variable passed from the main program to SUBROUTINE WPLATE is the number of plates, NPLTS.

The following is a sample SUBROUTINE WPLATE that generates the plates for one arm of the antenna with 45 degree polar angle incrementation, as in wire grid modelling. The number of plates, NPLTS, is 22 to model the full arm.

```
SUBROUTINE WPLATE(NPLTS,NCNRS,SEGM,IREC,IPN,IGS,PCN)
  DIMENSION NCNRS(30),SEGM(30),IREC(30),IPN(30),IGS(30),
```

```

*PCN(3,4,30)
C
C THE DIMENSIONING ALLOWS FOR A MAXIMUM OF 30 PLATES AND
C FOUR CORNERS ON EACH PLATE.
C
DO 30 I=1,NPLTS
NCNRS(I) = 4
SEGM(I) = 0.25
IREC(I) = 0
IPN(I) = 3
IGS(I) = 0
30 CONTINUE
DO 40 I=1,NPLTS
FF = REAL(I)
PHEE = (FF-1.)*45.
PHEEP = PHEE*3.14159265/180.
PHEEO = PHEE+45.
PH = PHEEO*3.14159265/180.
BB = 0.00108*PHEE
RR = (10.**BB)*0.395*0.01
CC = 0.00108*PHEEO
SS = (10.**CC)*0.395*0.01
PCN(1,1,I) = RR*COS(PHEEP)
PCN(2,1,I) = RR*SIN(PHEEP)
PCN(3,1,I) = 0.
PCN(1,2,I) = SS*COS(PH)
PCN(2,2,I) = SS*SIN(PH)
PCN(3,2,I) = 0.
DD = 0.00106*PHEEO
TT = (10.**DD)*0.4437*0.01
EE = 0.00106*PHEE
UU = (10.**EE)*0.4437*0.01
PCN(1,3,I) = TT*COS(PH)
PCN(2,3,I) = TT*SIN(PH)
PCN(3,3,I) = 0.
PCN(1,4,I) = UU*COS(PHEEP)
PCN(2,4,I) = UU*SIN(PHEEP)
PCN(3,4,I) = 0.
40 CONTINUE
RETURN
END

```

This subroutine can be used to run the CPU execution time experiment mentioned in Chapter 3. Simply change the variable NPLTS read in the seventh READ statement of the main program.

If a geometry requires both wires and plates, both SUBROUTINE WPLATE and WGEOM may be used. The wire to plate

attachments would be put into SUBROUTINE WGEOM.

Bibliography

1. Stutzmann, Warren L. and Gary A. Thiele. Antenna Theory and Design. New York: John Wiley and Sons, 1981.
2. Johnson, Capt Thomas W. Lecture in EE 630, Applications of Electromagnetics. School of Engineering, Air Force Institute of Technology (AU), Wright-Patterson AFB OH, April 1984.
3. Green, R. B. The General Theory of Antenna Scattering. PhD dissertation. Ohio State University, Columbus OH, 1963.
4. Curtis, Walter. "Spiral Antennas," IRE Transactions on Antennas and Propagation: 298-306 (May 1960).
5. Cheo, B.R.S. and others. "A Solution to the Frequency-Independent Antenna Problem," IRE Transactions on Antennas and Propagation: 522-534 (November 1961).
6. Mei, K. K. "On the Integral Equations of Thin Wire Antennas," IEEE Transactions on Antennas and Propagation: 374-378 (May 1965).
7. King, R.W.P. The Theory of Linear Antennas. Cambridge MA: Harvard University Press, 1956.
8. Kent, William. Personal interview. Mission Avionics Analysis Branch, Aeronautical Systems Division, Wright-Patterson AFB OH, 24 April 1984.
9. Mosko, Joseph A. "An Introduction to Wideband, Two-Channel Direction-Finding Systems," Microwave Journal, 27: 91-105 (February 1984).
10. Papoulis, Athanasios. The Fourier Integral and its Applications. New York: McGraw Hill, 1962.
11. Rumsey, V. H. "Reaction Concept in Electromagnetic Theory," Physical Review, 94: 1483-1491 (June 1954).
12. Schelkunoff, S. A. Electromagnetic Waves. New York: D. Van Nostrand, 1943.
13. Newman, E. H. and P. Alexandropoulos. A User's Manual for Electromagnetic Surface Patch (ESP) Code: Version II - Polygonal Plates and Wires. Ohio State University, Columbus OH, 1983.
14. Schelkunoff, S. A. and H.T. Friis. Antennas: Theory and Practice. New York: John Wiley and Sons, 1952.

15. Beyer, William H. CRC Standard Mathematical Tables.
26th Edition, Boca Raton FL: CRC Press, 1982.
16. Baker, Dirk. Personal interview. 1984 Antenna
Applications Symposium, Robert Allerton Park IL, 21
September 1984.

Vita

Lieutenant John Paul Skinner was born on 11 March 1961 in Beaumont, Texas. He graduated from high school in Silsbee, Texas in 1979. He attended Texas A&M University, from which he graduated Summa Cum Laude with a Bachelor of Science degree in Electrical Engineering in December 1982. Upon graduation, he enlisted in the USAF and attended Officer Training School. He received his commission in the USAF in April 1983, and entered the School of Engineering, Air Force Institute of Technology, in May 1983.

Permanent address: P. O. Box 1397

Silsbee, Texas 77656

